ABSTRACT

Title of Dissertation: PATH-INTEGRAL MONTE-CARLO SIMULATIONS OF ALUMINUM ATOMS EMBEDDED IN SOLID *PARA*-HYDROGEN AND IN HELIUM CLUSTERS

Qian Wang, Doctor of Philosophy, 2005

Dissertation Directed By: Professor Millard H. Alexander
Department of Chemistry and Biochemistry &
The Institute for Physical Science and
Technology, University of Maryland

In this dissertation we use a path-integral Monte Carlo (PIMC) simulation method to study an open-shell atomic Al impurity doped in two kinds of low temperature condensed media.

We first use the Multilevel Metropolis PIMC method to study the arrangement of He atoms around a single Al atom doped in a He cluster. We use these results to simulate the Al electronic excitation spectrum in the cluster. Our accurate *ab initio* Al–He pair potentials and the Balling and Wright pairwise Hamiltonian model are used to describe the full potential and the electronic asymmetry arising from the open-shell character of the Al atom in its ground and excited electronic states.

To extend our investigation to more than one impurity atom, we develop a novel approach to the determination of the interaction between two atoms, each in a ^2P electronic state, embedded in a cluster of spherical atoms. The model transforms accurate *ab initio* potential energy curves for all the 36 molecular orbital states of the M–M system into a set of 36 Cartesian states that correspond to assigning the two 3*p*

electrons to Cartesian orbitals centered on each atom. In this Cartesian state basis, the matrix elements corresponding to the interaction of each ^2P atom with any number of surrounding spherical ligands can be determined. The lowest eigenvalue of the resulting 36×36 matrix defines, in an adiabatic approximation, the potential governing the motion of the atoms.

We use PIMC simulations to study the structural properties of pure solid *para*-hydrogen ($p\mathrm{H}_2$) and Al atoms embedded in solid $p\mathrm{H}_2$. For a single impurity Al atom, we predict the 3*p* electron density to be distributed mainly along one particular direction. This lowers the static lattice energy. For two Al atoms embedded in solid $p\mathrm{H}_2$ / $o\mathrm{D}_2$, we found that if the initial substitution sites are within a distance of ~ 13 Bohr, the Al atoms will significantly distort the lattice structure to allow recombination, with an accompanying release of energy during the process. For substitution distances longer than 14 bohr, the dispersion of Al atoms is shown to be metastable.

PATH-INTEGRAL MONTE-CARLO SIMULATIONS OF ALUMINUM ATOMS EMBEDDED IN SOLID *PARA*-HYDROGEN AND IN HELIUM CLUSTERS

By

Qian Wang

Dissertation submitted to the Faculty of the Graduate School of the
University of Maryland, College Park, in partial fulfillment
of the requirements for the degree of
Doctor of Philosophy
2005

Advisory Committee:
Professor Millard H. Alexander, Chair/Advisor
Professor Janice E. Reutt-Robey
Professor Devarajan Thirumalai
Assistant Professor Daniel Kosov
Professor Victor M. Yakovenko

Dedication

To my husband, Wei: 600 miles a week, all these years, together we built the road. Thank you.

To my parents, Guanghua and Zhixiu, who always supported me, who were (and still are) always there for me.

Acknowledgements

I first wish to express my deepest gratitude to Millard Alexander, my advisor, who introduced me to this field more than three years ago. Without the guidance, stimulating discussions, support, encouragement, and learning opportunities he enabled, none of the work in this thesis would be possible. He has made my graduate experience at the University of Maryland at College Park an excellent one.

I have been benefited significantly from previous advances and applications of the path-integral, Monte-Carlo (PIMC) method. In particular, I am grateful to Professor Mark Tuckerman for providing his lecture notes on Path-Integral Molecular Dynamics, which first introduced to me the staging method. I am grateful to Professor David Ceperley who gave me his PIMC code. This provided invaluable guidance in the development of my own multilevel PIMC code. I also thank Xiaofeng Tan for his help with the correct assignment of the electronic states of the Al_2 dimer.

I am grateful for the support of the other members of the Alexander research group. In particular, I would like to thank my officemates and close friends Sule Atahan and Yi-Ren Tzeng. Troubleshooting my computer codes, and spending nights in the office working together, they contributed to both my science and my English. Their friendship added much enjoyment to my graduate work.

I am grateful for the support of the Chemical Physics program at the University of Maryland, especially to Professor Michael Coplan and Diane Mancuso, who helped me a lot through the years.

And last but not least: thanks to all my family and friends, for their constant support.

Table of Contents

List of Tables

List of Figures

Chapter 1: Introduction to the use of path-integral Monte-Carlo methods to investigate open-shell systems

1.1 Introduction

In the language of quantum chemistry, an open shell is a valence shell that is not completely filled with electrons. The resulting unpaired spin and/or orbital angular momenta introduce major difficulties in the variational solution of the Schrödinger equation for open-shell systems. Obtaining accurate orbital and energies for an open-shell system is far more complicated than for a closed-shell system.[1] However, much important chemistry involves open-shell encounters.

An even more complicated problem for theory is extended systems involving open-shell impurities. Experimentally, open-shell atoms have been doped in solid *para*-hydrogen and helium droplets, either to study how the embedded atoms effect the energetics and properties of the system or to understand how the electronic states of the impurity atom are altered by the solvation.[2-11] For the doped hydrogen systems, the interest also comes from the potential technological application of energy storage (as will be discussed in more detail in the Introductions to Chapters 3 and 4). Helium droplets have been recently exploited as a weakly perturbing, homogeneous and ultracold matrix for high-resolution spectroscopy (see more in Chapter 2).

Previous theoretical investigations of atomic impurities in condensed media have largely considered impurities that are closed-shell or have spherical charge distributions. Here, the assumption of a pairwise-additive potential is widely made. The interactions between particles are taken to be functions of nuclear positions only with no dependence on the angular orientation of the electrons. This assumption is not

a plausible one for open-shell atoms, whenever the electronic charge distribution is non-spherical. Because of the rotational invariance of the Hamiltonian, an isolated open-shell atom has three-fold (*P* states) or five-fold (*D* states) spatial degeneracy. However, the symmetry is broken by the presence of near-by ligands, so that this degeneracy is lifted. For an atom in a *P* state, for example, the p_x, p_y, and p_z orbitals can interact differently with the neighboring ligands.

Alexander *et al*. were among the first who took into account electronic anisotropy in modeling open-shell atoms in clusters.[12,13] They used the Balling and Wright model[14] in a study of the importance of the orbital degeneracy of the B atom in solid $p\mathrm{H}_2$ (with Krumrine, Jang and Voth).[15] Mirijanian, Alexander and Voth further extended the quantum simulation studies of Alexander and co-workers[15] to an atomic Al impurity.[16] In both simulations, neglect of the electronic anisotropy can lead to major inaccuracies in the calculated binding energy and in the radial distribution function of the impurity, especially when vacancies are present in the solid host.[15,16]

In section 1.2 of this chapter, we review briefly the Balling and Wright model for a single ^2P atomic impurity in clusters of spherical particles. As an extension of this earlier work, in Chapter 2 we discuss our use of the path-integral, Monte-Carlo method to simulate the electronic absorption of a single Al atom in helium clusters. The path-integral method is the best choice to investigate properties of quantum systems at low temperature, but not absolute zero. In section 1.3 of this chapter, we review the basic equations relevant to the Monte-Carlo implementation of the path-integral method. In Chapter 2, we will turn our attention to the more sophisticated algorithm needed to describe liquid helium and impurity-doped liquid helium at very low temperatures.

For open-shell atoms like B and Al, one important question remains unanswered: When doped with multiple atomic impurities, is the system, albeit at

ultra-low temperature, stable with respect to recombination, which is a highly exothermic process? To study more than one doped atom, we must consider the interaction between open-shell impurity atoms, which depends on the relative orientation of the *p*-electrons of both dopants.

In Chapter 3, we develop an accurate description of the interaction of two ^2P atoms in the presence of multiple spherical ligands. We will apply this to the interaction of two Al atoms embedded in solid $p\mathrm{H}_2$, site-substituted in the center of two adjacent hexagons. In Chapter 4, we will further perform a series of PIMC simulations of solid $p\mathrm{H}_2$ (or $o\mathrm{D}_2$) with two Al atoms initially site-substituted in different locations. The aim is the understanding of the equilibrium stability of the trapped Al impurities and the changes in the solid structure when multiple Al dopants are added.

Chapter 5 contains the conclusions of this dissertation.

1.2 Interaction of a single ^2P Atom with multiple spherical ligands

To describe the interaction of one ^2P atom embedded in a cluster formed of spherical ligands, we use a model, first presented by Balling and Wright[14] for the interaction of alkali metal atoms with spherical ligands. This model is based on explicit consideration of the interaction of the p_x, p_y, and p_z orbitals of the metal with each ligand. The ^2P atom will be described in an uncoupled, Cartesian basis $| lq_l >$ where l, the orbital electronic angular momentum of the atom is 1 and q_l {= *x, y,* or *z*} designates the orientation of the real (Cartesian) singly-filled *p* orbital. The encounter between an atom in a ^2P state and a spherical atom at any position in space can be described as a rotation of a diagonal matrix that contains the two potentials, V_Σ and V_Π, which describe the interaction of the ^2P atom and the spherical partner when the latter is located on the *z* axis.[14,17]

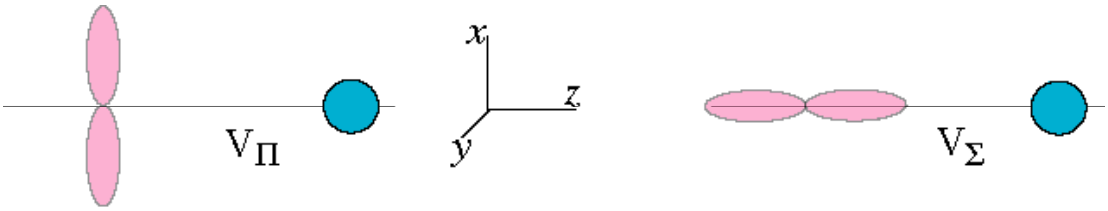

Fig 1.1 The interaction of a ^2P atom and a spherical ligand located on the z axis.

If the spherical atom is rotated to a position $\{R, \theta, \phi\}$, the interaction is described by the matrix, still in the basis of the three Cartesian p orbitals,

$$\mathbf{V}(R, \theta, \phi) \equiv \mathbf{D}(\phi, \theta, 0)\, \mathbf{V}(R)\, \mathbf{D}^T(\phi, \theta, 0) \tag{1.1}$$

Here, $\mathbf{D}(\phi, \theta, 0)$ is the matrix of the rotation specified by the Euler angles $\{\phi, \theta, 0\}$, and $\mathbf{V}(R)$ is a diagonal matrix with elements

q_l	$q_l = x$	y	z
x	$V_\Pi(R)$	0	0
y	0	$V_\Pi(R)$	0
z	0	0	$V_\Sigma(R)$

(1.2)

It can be shown that the transformation of Eq. (1.1) leads to the following expression for $\mathbf{V}(R,\theta,\phi)$, still in the basis of the x, y and z Cartesian p orbitals.

$$\mathbf{V} = V_\Pi\, \mathbf{1} + (V_\Sigma - V_\Pi) \times \frac{1}{R^2} \begin{vmatrix} x^2 & xy & xz \\ xy & y^2 & yz \\ xz & yz & z^2 \end{vmatrix} \tag{1.3}$$

where $\mathbf{1}$ designates the unit matrix and $\{x,y,z\}$ designates the Cartesian position of the spherical ligand. Here we have suppressed the arguments of $\mathbf{V}$ and the dependence on R of V_Σ and V_Π. In the basis of the Cartesian orbitals with negative spin projection,

which we designate by an overbar on each quantum number ($\bar{x},\bar{y},\bar{z}$), we have an identical 3×3 matrix, so that in the basis of the six *p* spin orbitals, the interaction of the Al atom with a spherical perturber at position {*x,y,z*} is block diagonal and given by

$$\mathbf{V}_6(x,y,z)=\begin{vmatrix}\mathbf{V} & 0\\ 0 & \mathbf{V}\end{vmatrix} \tag{1.4}$$

where **V** is the 3×3 matrix defined by Eq. (1.3).

In the presence of multiple spherical ligands, each located at position $\{x_i,y_i,z_i\}$, the matrix of the complete interaction Hamiltonian is just

$$\mathbf{V}=\sum_i \mathbf{V}_6(x_i,y_i,z_i) \tag{1.5}$$

In the 6×6 basis of the three Cartesian *p* orbitals (and their two spin projections), the matrix of the spin-orbit Hamiltonian is

$$\underline{\underline{H}}_{so}=\frac{1}{2}a\times\begin{array}{c|cccccc} & x & y & z & \bar{x} & \bar{y} & \bar{z}\\ \hline x & 0 & i & 0 & 0 & 0 & 1\\ y & -i & 0 & 0 & 0 & 0 & i\\ z & 0 & 0 & 0 & -1 & -i & 0\\ \bar{x} & 0 & 0 & -1 & 0 & -i & 0\\ \bar{y} & 0 & 0 & i & i & 0 & 0\\ \bar{z} & 1 & -i & 0 & 0 & 0 & 0 \end{array} \tag{1.6}$$

where *a* is the spin-orbit constant of the ^2P atom (74.7 cm^{-1} for Al[18]).

In the adiabatic limit, we diagonalize the sum of the 6×6 **V** matrix and the 6×6 matrix of the spin-orbit operator for the single ^2P atom [Eq. (1.6)]. The motion of the atoms is governed by the lowest root V_a, to which is added the pair-wise scalar interaction between all the spherical ligands.

1.3 Path-integral Monte-Carlo simulations

1.3.1 The Path-integral method

Path-integral (PI) simulation is a powerful computational tool to calculate properties of quantum many-particle systems. It can be applied to systems at finite temperature, unlike other quantum simulation methods which are essentially zero-temperature methods.[19] For a comprehensive review, see Berne and Thirumalai.[20]

The PI method is based on the discretization of the path-integral representation of the density matrix developed by Feynman and Hibbs.[21] If the exact eigenvalues and eigenfunctions for a Hamiltonian H are designated E_i and ϕ_i, then the single-particle quantum partition function is, at constant volume and temperature (a canonical ensemble; we will extend the method to isothermal-isobaric ensembles in Chapter 4):

$$Q_{1VT} = \sum_i e^{-\beta E_i} = Tr(e^{-\beta \mathrm{H}}) \tag{1.7}$$

with $\beta=1/k_BT$. The trace can be carried out in any complete basis. Specifically, if we work in a coordinate basis, the trace becomes

$$Q_{1VT} = \int d\mathbf{q} \langle \mathbf{q} \mid e^{-\beta \mathrm{H}} \mid \mathbf{q} \rangle \tag{1.8}$$

where $\mathbf{q}$ designates the coordinates of the particle. The quantity $\langle \mathbf{q} \mid e^{-\beta \mathrm{H}} \mid \mathbf{q} \rangle$ is the diagonal element of the density operator in position space.

We then divide the exponential into p parts (p is called the Trotter number) to facilitate evaluation of the matrix element. We insert $p-1$ unit operators in the form

$$\mathbf{1} = \int d\mathbf{q} \mid \mathbf{q} \rangle \langle \mathbf{q} \mid \tag{1.9}$$

and split the exponential as follows:

$$
\begin{aligned}
Q_{1VT} &= \int d\mathbf{q} \left\langle \mathbf{q} \left| e^{-\beta \mathrm{H}/p} \ldots e^{-\beta \mathrm{H}/p} \ldots e^{-\beta \mathrm{H}/p} \right| \mathbf{q} \right\rangle \\
&= \int d\mathbf{q}_1 d\mathbf{q}_2 \ldots d\mathbf{q}_p \left\langle \mathbf{q}_1 \left| e^{-\beta \mathrm{H}/p} \right| \mathbf{q}_2 \right\rangle \ldots \left\langle \mathbf{q}_{p-1} \left| e^{-\beta \mathrm{H}/p} \right| \mathbf{q}_p \right\rangle \left\langle \mathbf{q}_p \left| e^{-\beta \mathrm{H}/p} \right| \mathbf{q}_1 \right\rangle
\end{aligned} \tag{1.10}
$$

Instead of one integral over the diagonal elements of the density operator at low temperature T, we now have p integrals involving off-diagonal terms of the density operator at a higher effective temperature pT. Instead of integrating over the spatial coordinates of the original particle, we integrate over the spatial coordinates of p pseudoparticles. If (as in the systems treated in this dissertation) the Hamiltonian depends only on the momenta and coordinates, it can be split into two pieces, H=T+V, where $\mathrm{T} = \mathrm{P}^2/2m$ is the kinetic energy operator and V is the potential energy operator.

When p is large enough, there exist several accurate high-temperature approximations to the density matrix.[19] We use the simplest, the so called "*primitive*" approximation, which is based on the Trotter formula,[22]

$$
e^{-\beta \mathrm{H}/p} \approx e^{-\beta \mathrm{T}/p} e^{-\beta \mathrm{V}/p} \approx e^{-\beta \mathrm{V}/p} e^{-\beta \mathrm{T}/p} \approx e^{-\beta \mathrm{V}/2p} e^{-\beta \mathrm{T}/p} e^{-\beta \mathrm{V}/2p} \tag{1.11}
$$

with error of order $O[(\beta/p)^2]$. Then T and V are (approximately) decoupled and the density matrix can be calculated explicitly, as follows:

$$
\langle \mathbf{q}_i \mid e^{-\beta \mathrm{H}/p} \mid \mathbf{q}_{i+1} \rangle = \exp\left(-\frac{\beta [V(\mathbf{q}_i) + V(\mathbf{q}_{i+1})]}{2p} \right) \langle \mathbf{q}_i \mid e^{-\beta \mathrm{T}/p} \mid \mathbf{q}_{i+1} \rangle \tag{1.12}
$$

The free particle kinetic energy can be shown to be,[21]

$$
\langle \mathbf{q}_i \mid e^{-\beta \mathrm{T}/p} \mid \mathbf{q}_{i+1} \rangle = \left(\frac{mp}{2\pi\beta\hbar^2} \right)^{1/2} \exp\left(-\frac{mp}{2\beta\hbar^2} \mid \mathbf{q}_i - \mathbf{q}_{i+1} \mid^2 \right) \tag{1.13}
$$

Here m is the mass of the particle and $\mid \mathbf{q}_i - \mathbf{q}_{i+1} \mid$ is the distance between pseudoparticles i and i+1. Thus

$$Q_{1VT} \approx (\frac{mp}{2\pi\beta\hbar^2})^{3p/2} \int d\mathbf{q}_1 d\mathbf{q}_2 ... d\mathbf{q}_p \exp\left\{-\sum_{i=1}^{p}\left[\frac{mp}{2\beta\hbar^2} \mid \mathbf{q}_i - \mathbf{q}_{i+1} \mid^2 + \frac{\beta}{p} V(\mathbf{q}_i)\right]\right\} \quad (1.14)$$

with $\mathbf{q}_{p+1}=\mathbf{q}_1$.

It is straightforward to generalize the above formula to a system of N indistinguishable quantum particles of identical mass. We have

$$Q_{NVT} \approx \frac{1}{N!}(\frac{mp}{2\pi\beta\hbar^2})^{3pN/2} \int d\mathbf{q}_1 d\mathbf{q}_2 ... d\mathbf{q}_p \exp\left\{-\sum_{i=1}^{p}\left[\frac{mp}{2\beta\hbar^2} \mid \mathbf{q}_i - \mathbf{q}_{i+1} \mid^2 + \frac{\beta}{p} V(\mathbf{q}_i)\right]\right\} \quad (1.15)$$

Here each vector $\mathbf{q}_i$ represents the set of $3N$ coordinates describing the i^{th} pseudosystem of N particles, which is often designated a "slice",[19] and the quantity $\mid \mathbf{q}_i - \mathbf{q}_{i+1} \mid^2$ is the square of the distance between two slices in the $3N$ coordinate space. The partition function then appears as a Boltzmann average over all positions of the slices of an effective potential V_{eff}, which consists of the potential plus a harmonic potential of force constant $mp / \beta^2\hbar^2$ between each slice.

Note that the particles are assumed to obey ordinary Boltzmann statistics. Whenever the symmetry properties of these quantum particles need to be taken into account, the above canonical partition function must be modified to include Bose or Fermi statistics under permutation. Specifically, the states involved in the summation would be either totally symmetric or totally antisymmetric with respect to the interchange of any two particles.[21] However, studies have shown that identical particle exchange is significant only for cryogenic liquid helium (both ^{3}He and ^{4}He).[23]

Extending of Eq. (1.15) to a mixed system is straightforward. Suppose we have n_{H_2} hydrogen molecules and n_{Al} Al atoms, the partition function is given by

$$Q_{NVT} \approx \frac{1}{n_{H_2}!n_{Al}!}\left(\frac{m_{H_2}p}{2\pi\beta\hbar^2}\right)^{3pn_{H_2}/2}\left(\frac{m_{Al}p}{2\pi\beta\hbar^2}\right)^{3pn_{Al}/2}$$
$$\times\int d\mathbf{q}_1 d\mathbf{q}_2 ... d\mathbf{q}_p \exp\left\{-\sum_{i=1}^{p}\left[\frac{m_{H_2}p}{2\beta\hbar^2}\mid \mathbf{q}_{i,H_2}-\mathbf{q}_{i+1,H_2}\mid^2+\frac{m_{Al}p}{2\beta\hbar^2}\mid \mathbf{q}_{i,Al}-\mathbf{q}_{i+1,Al}\mid^2+\frac{\beta}{p}V(\mathbf{q}_i)\right]\right\} \tag{1.16}$$

Here, $\mathbf{q}_{i,H_2}$, $\mathbf{q}_{i,\mathrm{Al}}$ are the $3\,n_{\mathrm{H_2}}$ coordinates of the hydrogen molecules and the $3n_{\mathrm{Al}}$ coordinates of the Al atoms in the i^{th} slice. Here, also, the effective potential is

$$\beta V_{eff} = \sum_{i=1}^{p}\left[\frac{m_{H_2}p}{2\beta\hbar^2}\mid \mathbf{q}_{i,H_2}-\mathbf{q}_{i+1,H_2}\mid^2+\frac{m_{al}p}{2\beta\hbar^2}\mid \mathbf{q}_{i,Al}-\mathbf{q}_{i+1,Al}\mid^2+\frac{\beta}{p}V(\mathbf{q}_i)\right] \tag{1.17}$$

The average of an observable A for the system can be calculated as

$$\langle A\rangle = \frac{\frac{1}{p}\int d\mathbf{q}_1 d\mathbf{q}_2 ... d\mathbf{q}_p \sum_{i=1}^{p} A(\mathbf{q}_i)e^{-\beta V_{eff}}}{\int d\mathbf{r}_1 d\mathbf{r}_2 ... d\mathbf{r}_p e^{-\beta V_{eff}}} \tag{1.18}$$

1.3.2 Monte-Carlo implementation

Obviously, one cannot carry out the quadrature exactly, which would require summing over all possible coordinates of the *N*-particle slices. Consequently, a more approximate computational algorithm has been developed to permit use of this PI technique to compute detailed microscopic properties. This is the Monte-Carlo (MC) approach, which is based on ideas developed by von Neumann, Ulam, and Metropolis in the 1940's to study the diffusion of neutrons in fissionable material.[24] The name "Monte-Carlo" refers to the role that random numbers play in the method.

A straightforward implementation of the MC approach to our system would be to choose equally from all possible states, and then weight them by their Boltzmann factor $\exp(-\beta V_{eff})$. Unfortunately, in this process time is wasted in sampling statistically unimportant configurations with small values of $\exp(-\beta V_{eff})$. It is important to use sampling techniques that choose random numbers from a distribution adjusted so that the function evaluation is concentrated in regions of

space that make important contributions to the integral.[24] The choice of points is generated by application of the so-called standard Metropolis algorithm.[25] It chooses states with probability $\exp(-\beta V_{eff})$, and weights them equally. The detailed algorithm is:

1. Choose a set of p slices as the initial configuration. Calculate V_{eff} for this configuration.
2. Displace the pseudoparticles in one slice in position space by a random vector $d\mathbf{q}=\Delta\mathbf{r}$, where Δ is the maximum displacement allowed in each dimension and $\mathbf{r}$ is a pseudorandom matrix of size $3\times N$ over the range $[-1,1]$. Calculate $V_{eff,new}$ for this altered configuration; then calculate the change in the effective potential relative to the previous configuration, $\delta V = V_{eff,new} - V_{eff}$;
3. If $\delta V \leq 0$, the new configuration is accepted. Otherwise, a random number $0 \leq \eta \leq 1$ is generated, and the new configuration is accepted only if $\exp(-\beta\delta V) > \eta$;
4. Go back to step (2) and iterate.

After a number of iterations, hopefully not too large, the set of slices will converge to those that make the most substantial contributions to the ensemble averages.

This algorithm, while in principle capable of any accuracy, converges only slowly when dealing with quantum system at very low temperatures. In the next chapter we will detail one important improvement over the standard Metropolis algorithm, which makes possible the simulation of helium systems.

The Metropolis algorithm generates simulation trajectories that are naturally weighted to favor thermally populated states of the system. The other widely used simulation method for chemical systems is Molecular Dynamics (MD). In the MD method one generates trajectories by iteratively solving the equation of motion of the system. The trajectories are in real time. By contrast a PIMC simulation explores

phase space without evolving in real time. For the determination of equilibrium statistical averages, the two methods should give essentially same results, provided that ergodicity is ensured (in other words, provided that the time average is equivalent to the ensemble average).

In Ceperley's review of the application of path-integral methodology to condensed helium,[19] he compared the PIMC and PIMD methods. He pointed out "dynamical methods by themselves can not treat problems in which quantum statistics are important," because it is not possible for the permutation to change continuously. Even for systems of distinguishable particles, "there are two major concerns with MD methods: ergodicity and efficiency." Ergodicity in MD can be ensured by using a Nosé thermostat or with a hybrid MC-MD method. For efficiency in MD, Tuckerman *et al*.[26] have introduced methods to accelerate convergence.

Metropolis MC usually entails single-particle moves, while in MD simulations one moves all particles simultaneously. In cases where a computer intensive potential calculation must be done for all the particles simultaneously (as, for example, when a Car-Parrinello local-density-functional algorithm is used), the MD technique is advantageous because it moves more particles before a recalculation of the potential is necessary. In these cases, PIMD simulations can be almost as efficient as PIMC.

As it will be shown in following chapters, our potential model couples all the particles in the system together, so the interaction potential must be determined for all the pseudoparticles simultaneously. We move all pseudoparticles in one slice simultaneously in the MC process.

Another important factor in comparing MD with MC is the cost of calculating forces *vs*. that of calculating potentials. In MC, one only needs interactions, while in MD, one needs the forces, namely, derivatives of the interactions. In pair-wise additive potential models, the force calculation does not cost much more. In our potential model, however, derivative calculations are expensive. Another advantage

of MC over MD in our work is the simplicity in coding. Finally, MC simulations correspond naturally to a canonical ensemble, while straight MD simulations correspond to a constant energy ensemble. To carry out constant temperature MD simulations requires the additional complexity of adding Nosé-Hover chains.[27-30]

1.3.3 The pair correlation function $g(r)$

By definition, $\rho g(r)$ is the conditional probability density that a particle will be found at r given that another is at the origin, where $\rho=N/V$ is the average number density for N particles in volume V.[31] The number of neighbors within a distance r_o of a central atom is

$$n(r_o) = 4\pi\rho\int_0^{r_o} r^2 g(r)dr \quad . \tag{1.19}$$

Consequently, the pair-correlation function (often called the radial distribution function) $g(r)$, is the probability of finding a pair of particles a distance r apart, relative to the probability expected for a completely random distribution at the same density. Thus, $g(r)$ approaches a limiting value of unity at large values of r.

In a canonical ensemble of N particles the pair-correlation function is given by

$$g(r) = g(\mathbf{r}_1,\mathbf{r}_2) = \frac{N(N-1)\int d\mathbf{r}_3 d\mathbf{r}_4 ... d\mathbf{r}_N \exp\left[-\beta U(\mathbf{r}_1,\mathbf{r}_2,...\mathbf{r}_N)\right]}{\rho^2 \int d\mathbf{r}_1 d\mathbf{r}_2 ... d\mathbf{r}_N \exp\left[-\beta U(\mathbf{r}_1,\mathbf{r}_2,...\mathbf{r}_N)\right]} \tag{1.20}$$

where $\mathbf{r}_i$ is the coordinate of the i^{th} particle. Here U is the classical potential energy.[31] Equivalently,[24]

$$g(r) = \rho^{-2}\left\langle \sum_i \sum_{j\neq i} \delta(\mathbf{r}_i)\delta(\mathbf{r}_j - \mathbf{r}) \right\rangle = \frac{V}{N^2}\left\langle \sum_i \sum_{j\neq i} \delta(\mathbf{r} - \mathbf{r}_{ij}) \right\rangle. \tag{1.21}$$

The second expression in this equation is the one we use to evaluate $g(r)$ from a computer simulation. We shall define $N(r)$ to be the average number of particles situated at a distance r and $r+dr$ from a given particle. By measuring the distance between each pair of particles as the simulation evolves and sorting the values into bins, we can obtain a histogram of the function $N(r)$. The pair correlation function is

then

$$g(r+\tfrac{1}{2}\delta r)=\frac{N(r)}{4\pi\rho\left[(r+\delta r)^3-r^3\right]/3} \tag{1.22}$$

where $4\pi\left[(r+\delta r)^3-r^3\right]/3$ is the volume of each bin.

In our path-integral method, the pair correlation function is similarly defined, with $\boldsymbol{r}$ being the coordinate of a pseudoparticle. If different species (Al, $p\mathrm{H_2}/o\mathrm{D_2}$, He) are present, pair correlation functions $g_{ab}(r_{ab})$ can be defined for each pair,[24] using the same definition as in the single species case. Consequently, the binary Al-$\mathrm{H_2}$ system is described by 3 independent g_{ab} functions: $g_{\mathrm{H_2-H_2/O_2-O_2}}$, $g_{\text{Al-Al}}$ and $g_{\mathrm{Al-H_2/O_2}}$, which provide information about the location of the various pairs of atoms in the solid.

1.3.4 Kinetic energy, potential energy and pressure estimators

For N indistinguishable particles, an estimator for the kinetic energy is obtained by applying the thermodynamic relationship $E=\partial(\beta A)/\partial\beta=-\partial(\ln Q)/\partial\beta$ to the partition function of Eq. (1.15) and then subtracting the expectation value of the potential energy. Here, E is the total internal energy and A is the Helmholtz free energy. The resulting expression for the average kinetic energy is

$$\langle E_k\rangle=\frac{p}{2\beta}\left(3N-\frac{m}{\beta\hbar^2}\left\langle\sum_{i=1}^{p}|\,\mathbf{q}_i-\mathbf{q}_{i+1}\,|^2\right\rangle\right)\quad. \tag{1.23}$$

This estimator predicts that the translational kinetic energy is given by the difference between a constant (p times the average thermal energy of the system $-\ \frac{3}{2}NkT$) and the energy stored in the springs between the slices.[32-34]

For our system with $n_{\mathrm{H_2}}$ hydrogen molecules and n_{Al} Al atoms, we obtain a similar expression for the total energy

$$\langle E\rangle = \frac{p}{2\beta}\left(3n_{H_2} - \frac{m}{\beta\hbar^2}\left\langle \sum_{i=1}^{p} | \mathbf{q}_{i,H_2} - \mathbf{q}_{i+1,H_2} |^2 \right\rangle\right) + \frac{p}{2\beta}\left(3n_{Al} - \frac{m}{\beta\hbar^2}\left\langle \sum_{i=1}^{p} | \mathbf{q}_{i,Al} - \mathbf{q}_{i+1,Al} |^2 \right\rangle\right) + \frac{1}{p}\left\langle \sum_{i=1}^{p} V(\mathbf{q}_i) \right\rangle \tag{1.24}$$

Here the first term is the contribution of the kinetic energy of the hydrogen molecules; the second term, the kinetic energy of the Al atoms; and the last term, the average total potential energy. We shall refer to the latter as the static lattice energy.

Herman, Bruskin and Berne[35] showed that the variance of this "crude" kinetic energy estimator is large, and the relative error in the determination of the energy increases with the number of discrete points, p. On the one hand the Trotter approximation becomes more accurate with large p. However, large p requires more computational resources and produces a larger relative error in the average kinetic energy. For balance, one needs to choose a moderately large value of p.

This estimate of the kinetic energy is very imprecise for a single quantum particle. However, for systems with a large number of particles and for relatively small value of p, the large variance of the kinetic energy estimator for one particle is compensated by the large number of independent estimates from the different particles, so it is still a reasonable estimator.[34] The advantage for us is that this estimator does not require derivatives of the potential energy. When the potential energy is pairwise additive, determination of these derivatives is not difficult. However, in the anisotropic potential models we use here, the calculation of derivatives requires considerably more effort. So in this dissertation, unless otherwise stated, we use the estimator of Eq. (1.24) for the kinetic energy.

Other kinetic energy estimators have been introduced in the literature, one of which we will indirectly use in our constant pressure simulations. The first is the virial energy estimator proposed by Herman, Bruskin and Berne.[35] For a single particle in 1-dimension, the kinetic energy is estimated as

$$\langle E_k \rangle = \frac{1}{2p} \left\langle \sum_{i=1}^{p} x_i \frac{\partial V(x_i)}{\partial x_i} \right\rangle \tag{1.25}$$

The authors have shown this estimator is better behaved than the crude estimator of Eq. (1.23). It also avoids the drawback present in the crude estimator that the result is given as a difference between two large quantities.

Another kinetic energy estimator for a single particle in 1-dimension,[36] obtained from integration by parts, has the form

$$\langle E_k \rangle = \frac{3}{2\beta} + \frac{1}{2p} \left\langle \sum_{i=1}^{p} (x_i - x_p) \frac{\partial V(x_i)}{\partial x_i} \right\rangle \tag{1.26}$$

Here the first term corresponds to the kinetic energy of the free particle, the second term reflects modifications in the kinetic energy due to the effect of the interparticle interactions.

It is straightforward to extend Eqs. (1.25) and (1.26) to our case of multiple species and multiple dimensions. The resulting equations are not given here.

Another related problem is the determination of the pressure.[24,34,37,38] To proceed, we first observe that the coordinate derivative in the virial theorem, $\left\langle x_j \frac{\partial H}{\partial x_j} \right\rangle = k_B T$,[39] is the negative of a component of the total force $\vec{f}_j$ on particle j.

$$-\frac{1}{3} \left\langle \sum_{i=1}^{p} \sum_{j=1}^{N} q_{i,j} \frac{\partial \mathrm{H}}{\partial q_{i,j}} \right\rangle = \frac{1}{3} \left\langle \sum_{i=1}^{p} \sum_{j=1}^{N} q_{i,j} \overrightarrow{f_{i,j}^{\mathrm{tot}}} \right\rangle = -pNk_B T \tag{1.27}$$

The factor of 3 here accounts for the 3-dimensional nature of the system. The total force is the sum of internal forces between particles plus any external forces. The latter are related to the external pressure, namely[24]

$$\frac{1}{3} \left\langle \sum_{i=1}^{p} \sum_{j=1}^{N} q_{i,j} \overrightarrow{f_{i,j}^{\mathrm{ext}}} \right\rangle = -PV \quad . \tag{1.28}$$

For internal forces, we define

$$\alpha = \frac{mp}{2\beta^2 \hbar^2} \sum_{i=1}^{p} \sum_{j=1}^{N} \left(q_{i,j} - q_{i+1,j} \right)^2 \ , \tag{1.29}$$

so that the effective interaction potential from the Trotter approximation is

$$V_{eff} = \alpha + \frac{1}{p}\sum_{i=1}^{p} V(\mathbf{q}_i) + \text{constant} \ . \tag{1.30}$$

Euler's homogeneous function theorem states that for a homogeneous function of degree n [that is, a function such that $f(tx, ty) = t^n f(x, y)$]

.

$$x\frac{\partial f(x,y)}{\partial x} + y\frac{\partial f(x,y)}{\partial y} = nf(x,y) \ , \tag{1.31}$$

We can use this result to derive the following equation:

$$\begin{aligned} -\frac{1}{3}\left\langle \sum_{i=1}^{p}\sum_{j=1}^{N} q_{i,j}\frac{\partial V_{eff}}{\partial q_{i,j}} \right\rangle &= \frac{1}{3}\left\langle \sum_{i=1}^{p}\sum_{j=1}^{N} q_{i,j}\overrightarrow{f_{i,j}^{\text{int}}} \right\rangle \\ &= -\frac{1}{3}\left\langle \sum_{i=1}^{p}\sum_{j=1}^{N} q_{i,j}\frac{\partial \alpha}{\partial q_{i,j}} \right\rangle - \frac{1}{3p}\left\langle \sum_{i=1}^{p}\sum_{j=1}^{N} q_{i,j}\frac{\partial V(\mathbf{q}_i)}{\partial q_{i,j}} \right\rangle \\ &= -\frac{2}{3}\langle \alpha \rangle - \frac{1}{3p}\left\langle \sum_{i=1}^{p}\sum_{j=1}^{N} q_{i,j}\frac{\partial V(\mathbf{q}_i)}{\partial q_{i,j}} \right\rangle \end{aligned} \tag{1.32}$$

so that

$$\begin{aligned} PV &= pNk_BT - \frac{2}{3}\langle \alpha \rangle - \frac{1}{3p}\left\langle \sum_{i=1}^{p}\sum_{j=1}^{N} q_{i,j}\frac{\partial V(\mathbf{q}_i)}{\partial q_{i,j}} \right\rangle \\ &= pNk_BT - \sum_{i=1}^{p}\sum_{j=}^{N}\left\langle \frac{mp}{3\beta^2\hbar^2}\left(q_{i,j} - q_{i+1,j}\right)^2 + \frac{1}{3p}q_{i,j}\frac{\partial V(\mathbf{q}_i)}{\partial q_{i,j}} \right\rangle \end{aligned} \tag{1.33}$$

We note that this expression for PV is equal to 2/3 of the difference between the crude kinetic energy estimator and the virial estimator. In constant pressure simulations, we can use this formula to verify that the estimated pressure is equal to the preset pressure.

1.3.5 Statistical errors

Computer simulation is an experimental science subject to systematic and statistical errors. Inserting periodic boundary conditions and tail corrections can compensate for the errors arising from the finite size of the simulation box. Another error endemic to MC simulations is that neighboring configurations are highly correlated, so that subsequent iterations may not give useful new information on a computed property. To compensate for this we need to determine the correlation length, which by definition is the average number of iterations necessary to provide new information about a property A.

Ceperley[19] proposed using the following formula to calculate the correlation length:

$$s = 1 + 2\sum_{k=1}^{\infty} \frac{\left\langle (A_o - \overline{A})(A_k - \overline{A}) \right\rangle}{\sigma^2(A)} \quad . \tag{1.34}$$

Here A_o is the initial value of A, A_k is the value of after the k^{th} iteration , $\overline{A} = \langle A \rangle$ is the mean over all iterations, and $\sigma^2(A) = \left\langle (A_k - \overline{A})^2 \right\rangle$ is the variance.

We follow instead the method proposed by Fincham, Quirke and Tildesley,[40] which is more straightforward to implement. At each of M steps, we save the computed values of the property A as well as the variance $\sigma^2(A)$. We then separate these results into n_b blocks each of length M_b (n_b M_b = M) and then calculate the mean value of A for each block

$$\langle A \rangle_b = \frac{1}{M_b} \sum_{i_b=1}^{M_b} A_{i_b} \quad , \tag{1.35}$$

where the sum runs over only the results in block b. We can estimate the variance for all the blocks

$$\sigma^2(\langle A\rangle_b) = \frac{1}{n_b}\sum_{b=1}^{n_b}(\langle A\rangle_b - \overline{A})^2 \quad . \tag{1.36}$$

We then define the correlation length s as the limiting ratio

$$s = \lim_{M_b\to\infty} \frac{M_b\sigma^2(\langle A\rangle_b)}{\sigma^2(A)} \quad . \tag{1.37}$$

The value of s is the number of additional MC iterations one must accumulate before the calculation of an average value of the property A will contribute significant new information. Tildesley *et al.* propose plotting the quantity $M_b\sigma^2(\langle A\rangle_b)/\sigma^2(A)$ against $M_b^{1/2}$ ($M_b^{1/2}$ is simply a convenient variable here, use of the square root as the abscissa compresses the data to makes an easier visible comparison) and then using graphical extrapolation to obtain the value of the correlation length s.

In addition, the precision of the calculated property A in the simulation is limited by an overall variance

$$\sigma_{run}(A) = \sqrt{s\sigma^2(A)/M} \quad . \tag{1.38}$$

To minimize statistical errors, it is essential that the total number of iterations be much greater than s. This defines a "well converged" run.[19]

Chapter 2: Path-integral Monte-Carlo investigation and spectral simulation of an Al atom doped in Helium

2.1 Introduction

In recent years extensive experimental studies of helium droplets and impurity doped helium droplets have appeared.[7,11] The helium environment is unique because the interaction between helium atoms is very weak. Helium is the lightest noble gas atom. Consequently, helium atoms have large zero-point motion and solidify only under pressure. In fact, helium clusters are known to be the only clusters that remain liquid under all conditions of formation.[41] Because the helium quantum liquids are highly homogeneous compared to traditional solid rare gas cryogenic matrices, problems of inhomogeneous line broadening do not occur, and matrix induced perturbations are minimized.

Helium clusters provide a unique quantum environment to study the low temperature spectra of isolated atoms or molecules. In the bulk, superfluid helium has the unique property of "self-cleaning"; that is, in bulk helium liquid impurities either aggregate or are absorbed onto the walls of the container. With the molecular beam techniques developed about a decade ago for impurity doped helium droplets,[3,11] experimentalists can now control impurity aggregation in helium droplets for isolation spectroscopy. In a molecular beam experiment, helium droplets undergo collisions with atoms or molecules formed in a free jet expansion. Some of the targets are absorbed into/onto the helium droplet. Subsequently, the surface helium atoms evaporate and cool the resulting droplet. By means of this technique, on can form ^{4}He clusters with $N \sim 10^3 - 10^4$ atoms (diameter 5–10 nm) at temperatures of T=0.3–0.4K.

The spectra of a wide range of species attached to or embedded in these nanoclusters have been measured.[3,11]

High-resolution spectra in helium droplets at 0.38K of the alkali atoms (Li, Na, K), as well as Al and Mg have been recorded by Lehmann, Scoles and coworkers.[4-6,8] These experiments revealed that the alkalis are attached to the surface of helium nanoclusters, while the Al and Mg atoms reside in the interior of the clusters. Other atomic dopants such as Eu and Ag have been observed to immerse completely into the helium droplet.[3] By contrast, experiment does not provide unambiguous information on the location of other alkaline earth atoms (Ca, Sr, Ba), with the exception of Mg. A possible explanation is that they are located in the region of low helium density near the surface.[3]

A semi-empirical criterion was proposed by Ancilotto *et al*, which compares the gain in energy due to the metal-helium pair interaction against the cost of creating a cavity within the liquid helium.[42] In this work, we will not deal with the solvation model of atoms in a finite helium droplet. Rather, we assume that the Al atom resides in the interior of the helium droplets, which was both predicted by a semi-empirical criterion and verified by experiment.[5]

Spectra of alkali atoms in helium droplets have been studied by density functional methods (Cs) and path-integral Monte-Carlo simulations (Li, Na, K) based on high-level *ab initio* calculations, including spin-orbit interactions.[41,43] Considerable effort has been devoted to the construction of accurate *ab initio* alkaline earth (Be, Mg, Ca, Sr, Ba)–helium pair potentials,[44-46] because it was found that the predicted spectra depended critically on the details of the pair-potentials used.[3] For Al atoms, Lehmann, Scoles and coworkers[5] used a semi-empirical Hatree-Fock, damped dispersion (HFD) approach to calculate the Al–He potential energy curves.

These authors used these potential energy surfaces to compare the lower –energy ($1^2\Pi_{1/2}$) spin-orbit-coupled surface to the spin-orbit free $1^2\Pi$ surface in

$AlHe_n$ (n=1, 4, 6–8), where the helium atoms are arranged symmetrically in the xy plane around the Al p_z orbital. They also carried out a density functional calculation in which Al was treated as a classical object in a quantum liquid. They conclude from their calculations that the Al electron density is localized in the Al p_z orbital, perpendicular to the plane occupied by the helium ligands

These simple calculations provide qualitative models for how the partially filled p electron shell in the Al electronic ground state affects the embedding of the atom into the cluster. Nevertheless, to describe accurately in simulations the many-body interactions of the open-shell atom is a difficult theoretical challenge. To our knowledge, no high level simulations have been presented for Al atoms in helium.

In this work, the ground and excited binary Al–He potentials were determined from accurate *ab initio* calculations. Subsequently we describe the interaction of Al in its ground ($3p\ ^2P$) state with multiple He atoms using the Balling and Wright model,[14] as we discussed in the previous chapter. In section 2.2 of this chapter, we present the relevant Al–He diatomic potential energy curves, followed by a Balling and Wright model description of the anisotropic interaction in excited states ^2D.

As discussed in the preceding Chapter, thermodynamic properties of quantum systems can be calculated accurately by path-integral, Monte-Carlo simulations, provided that the sampling converges in a reasonable amount of time. The easiest approach is the slice by slice sampling discussed in Chap. 1. However, the primitive Trotter approximation [Eq. (1.11) in Chap. 1] is accurate only to order $O[(\beta/p)^2]$. In order for simulations based on this primitive approximation to be valid, the trotter number p must be several thousands at the temperatures (T=0.3–0.4 K[47]) at which the spectroscopic measurements on impurity-doped helium clusters have been performed. This means thousands of integrals must be convoluted. The slice-by-slice sampling becomes slow and convergence requires large CPU times.

Improvement beyond the primitive approximation involves the use of more accurate low-temperature approximations to the density matrix. If this lowers the error, then the Trotter number can be significantly decreased.[19] The most successfully used is the pair-product form based on pair decomposition of the density matrix, which works perfectly for spherical interactions between helium atoms as well as between helium and spherical impurities like alkaline atoms.[41,47] However, when the helium-impurity interaction is not isotropic, it is more convenient to work within the primitive approximation for the helium-impurity interaction.[47,48] In this case, use of the pair decomposition approximation for the helium-helium interaction, while the primitive approximation is used for the helium-impurity interaction, does not result in a substantial improvement of the efficiency.[48] We, therefore, keep the primitive approximation in this work.

Another way to improve the sampling is to speed up convergence by better design of the Metropolis Monte-Carlo method. A review of this approach and an application to helium systems has been published by Ceperley.[19] The implementation used in our impurity-doped clusters is closely related to recent work on pure helium clusters by Chakravarty, Gordillo and Ceperley[49] and by Brualla.[50] Complete details will be given in section 2.3 below.

Subsequent to the PIMC simulation, we use a semiclassical Franck-Condon expression to calculate the electronic spectrum corresponding to the $3d \leftarrow 3p$, $4s \leftarrow 3p$, $4p \leftarrow 3p$ transitions of the Al chromophore, perturbed and shifted by the helium cluster. We then compare the $3d \leftarrow 3p$ spectrum with that observed experimentally by Lehmann, Scoles and coworkers,[5] and compare the $4s \leftarrow 3p$ spectrum with that of Al in bulk liquid helium by Takami *et al.*[51] We present the results and discussion in section 2.4. We conclude with a brief conclusion in section 2.5.

2.2 Al–He$_N$ potential energy surface

2.2.1 Diatomic potential energy curves

For the He–He interaction, we adopt the well-known Aziz potential.[52] To determine the Al–He ground state potentials, Alexander[53] used the coupled cluster (CCSDT) method with counterpoise corrections. Dunning's correlation consistent *avtz*, *avqz* and *av5z* basis sets were used. For the excited states, Alexander[53] used internally-contracted, multireference, configuration-interaction with the Davidson correction (IC-MRCI+Q) calculations. Basis sets of *avqz* and *av5z* were used in excited states. Calculations, done with the MOLPRO2000 program suite[54], were carried out at 25 different values of the Al–He distances R (3.25, 3.5, 3.75, 4.0, 4.25, 4.5, 4.75, 5.0, 5.25, 5.5, 5.75, 6.0, 6.25, 6.5, 7.0, 7.5, 8.0, 8.5, 9.0, 9.5, 10.0, 10.5, 12.0, 18.0 and 25.0 bohr). The ground state potentials were extrapolated to the infinite basis set limit using the Peterson-Dunning formula,[55] and the excited states were extrapolated to the infinite basis set limit using the two-point extrapolation by Martin and Taylor.[56-58] We fit all calculated potential curves to the following form:

$$V(R) = c_1 \exp(-\lambda_1 R) + (c_2 + c_3 R)\exp(-\lambda_2 R) - \tfrac{1}{2} c_4 \left[\tanh\{\alpha(R - \lambda_3)\} + 1\right] R^{-6} \qquad (2.1)$$

Figure 2.1 shows the calculated potential energy curves of the AlHe diatomic electronic states correlating with the Al ground states ($3s^2 3p\ ^2P$)+He and Al excited states ($3s^2 3d\ ^2D$)+He, ($3s^2 4s\ ^2S$)+He and ($3s^2 4p\ ^2P$)+He atomic asymptotes. Table 2.1 summarizes the binding energies (D_e) and the equilibrium internuclear distances (R_e) from these *ab initio* calculations.

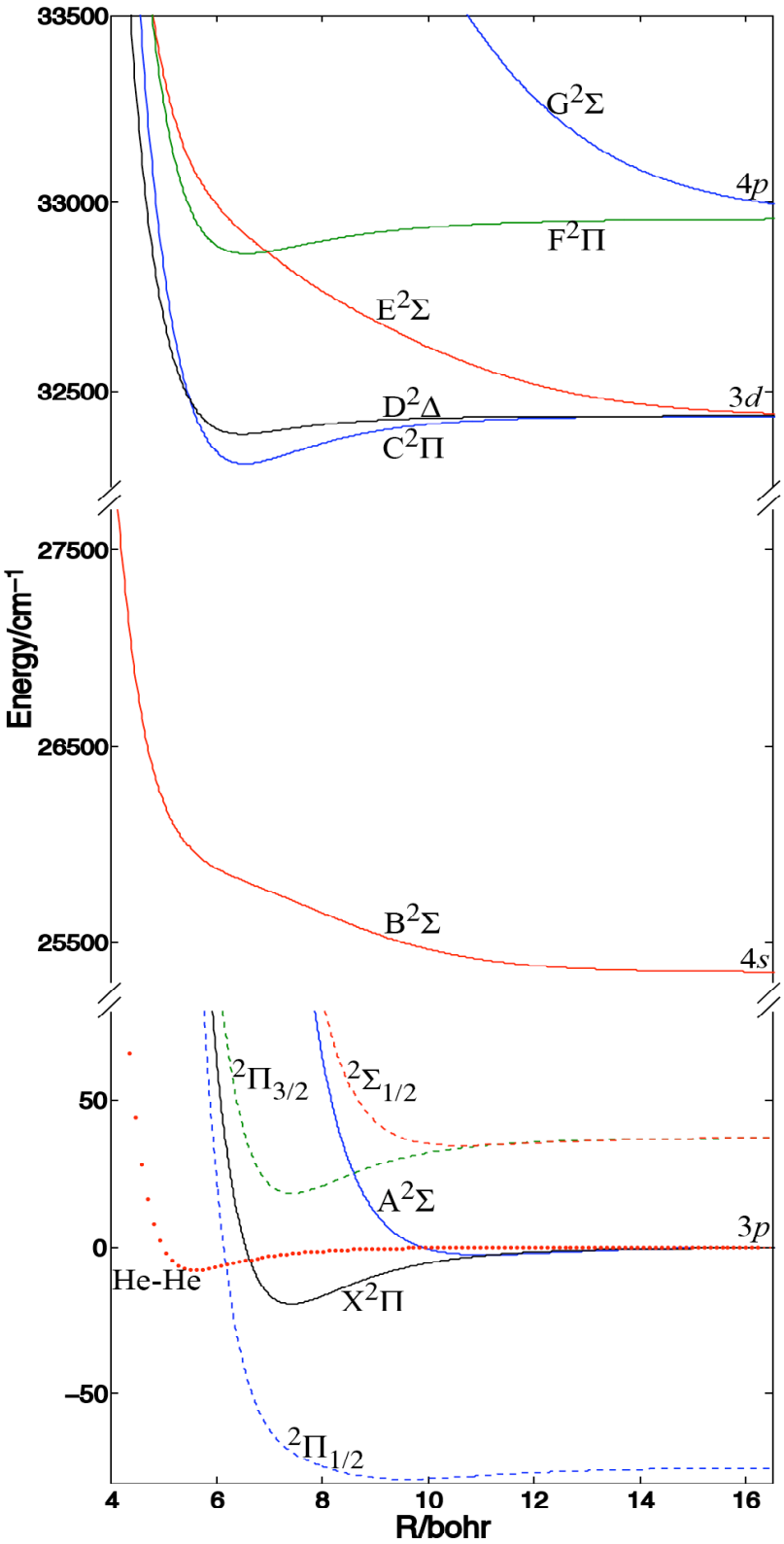

Fig 2.1AI–He potential energy curves obtained by *ab initio* calculations. The He-He interaction potential (dotted line) is also shown.

Table 2.1 Binding energy and equilibrium internuclear distance of the Al–He and He–He interaction. These values are not reported for states with purely repulsive potential curves.

asymptote	state	R_e/bohr	D_e /cm^{-1}
Al($4p\ ^2P$)–He	$^2\Sigma$	n/a	n/a
	$^2\Pi$	6.56	93.70
Al($4s\ ^2S$)–He	$^2\Sigma$	19.91	0.23
Al($3d\ ^2D$)–He	$^2\Sigma$	n/a	n/a
	$^2\Pi$	6.54	125.85
	$^2\Delta$	6.49	47.93
Al($3p\ ^2P$)–He	$^2\Sigma$	11.07	2.60
(ground state)	$^2\Pi$	7.43	19.34
	$^2\Sigma_{1/2}$	10.65	2.81
	$^2\Pi_{3/2}$	7.43	19.34
	$^2\Pi_{1/2}$	9.59	4.00
He–He		5.63	7.61

With the inclusion of spin-orbit coupling, the ground state Al ($3p$)–He potential splits into a lower $^2\Pi_{1/2}$ state and higher states $^2\Pi_{3/2}$ and $^2\Sigma_{1/2}$. For comparison, these states are plotted in Fig 2.1. The spin-orbit coupling constant for the Al ground state is A_{so}= 74.69 cm^{-1}.[18] In table 2.1, we see that when the spin-orbit coupling is not taken into account, the ground state diatomic interaction between Al and He ($3p\ ^2\Pi$) is more attractive than the interaction between two He atoms (D_e=19.34 cm^{-1} as compared with 7.61 cm^{-1}). However, when the spin-orbit coupling is included, the potential curve for the lowest Al–He state ($^2\Pi_{1/2}$), is less attractive than the He–He interaction. The effects of spin-orbit coupling are much smaller in the electronically excited states (A_{so}= 0.54 cm^{-1} for Al $3d$, and A_{so}= 10.55 cm^{-1} for Al $4p$)[18] and, consequently, are not shown here.

For computational expediency, we used a rapid table-lookup algorithm to interpolate the Al–He ground and excited state potentials, and the He–He potentials. The potential is first calculated at grids equispaced in r^{-2}, then algebraically interpolated.[24]

2.2.2 Al(^2D)–He$_N$ potential

To simulate the electronic transition spectrum semiclassically, we need to calculate the excited state electronic energy for all nuclear arrangements resulting from the PIMC simulation on the ground-state potential energy surface. The interaction between the five-fold degenerate ^2D excited state and multiple helium atoms is treated using the Balling and Wright approach discussed in Chapter 1.2. An identical model was employed by Krumrine *et al.*[12] in a previous study of the $^2D \leftarrow ^2P$ transition of B in the BAr_2 complex. For the binary Al–He complex, the matrix of the electrostatic interaction potential in the basis formed by the five spherical harmonics with l=2 (d functions) is diagonal and given by [similar to Eq. (1.2)] $\mathbf{V}(R)$

	d_{+2}	d_{+1}	d_0	d_{-1}	d_{-2}
d_{+2}	V_Δ	0	0	0	0
d_{+1}	0	V_Π	0	0	0
d_0	0	0	V_Σ	0	0
d_{-1}	0	0	0	V_Π	0
d_{-2}	0	0	0	0	V_Δ

(2.2)

with an identical 5×5 block for the $m_S = -1/2$ states

For a helium atom approaching at polar and azimuthal angles (θ, ϕ), the interaction matrix is transformed by the following rotation matrix

$$\mathbf{R}(\theta, \phi) = \mathbf{D}(\theta)\mathbf{E}(\phi) \tag{2.3}$$

where the elements of $\mathbf{D}(\theta)$ are the Wigner reduced rotation matrix elements $d^2_{m'm}(\theta)$.[59,60] Also, $\mathbf{E}(\phi)$ is a diagonal matrix with diagonal elements [$exp(2i\phi)$, $exp(i\phi)$, 1, $exp(-i\phi)$, $exp(-2i\phi)$].

The transformation matrix from the definite-m to Cartesian d-functions is

$$\mathbf{T} = \begin{array}{c|ccccc} & d_{x^2-y^2} & d_{xy} & d_{zx} & d_{yz} & d_{z^2} \\ \hline d_{+2} & 2^{-1/2} & -i2^{-1/2} & 0 & 0 & 0 \\ d_{+1} & 0 & 0 & 2^{-1/2} & -i2^{-1/2} & 0 \\ d_0 & 0 & 0 & 0 & 0 & 1 \\ d_{-1} & 0 & 0 & -2^{-1/2} & -i2^{-1/2} & 0 \\ d_{-2} & 2^{-1/2} & i2^{-1/2} & 0 & 0 & 0 \end{array} \tag{2.4}$$

The matrix of the full electronic interaction potential in the uncoupled Cartesian basis is therefore explicitly given by

$$\mathbf{V}_{3d}(R,\theta,\phi) = \begin{vmatrix} \mathbf{V}_{55} & 0 \\ 0 & \mathbf{V}_{55} \end{vmatrix} \tag{2.5}$$

where $\mathbf{V}_{55}$ is a 5×5 matrix (identical for both the $m_S = 1/2$ and $m_S = -1/2$ states). This is given by

$$\mathbf{V}_{55} = \mathbf{T}^T\mathbf{R}^T(\theta, \phi)\mathbf{V}(R)\mathbf{R}(\theta, \phi)\mathbf{T} \ . \tag{2.6}$$

For multiple ligands, the complete potential matrix is the sum of the 10×10 matrices for each ligand. The spin-orbit operator [see in Appendix 2.I, Eq. (2.1.2)] mixes the $m_S = 1/2$ states and $m_S = -1/2$ states. We diagonalize the 10×10 matrix which is the sum of the full **V** matrix and the spin-orbit matrix. The eigenvalues define, in an adiabatic sense, the excited state energy levels for our spectral simulation.

2.3 Cluster and spectral simulations

In this study, we will present calculations for Boltzmann statistics only, ignoring any quantum effects due to the bosonic (or fermionic) nature of the He cluster. A similar approach was reported recently in a theoretical determination of the rotational constant of OCS molecules doped into clusters of ^{4}He at the same temperature.[48]

The ^{4}He atoms have such a large zero-point motion that they frequently change place at low temperature. A dramatic consequence of the exchange is the superfluidity seen when ^{4}He is cooled below 2.17K. Exchange effects can be incorporated into the PIMC algorithm by including permutation sampling. In simulations of pure helium, it is found that only with inclusion of exchange can one describe accurately properties of the phase transition as well as the response of the system to rotation. Since permutation space is discrete, one can explicitly construct a transition table and call up the so-called "heat-bath" transition rule to accept or reject exchange moves.[19,47] The reason for our neglect of particle exchange is that because the permutation space is very sparse, the fraction of particles involved in the permutation movement is usually small.[19] Converge is slow, especially for simulations with large Trotter number *p*.

Also, we do not expect big discrepancies in the calculated spectra due to neglect of bosonic exchange. As was shown previously by Ceperley,[19] the difference in the pair-correlation functions of "distinguishable" and "indistinguishable" boson liquid helium is very small (only 2% at maximum) below the superfluid transition temperature. This means that the arrangement of helium atoms is not dramatically affected by the bosonic exchange. The effect of Bose-Einstein statistics is more obvious in dynamical properties of the system, such as the momentum distribution and rotational constant. Since our spectroscopic simulation only depends on differences in excited and ground state energies of the embedded Al atom, which are governed by the locations of the particles in the system, we do not expect siginificant discrepancies due to the neglect of particle exchange.

In this section we describe the multilevel Metropolis method and the Frank-Condon semiclassical spectra simulation. Although another important PIMC simulation method – the staging method – is not directly used in this work, it serves

as one justification for our use of the Levy construction in the multilevel Metropolis method. We outline the staging method in Appendix 2.II.

2.3.1 The Metropolis algorithm revisited

The central requirement in any simulation is finding a method to generate a sequence of random states so that by the end of the simulation each state has occurred with the appropriate probability. The solution is to set up a Markov chain of states.[24] A Markov chain is a sequence of trials that satisfies two conditions:[24]

1. The outcome of each trial belongs to a finite set of outcomes, $\{s_0, s_1, s_2, \ldots\}$, called the state space.
2. The outcome of each trial depends only on the outcome of the trial that immediately preceded it.

To construct a Markov chain, let us change the state of the system according to a fixed transition rule $P(s \rightarrow s')$. Repeated application of this transition rule will generate a random walk. For the state to converge to equilibrium, the transition probability must be ergodic, *i.e.*, one can move from any state to any other state in a finite number of steps with a nonzero probability.

The transition probability usually satisfies detailed balance:

$$\pi(s)\, P(s \rightarrow s') = \pi(s')\, P(s' \rightarrow s) \tag{2.7}$$

where $\pi(s)$ is the relative population of state s at equilibrium. If ergodicity is assumed, then the condition of detailed balance is sufficient to guarantee that in the limit of many steps, one will sample the limiting distribution $\pi(s)$.

We can factor the transition probability into an *a priori* sampling distribution $T(s \rightarrow s')$ and an acceptance probability $A(s \rightarrow s')$,

$$P(s \rightarrow s') = T(s \rightarrow s')\, A(s \rightarrow s') \ . \tag{2.8}$$

In the generalized Metropolis procedure[19] a trial move is accepted or rejected according to

$$A(s \to s') = \min\left[1, \frac{T(s' \to s)\pi(s')}{T(s \to s')\pi(s)}\right] \tag{2.9}$$

It is easy to verify that Eq. (2.9) satisfies the detailed balance condition. The probability $T(s \to s')$ can be chosen to be any convenient sampling distribution. In particular, in the original Metropolis procedure $T(s \to s') = T(s' \to s)$ is chosen to be a constant distribution inside a cube and zero outside. It then leads to the acceptance criterion $\exp(-\delta V)$ used in the algorithm introduced in Chapter 1, 1.3.2.

2.3.2 The Levy construction

The Levy construction is an early (1939) algorithm for sampling a free-particle path (V=0, only the kinetic energy component contributes to the effective potential). In the Levy construction of a Brownian bridge,[19,61] one starts with two fixed end points, $\mathbf{q}_0$ and $\mathbf{q}_\beta$. The middle point $\mathbf{q}_{\beta/2}$ is sampled exactly as

$$\mathbf{q}_{\beta/2} = \frac{\mathbf{q}_0 + \mathbf{q}_\beta}{2} + \eta\sqrt{\frac{\hbar^2\beta}{4m}} \tag{2.10}$$

where η is a normally distributed random vector, with mean zero and unit covariance. Because the sampling is exact, there are no rejections. By applying this algorithm recursively in two subintervals $(0, \beta/2)$ and $(\beta/2, \beta)$, we can generate the additional two points $\mathbf{q}_{\beta/4}$ $\mathbf{q}_{3\beta/4}$. The algorithm continues: one doubles the number of sampled points at each level, until the difference between intervals is $\tau = \beta/p$.

A proof that the Levy construction exactly samples the free particle density matrix is given in Appendix 2.II. This simple yet powerful sampling method, combined with the multilevel method discussed in the next subsection, can significantly accelerate simulations of interacting quantum systems at finite temperature.

2.3.3 Multilevel Metropolis method

The multilevel Metropolis method is a general sampling technique[19,62] that links together several accept/reject steps. In cases where the probability function is difficult to compute or where the trial move is hard to construct and hard to get accepted, we can first evaluate a crude estimate:

$$A^*(s\to s') = \min\{1, \pi^*(s')T^*(s'\to s) / [\pi^*(s)T^*(s\to s')]\} \quad . \tag{2.11}$$

Then we have many rejections without doing too much work, because we either calculate a simpler (approximate) probability function, or reject unlikely trial moves at an early stage. In the rare case that this crude estimate gets accepted, one subsequently performs a second, accurate accept/reject step by including the initial crude estimate in the final accept/reject probability:

$$A''(s\to s') = \min\{1, \pi(s')T(s'\to s)\,\pi^*(s)T^*(s\to s') / [\pi(s)T(s\to s')\pi^*(s')T^*(s'\to s)]\} \tag{2.12}$$

This multilevel algorithm can be generalized to include several intermediate steps. Suppose we partition the configuration state s into l+1 levels (s_0, s_1, …, s_l), where s_0 remains fixed, the coordinates belonging to s_1 are to be sampled in the first level, s_2 in the second level, and so on. (s_0', s_1', …, s_l') are the new trial positions, with $s_0'=s_0$. The distribution at the finest level must be exact:

$$\pi_l(s_0, s_1, \ldots, s_l) = \pi(s) \tag{2.13}$$

With a sampling rule T_k at level k, the sampling level k is accepted with probability

$$A_k(s') = \min[1, \frac{T_k(s_k)\pi_k(s')\pi_{k-1}(s)}{T_k(s_k')\pi_k(s)\pi_{k-1}(s')}] \tag{2.14}$$

If level k sampling is accepted, we go on to the next level; if not, we go back to the very beginning and start a new partitioning. In the first level, π_0 is canceled out because s_0 remains fixed. The acceptance probability is constructed to satisfy detailed balance at each level:

$$\frac{\pi_k(s)}{\pi_{k-1}(s)} T_k(s'_k) A_k(s') = \frac{\pi_k(s')}{\pi_{k-1}(s')} T_k(s_k) A_k(s') \tag{2.15}$$

as well as in the overall movement from $s \to s'$.

$$\pi(s) P(s \to s') = \pi(s') P(s' \to s) \tag{2.16}$$

where

$$P(s \to s') = \prod_{k=1}^{l} T_k(s'_k) A_k(s') \tag{2.17}$$

Eq. (2.16) can be proved by multiplying Eq. (2.15) from 1 to l.

We use the Levy construction in the sampling rule T_k. Since the Levy construction samples the kinetic energy component in the path exactly, the rejection/acceptance criterion only involves the potential energy component. For a total level number of l, we pick up a segment of length 2^l+1 from the chain of the pseudoparticles. With the two ends fixed, we sample the middle point from the Levy construction and accept or reject according to the potential energy criterion. This is the first level or coarsest level sampling. If the coarsest level is accepted, we continue to divide each side into half and sample the two new middle points from the Levy construction. The acceptance/rejection criterion depends on the potential energy change at this level, as well as that in the previous level. Note the two displacements must be accepted together, because they belong to the same level. Otherwise they are rejected. We continue with this binary division process until we reach the finest level. Fig 2.2 is a schematic of a multilevel sampling of $l = 3$.

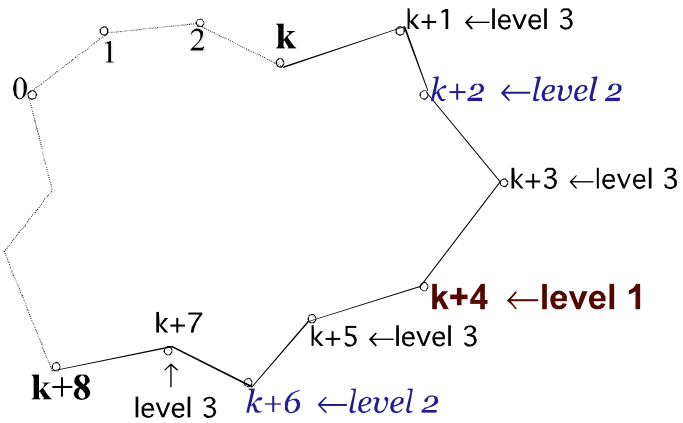

Fig 2.2 Graphical illustration of the algorithm with a three-level (l=3) sampling. Each point here represents a pseudo system with one Al and n_{He} He atoms.

The detailed algorithm can be illustrated graphically as follows:

1. *Pick out a segment of the chain*

2. *Fix the two ends*

Update the middle point. Accept with an approximate probability A_1, or reject and return to the first step (this defines the coarsest level)*

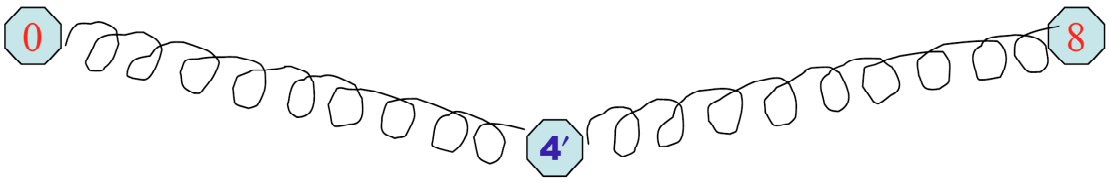

The coordinate $\mathbf{q}_4$ is sampled using

$$\mathbf{q}_4{}' = \frac{\mathbf{q}_0 + \mathbf{q}_8}{2} + \eta\sqrt{\frac{2\tau\hbar^2}{m}} \tag{2.18}$$

where η is a normally distributed random vector with zero mean and unit variance, with dimension equal to that of the coordinates $\mathbf{q}$. We then compute $U(\mathbf{q}_4;4\tau)$ and $U(\mathbf{q}_4';4\tau)$ given by

$$U(\mathbf{q};k\tau) = k\tau\, V(\mathbf{q}) \tag{2.19}$$

The difference in U is

$$\delta U_{4\tau} = U(\mathbf{q}_4';4\tau) - U(\mathbf{q}_4;4\tau)\ . \tag{2.20}$$

We then proceed to the next step with probability

$$A_1^* = A_{4\tau} = \min[1, \exp(-\delta U_{4\tau})] \tag{2.21}$$

3. *Update new middle points of the resulting chain. Accept with an approximate probability A_2^*/A_1^*, or reject and return to first step*

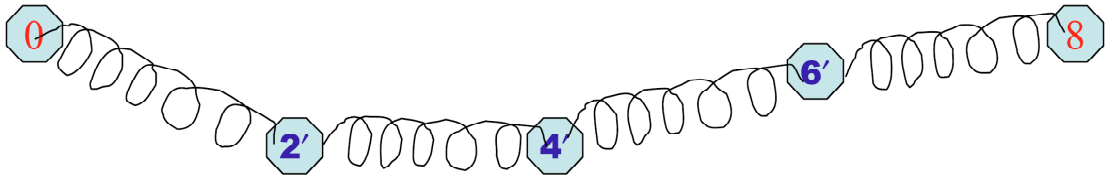

The coordinates $\mathbf{q}_2$ and $\mathbf{q}_6$ are sampled using

$$\begin{aligned} \mathbf{q}_2' &= \frac{\mathbf{q}_0 + \mathbf{q}_4'}{2} + \eta\sqrt{\frac{\tau\hbar^2}{m}} \\ \mathbf{q}_6' &= \frac{\mathbf{q}_4' + \mathbf{q}_6}{2} + \eta\sqrt{\frac{\tau\hbar^2}{m}} \end{aligned} \tag{2.22}$$

We then compute

$$\delta U_{2\tau} = U(\mathbf{q}_2';2\tau) - U(\mathbf{q}_2;2\tau) + U(\mathbf{q}_6';2\tau) - U(\mathbf{q}_6;2\tau) \tag{2.23}$$

and proceed to the next step with probability

$$A_2^*/A_1^* = A_{2\tau} = \min[1, \exp(-\delta U_{2\tau} + \delta U_{4\tau})] \tag{2.24}$$

Where A_2^* refers to the "local" probability in this level — $\exp(-\delta U_{2\tau})$.

4. *Update the middle points at the finest level. Accept with probability A_3/A_2^*, or reject and return to first step. Here A_3 should correspond to the exact distribution.*

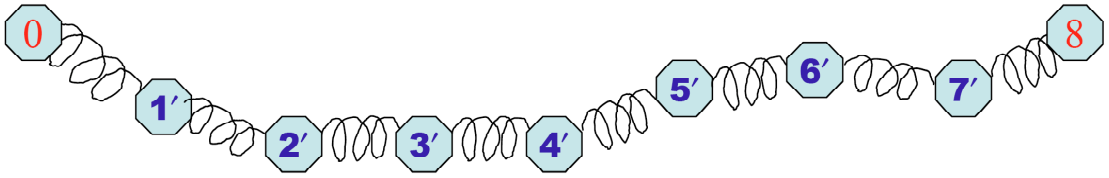

The coordinates of $\mathbf{q}_1'$, $\mathbf{q}_3'$, $\mathbf{q}_5'$ and $\mathbf{q}_7'$ are sampled using the same Levy construction with steps divided by 2:

$$\begin{aligned}
\mathbf{q}_1' &= \frac{\mathbf{q}_0 + \mathbf{q}_2'}{2} + \eta\sqrt{\frac{\tau\hbar^2}{2m}} \\
\mathbf{q}_3' &= \frac{\mathbf{q}_2' + \mathbf{q}_4'}{2} + \eta\sqrt{\frac{\tau\hbar^2}{2m}} \\
\mathbf{q}_5' &= \frac{\mathbf{q}_4' + \mathbf{q}_6'}{2} + \eta\sqrt{\frac{\tau\hbar^2}{2m}} \\
\mathbf{q}_7' &= \frac{\mathbf{q}_6' + \mathbf{q}_8}{2} + \eta\sqrt{\frac{\tau\hbar^2}{2m}}
\end{aligned} \tag{2.25}$$

Note that at the last level, all the points have been updated, except the two ends of this segment. The finest level is accepted by the probability

$$A_3/A_2^* = A_\tau = \min[1, \exp(-\delta U_\tau + \delta U_{2\tau})] \tag{2.26}$$

Only when this level is accepted, do we replace the old configuration by the new one. If it is rejected, the algorithm returns back to the very beginning with all the original positions restored.

After using all the approximate probabilities Eqs. (2.21), (2.24) and (2.26), we have indeed sampled the exact distribution

$$\exp(-\delta U_{4\tau}) \bullet \exp(-\delta U_{2\tau} + \delta U_{4\tau}) \bullet \exp(-\delta U_\tau + \delta U_{2\tau}) = \exp(-\delta U_\tau) \tag{2.27}$$

The evaluation of thermodynamic properties must be done only after a decision has been made to accept or reject the finest level (in the latter case, the system is returned to the original configuration). Only then does the state sample the exact distribution.

In the standard application of the Metropolis algorithm described in Chap 1, 1.3.2, the pseudoparticles are moved slice by slice, the movements are small, and in each movement the effective potential of Eq. (1.17) must be calculated. In practical terms, it is time consuming to move away from a starting point. In contrast, the advantage of the multilevel Metropolis method is that large and coarse displacements are sampled in the beginning. If they are not accepted, then time is not wasted on performing small displacements that are unlikely to be accepted. Thus we save computational effort and can move much faster through phase space.

2.3.4 Spectral simulation

The Franck-Condon principle states that the nuclear coordinates of a molecule remain fixed during an electronic transition. The general application of this principle was proposed by Lax half a century ago.[63] For a recent derivation, see Cheng and Whaley.[64] In a form appropriate for our PIMC simulation,[12] we have the following expression for the relative absorption at frequency ω corresponding to a transition from the electronic ground state of Al to the i^{th} component of the ten $3d$ states.

$$I_i(\omega) \propto \int d\mathbf{q} e^{-\beta V_{eff}} \delta\left[V_{3d_i}(\mathbf{q}) - V_{3p}(\mathbf{q}) - \hbar\omega\right] \left|\left\langle \phi_{e_i} | \mu | \phi_g \right\rangle\right|^2 \Big/ \int d\mathbf{q}\, e^{-\beta V_{eff}} \quad (2.28)$$

where V_{3p} is the potential energy of Al in its electronic ground state embedded in helium and V_{3d} is the corresponding energy of Al in its $3d$ excited state, evaluated at the same position. Because the helium-helium interaction is pairwise additive in our simulation, and the positions of the He atoms do not change in a Franck-Condon transition, the contribution of the helium-helium interactions cancel inside the delta function.

In particular, V_{3p} is the lowest eigenvalue of the sum of the 6×6 potential matrix (1.5) and the spin-orbit matrix (1.6). Also, V_{3d_i} corresponds to the i^{th} root of the diagonalization of the sum of the Al($3d$)–He Hamiltonian matrices [Eq. (2.15)] plus the matrix of the spin-orbit operator in the basis of the 10 $3d$ states. Here also $\left|\left\langle \phi_{e_i} | \mu | \phi_g \right\rangle\right|^2$ is the square of the transition dipole, and $e^{-\beta V_{eff}} \Big/ \int d\mathbf{q}\, e^{-\beta V_{eff}}$ is the Boltzmann normalization factor corresponding to the distribution of the ground state Al–$(He)_N$ cluster.

It is generally[39,65] assumed that the electronic transition dipole moment is independent of the nuclear coordinates. This constitutes the Condon approximation. So when one (or both) of the electronic states involved in the nominally atomic electronic transition is spherical (S symmetry), the transition dipole is simply a constant which can be brought outside of the integral and ignored.[17,41,64,66]

However, this cannot be done in our case where the ground state is *P* and the excited state is *D*. A similar complication arose in the work by Krumrine *et al.* on the $2s2p^2 \leftarrow 2s^2 2p$ absorption spectrum of the $B(Ar)_2$ complex.[12]

To evaluate $\left|\left\langle \phi_{e_i} \left| \mu \right| \phi_g \right\rangle\right|^2$, we use the Wigner-Eckart theorem.[60,67]

$$\left\langle j'm' \left| T_q^k \right| jm \right\rangle = (-1)^{j'-m'} \begin{pmatrix} j' & k & j \\ -m' & q & m \end{pmatrix} \left\langle j' \left\| T^k \right\| j \right\rangle \tag{2.29}$$

where T_q^k is the q ($q = -k, -k+1, \ldots, k$) component of a rank k tensor, T^k, and $\begin{pmatrix} j' & k & j \\ -m' & q & m \end{pmatrix}$ is a Wigner 3*j* symbol. The double-bar matrix element is independent of m, m' and q.

At each value of the nuclear coordinates which are the output of the PIMC simulation, both the excited and ground state wavefunctions $\left|\phi_{e_i}\right\rangle$ and $\left|\phi_g\right\rangle$, are each linear combinations of the two spin components of the uncoupled Cartesian basis wavefunctions $d_{x^2-y^2}, d_{xy}, d_{zx}, d_{yz}$, and d_{z^2} or p_x, p_y, and p_z, respectively To use the Wigner-Eckart theorem, we further transform these Cartesian besis functions into definite-*m* basis functions, obtaining

$$\left\langle \phi_{e_i} \left| \mu \right| \phi_g \right\rangle = \sum_{j=1}^{10} \sum_{l=\{-2,-\bar{2}\}}^{\{2,\bar{2}\}} \sum_{k=1}^{6} \sum_{m=\{-1,-\bar{1}\}}^{\{1,\bar{1}\}} \left\langle \phi_{e_i} \left| d_j \right\rangle \left\langle d_j \left| d_l \right\rangle \left\langle d_l \left| \mu \right| p_m \right\rangle \left\langle p_m \left| p_k \right\rangle \left\langle p_k \left| \phi_g \right\rangle \right. \right. \right. \right. \right. , \tag{2.30}$$

where d_j designates one of the 10 uncoupled Cartesian *d* functions and d_l designates one of the definite-*m d* functions. The symbols p_k and p_m are the corresponding notations for the Cartesian and definite-*m* functions for the ground 3*p* state. Also $\left\langle \phi_{e_i} \left| d_j \right\rangle \right.$ and $\left\langle p_k \left| \phi_g \right\rangle \right.$ designate the expansion coefficients of the excited and ground adiabatic electronic states in terms of the Cartesian states. The matrix elements $\left\langle d_j \left| d_l \right\rangle \right.$ and $\left\langle p_m \left| p_k \right\rangle \right.$ are the elements of the transformation between the Cartesian and definite-*m* bases.

The matrix element $\langle d_l|\mu|p_m\rangle$ can be evaluated using the Wigner-Eckart theorem because the dipole operator μ is a rank one tensor. In an unpolarized electric field we have:[67]

$$\begin{aligned}\langle d_l|\mu|p_m\rangle &\propto \langle d_l|\mu_x|p_m\rangle + \langle d_l|\mu_y|p_m\rangle + \langle d_l|\mu_z|p_m\rangle \\ &= \left\langle d_l\left|2^{-1/2}(-1+i)\mu_{+1}\right|p_m\right\rangle + \left\langle d_l\left|2^{-1/2}(1+i)\mu_{-1}\right|p_m\right\rangle + \langle d_l|\mu_0|p_m\rangle\end{aligned} \tag{2.31}$$

Since the electronic excitation is confined to the Al atom, and since the He atoms result in only a weak perturbation, we shall assume that the magnitude of the Cartesian dipole matrix elements are independent of geometry and dependent only on the dipole selection rules contained in the three matrix elements of Eq. (2.31). The values of the matrix elements in the Cartesian basis

$$\langle d_j|\mu|p_k\rangle = \sum_l\sum_m \langle d_j|d_l\rangle\langle d_l|\mu|p_m\rangle\langle p_m|p_k\rangle \tag{2.32}$$

are given in the following table, in units of $\mu=\mu_x=\mu_y=\mu_z$.

	p_x	p_y	p_z
$d_{x^2-y^2}$	$-\sqrt{3}$	$\sqrt{3}$	0
d_{xy}	$-\sqrt{3}$	$-\sqrt{3}$	0
d_{zx}	$\sqrt{3}$	0	$\sqrt{3}$
d_{yz}	0	$\sqrt{3}$	$\sqrt{3}$
d_{z^2}	1	1	–2

(2.33)

The other two terms in Eq. (2.30), the expansion coefficients, are identical to the eigenvectors obtained from diagonalizing the corresponding potential+spin-orbit matrix. These depend on the geometry of all the atoms. Thus, apart from a constant factor, the value of $\langle \phi_{e_i}|\mu|\phi_g\rangle$ for a given arrangement of the nuclear coordinates is obtained from two matrix multiplications between the transition dipole matrix [Eq. (2.33)] and the matrices of ground and excited state eigenvectors.

In our PIMC simulation we sample only a finite number of nuclear coordinates. Consequently, we approximate the delta function in Eq. (2.28) by a boxcar histogram: the spectral region under investigation is divided into equally spaced bins of width $\delta\omega$. For each integration point, the weight $\left|\left\langle \phi_{e_i} | \mu | \phi_g \right\rangle\right|^2$ is assigned to the particular bin in which $V_{3d}(\mathbf{q}) - V_{3p}(\mathbf{q})$ lies. We use a bin width of 5 cm^{-1}. Finally, the total spectral intensity at frequency ω is obtained by summing over the intensity associated with the transition to each of the 10 3*d* excited states.

We use same approach to simulate the Al $4p \leftarrow 3p$ excitation spectra in helium cluster. The dipole matrix in the Cartesian basis for a $p \leftarrow p$ transition, similar to Eq. (2.33), is given by

	p_x	p_y	p_z
p_x	0	−1	1
p_y	1	0	−1
p_z	−1	1	0

(2.34)

2.4 Results and discussion

We performed path-integral Monte-Carlo simulation at T=0.38 K, the temperature in the experiments of Scoles, Lehman and co-workers.[5] A total of 121 particles are included in a box with size appropriate to the density of bulk liquid helium, namely 0.0218Å^{-3}.[11] When Al is doped, one Al atom replaces a helium atom without change in the box. In the experiments, the average cluster size $\langle N \rangle$ is ≈4000.[11] Consequently, the diameter of the cluster is at least three times larger than our box size, so that periodic boundary conditions can be used. The standard "mininum image" convention is used,[24] and a spherical cutoff of the potentials is set to half the side length of the periodic box. The Trotter number *p* is set to 2700.

There are two basic types of moves we used: The first corresponds to the bisection method we discussed previously. Here caution must be taken to ensure that the two fixed ends are in the same box when periodic boundary conditions are used.

Since the trial movements are constructed by the Levy construction, there is no adjustable step size here, in contrast to the standard Metropolis method. Instead, the only parameter is the bisection level. For a total bisection level of 3, we obtained an overall bisection acceptance ratio about 12%.

The other move is a classical motion, which is inserted to improve the convergence of the algorithm.[49,50] This is a collective motion of all the 2700 pseudoatoms corresponding to a given atom (Al or He). In this motion all the pseudoatoms are displaced by the same amount, with the displacement chosen uniformly in a cube of size Δ_{cm}. Since this "classical" displacement move does not alter the inter-pseudoatom distances associated with the chosen atom, the acceptance criterion of the trial displacement is based entirely on the change in potential energy (min[1, $exp(-\beta\Delta V)$]).

This is equivalent to a classical motion of a "particle" consisting of p pseudoparticles. Although this motion does not change the chain structure, it helps to maximize the movement through phase space. For a displacement Δ_{cm} for the helium atoms of 0.015 bohr (and 1/3 of that for the Al atom), we reach an acceptance ratio for the "classical" movement of ~50%. Because this classical displacement takes longer than a bisection movement (since potentials of all p pseudosystems need to be updated), we attempt it less frequently. We perform one classical movement for every atom after every 500 bisection movements.

The simulation is carried out with blocks of movements. Each block consists of 500 bisection movements and one center of mass movement for all atoms. Over 6000 of these blocks were done prior to accumulating data for analysis. Then, unless otherwise stated, an additional 3000 blocks were carried out, for which data was recorded.

2.4.1 Structure of the Al doped helium cluster

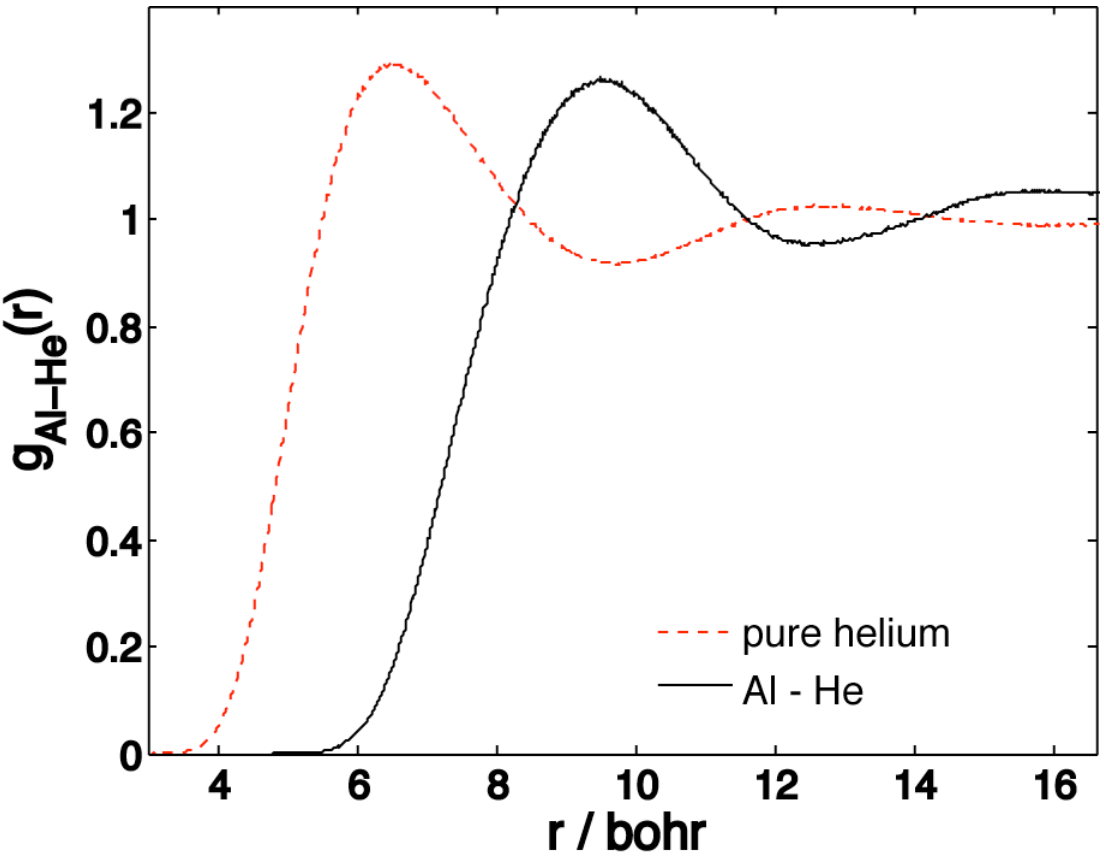

Fig 2.3 Al–He pair correlation functions for one Al atom doped in helium. For comparison, the pair correlation function for pure helium is also shown.

Insight into the structural changes of the liquid upon addition of an Al atom is given by the Al–He pair correlation function $g_{\mathrm{Al–He}}(r)$ shown in Fig 2.3. This is compared here with the correlation function for pure helium. The He–He pair correlation function peaks at a distance (6.54 bohr) substantially longer than the He_2 equilibrium internuclear distance predicted by the Aziz potential (5.63 bohr). This is because in the very anharmonic He_2 potential the large zero-point motion results in an average He–He distance which is somewhat larger than the position of the minimum.

When one Al atom replaces a helium atom, we see from Fig. 2.3 that the Al atom pushes the surrounding helium atoms away, relative to the He–He spacing. This

is a consequence, as shown in Fig. 2.1, of the longer minimum in the binary Al–He interaction as compared to He_2. This repulsion will create a helium cavity around the Al atom. The first shell of the Al–He pair correlation function peaks at ~9.45 bohr, close to the position of the minimum of the lowest of the spin-orbit-coupled binary Al–He potential curves ($^2\Pi_{1/2}$, r_e=9.6 bohr, see Fig. 2.1), but much larger than the minimum in the spin-orbit-free $^2\Pi$ potential (r_e=7.4 bohr). This is evidence that the spin-orbit coupling cannot be neglected.

Also, the width of the first peak is substantially greater than in the case of pure helium. This suggests that the distribution of helium around Al is not as uniform as in pure liquid He. However, we see no clear splitting of this peak. This type of splitting is apparent when Al is solvated in solid *para*-hydrogen, which we will discuss below in Chapter 4 of this dissertation. Because of the liquid character of the solvent with a consequent disordering of the structure, the effect of the anisotropy of the Al electronic distribution on the pair correlation function is blurred out.

Table 2.2 Energetic values from PIMC simulations of a helium cluster with a doped atomic Al impurity at 0.38K. The simulations consisted of a total of N =121 particles and were carried out with a Trotter number p=2700. The results are based on 3000 configurations from each run. The energies were computed from expressions given in Sec. 1.3.4. The quantities E_k and U are the kinetic and potential energies. E_k/N is the kinetic energy per He atom [In the case of the doped helium cluster, it is $E_k/(N-1)$]. The errors are estimated using the analysis described in section 1.3.5.

	U (cm^{-1})	$E_{k\mathrm{He}}/N$ (cm^{-1})	$E_{k\mathrm{Al}}$ (cm^{-1})
Pure helium	−1463.7±1.8	7.56±0.07	
Al + helium	−1580.2±3.3	7.69±0.08	3.20±1.10

Table 2.2 lists the total potential energies of 121 helium atoms and the total potential energy of one Al atom plus 120 helium atoms, as well as the average kinetic energy per atom. The well depth of the Aziz potential[52] we used to describe the He–He interaction has a minimum of -3.89 cm^{-1} at a distance of 6.77 bohr. For a He atom in an hcp lattice with 12 nearest neighbors, an estimate of the potential energy per He can be obtained by multiplying this well depth of -3.89 cm^{-1} by 12/2 (we divide by 2 to eliminate double counting), ~ -23 cm^{-1}. From Table 2.2 we find that the average potential energy per atom in pure helium, $-1463.7/121 \sim -12.1$ cm^{-1}, is only half the value, because the quantum He liquid is a much more disordered state than a rigid hcp lattice.

When one Al atom replaces a helium atom, the total potential energy decreases by ~106 cm^{-1}. This implies that it is energetically favorable for Al to reside inside the helium droplet. We observe that the kinetic energy of the He atoms is very large compared to the thermal energy at 0.38K ($3/2kT = 0.39$ cm^{-1}). This is a direct measure of the large zero-point motion of the He atom. By contrast, the kinetic energy of the Al atom is smaller, which indicates that the more massive Al atom behaves more classically at 0.38K.

The strength of the He–He interaction at distance of the first peak in the He–He $g(r)$ is ~ -4.85 cm^{-1}, while that of the Al–He $^2\Pi$ interaction at the first peak in the Al–He $g_{\text{–He}}(r)$ is ~ -7.31 cm^{-1}. At that same point the Al–He $^2\Pi_{1/2}$ potential is ~ -3.99 cm^{-1}. These energies alone do not account for the decrease of 106 cm^{-1} when one Al atom replaces a helium atom. A possible explanation is that the distortion engendered by the Al atom on the helium droplet compresses the liquid around the Al atom and thereby decreases the range of helium zero point motion. The process is accompanied by a gain in total potential energy, because the distance between helium atoms is reduced.

2.4.2 Absorption spectra

Fig 2.4 shows the predicted Al ($3^2D \leftarrow 3^2P$) absorption spectrum from the Franck-Condon simulations as described in section 2.3.4. The spectra is blue shifted from the positions of the $3^2D_{3/2} \leftarrow 3^2P_{1/2}$ and $3^2D_{5/2} \leftarrow 3^2P_{3/2}$ transitions in the isolated atom (32435 and 32325 cm^{-1}, respectively[18]). The blue shift and broadening are a result of the solvation of Al in the helium.[5] The large blue shift is due to the stronger repulsion between the helium cavity and the Al 3*d* excited state as compared to the Al 3*p* ground state.

The upper panel of Fig 2.4 shows the calculated spectrum from the simulation. We see that the shape, width and relative intensity as a function of frequency of the calculated spectrum is in moderately good agreement with experiment. However, the blue shift of the predicted spectra is ~200 cm^{-1} less than seen in the experiment, where the blue shift is about 1000 cm^{-1}. This disagreement may be due to errors in the *ab initio* potential curves, or, more likely, because we use a relatively small box of 121 particles, while the experiment is carried out in nanodroplets consisting of thousands of atoms.

As will be described in more detail in Appendix 4.II, we carried out an estimate of the tail correction of the total potential energy to correct for the finite size of our simulation box. The formula we use is

$$4\pi\rho\int_{r_c}^{\infty} r^2 V(r)dr \tag{2.35}$$

Here the cutoff radius r_c is set to be half of the box length. The calculated tail corrections are listed in Table 2.3. Note that we used averaged potentials for each of the asymptotic atomic states, because at large Al–He distance the spatial orientation of the Al electron has only a small effect.

Because the $E^2\Delta$ state of Al (3*d*)–He interaction has a long repulsive tail, the excited state of Al (3*d*) has a large positive tail correction to the potential energy. To

compensate for this we add 174 cm^{-1} to the 3*d* excited state energy. If we further add the ground state tail correction of –11 cm^{-1}, we obtain an additional blue shift of 185 cm^{-1}. The resulting spectrum, shown in the lower panel of Fig 2.4, is now much closer to the experiment.

Table 2.3 Calculated tail corrections

		ΔU (cm^{-1})
He–Al 3*p*	$(2\bullet X^2\Pi+A^2\Sigma)/3$	−11.24
He–Al 3*d*	$(2\bullet D^2\Delta+2\bullet C^2\Pi+E^2\Sigma)/5$	174.18
He–Al 4*s*	$B^2\Sigma$	−40.00
He–Al 4*p*	$(2\bullet F^2\Pi+G^2\Sigma)/3$	−8.54
He—He		−0.18

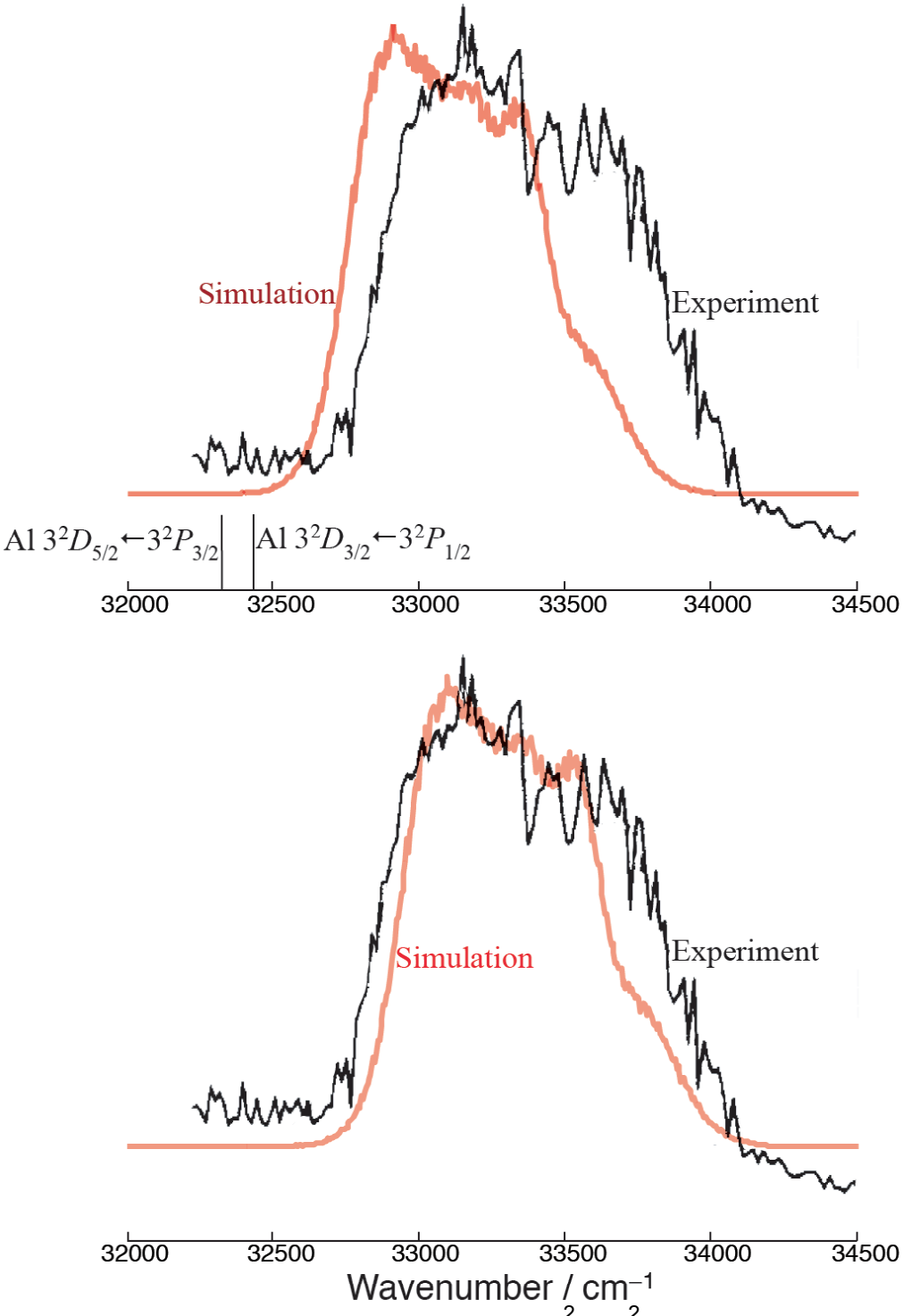

Fig 2.4 Predicted and experimental spectra for the Al $3^2D\leftarrow 3^2P$ transition in helium. Upper panel: calculated spectrum without tail correction; Lower panel: calculated spectrum shifted by tail correction. In both panels the experimental spectrum is from Ref. 5.

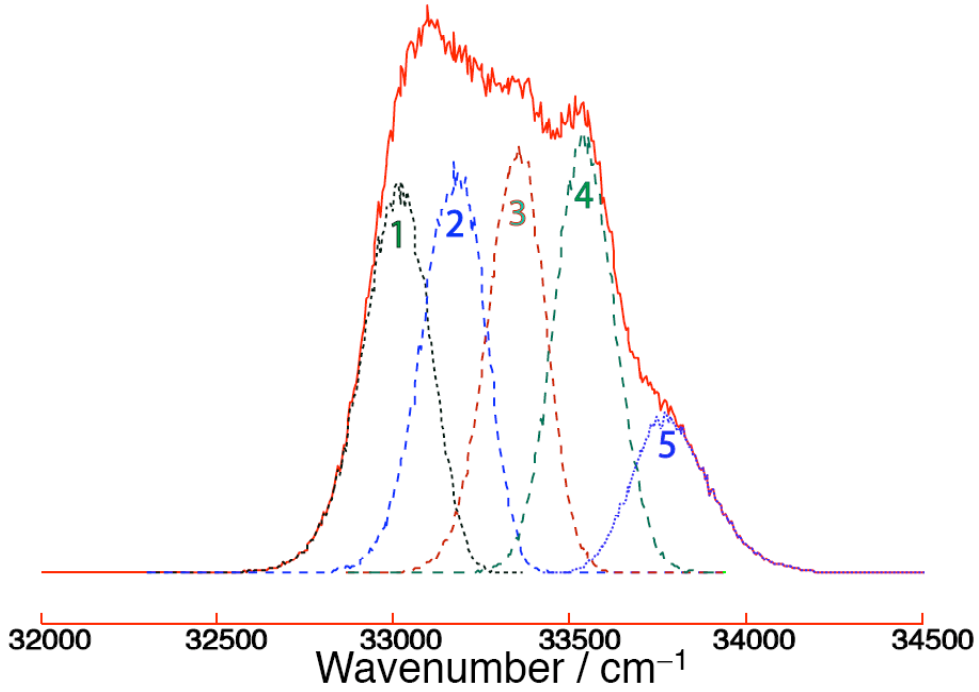

Fig 2.5 Contribution to the overall excitation spectrum of transitions to each of the five electronic states of Al (3*d*).

In previous work[12] on the BAr_2 complex, each electronically adiabatic excited state was found to be close in character to one of the asymptotic 3*d* diabatic states ($D_{x^2-y^2}$, D_{z^2}, D_{xy}, D_{xz}, D_{yz}). Consequently, the total spectrum could be analyzed nicely in terms of contributions from transitions into each diabatic state. The peaks in the spectrum could then be assigned, separately, to these individual transitions.[12]

Here, however, all five diabatic states are strongly coupled by the interaction with the surrounding helium atoms so that all asymptotic atomic states make a substantial contribution to each adiabatic state. We can, therefore, only assign the spectrum in terms of contributions into the five adiabatic states labeled 1, 2, 3, 4 and 5. This is shown in Fig 2.5. We find that the first four states contribute with almost equal intensity, at different frequencies. In contrast, the 5^{th} state contributes a smaller and flatter peak at the blue end of the absorption peak. The separation between the 1^{st}

and 5^{th} adiabatic states is about 1800 cm^{-1}. As we observe in Fig 2.1, this difference in energy is consistent with the separation between the lowest $C^2\Pi$ and highest $E^2\Delta$ potential energy curves of the binary Al($3d$)–He complex at an internuclear distance corresponding to the first peak in the Al–He correlation function (8–11 bohr).

Fig 2.6 shows the predicted spectrum for the higher energy (see Fig. 2.1) Al $4^2S \leftarrow 3^2P$ transition in helium, compared with the experimental[51] spectrum. These are plotted as a function of wavelength rather than frequency, to correspond to Ref. 51. The spectra are also blue shifted from the corresponding atomic transition. Although the both spectra have the same width and shape, the blue shift in the simulated spectrum is larger: ~25 nm, or, equivalent, ~2000 cm^{-1}). This difference is too large to be attributed to the missing tail corrections (Table 2.3). We note, however, the experiment was carried out at 1.7K, nearly a factor of five higher than the temperature of our simulation temperature, and furthermore the experiment was done in bulk liquid He.

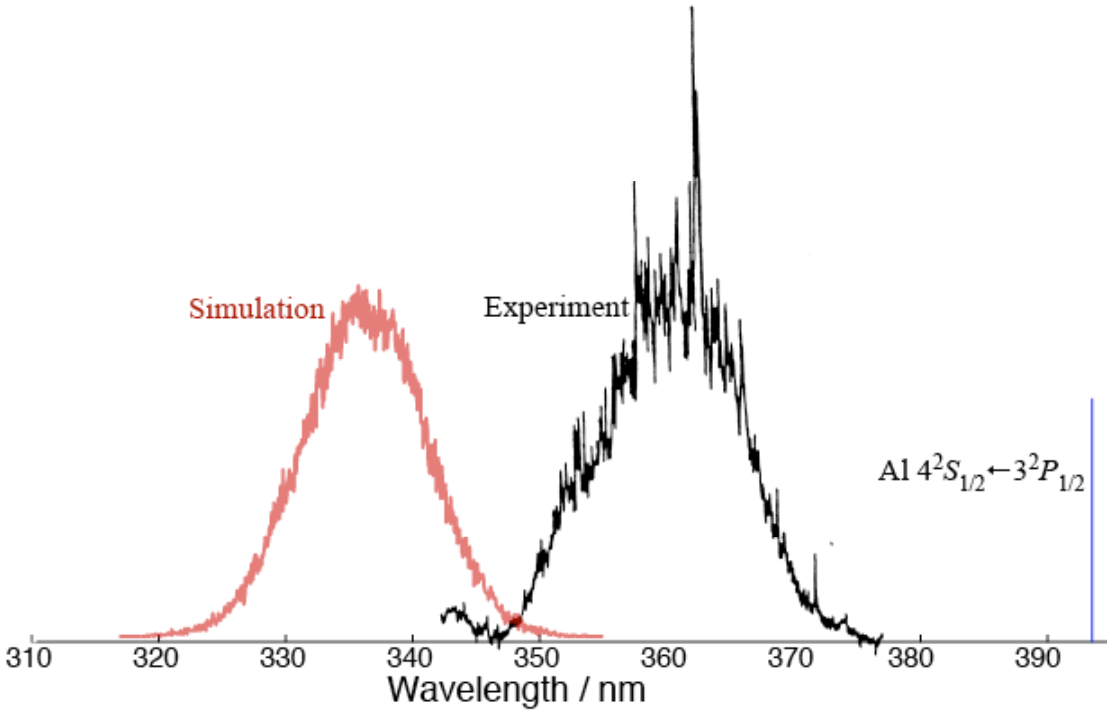

Fig 2.6 Predicted spectra for the Al $4^2S \leftarrow 3^2P$ transition in helium, compared to the experimental spectrum reported by Hui *et al*.[51]

Fig 2.7 shows our prediction for the Al $4^2P \leftarrow 3^2P$ transition in helium, as well as the assignment of the transition to the three adiabatic electronic states arising from Al ($4p$). To our knowledge, no experiments have been done reported for this transition. We predict a large blue shift (~7000 cm^{-1}) relative to the corresponding atomic transition.

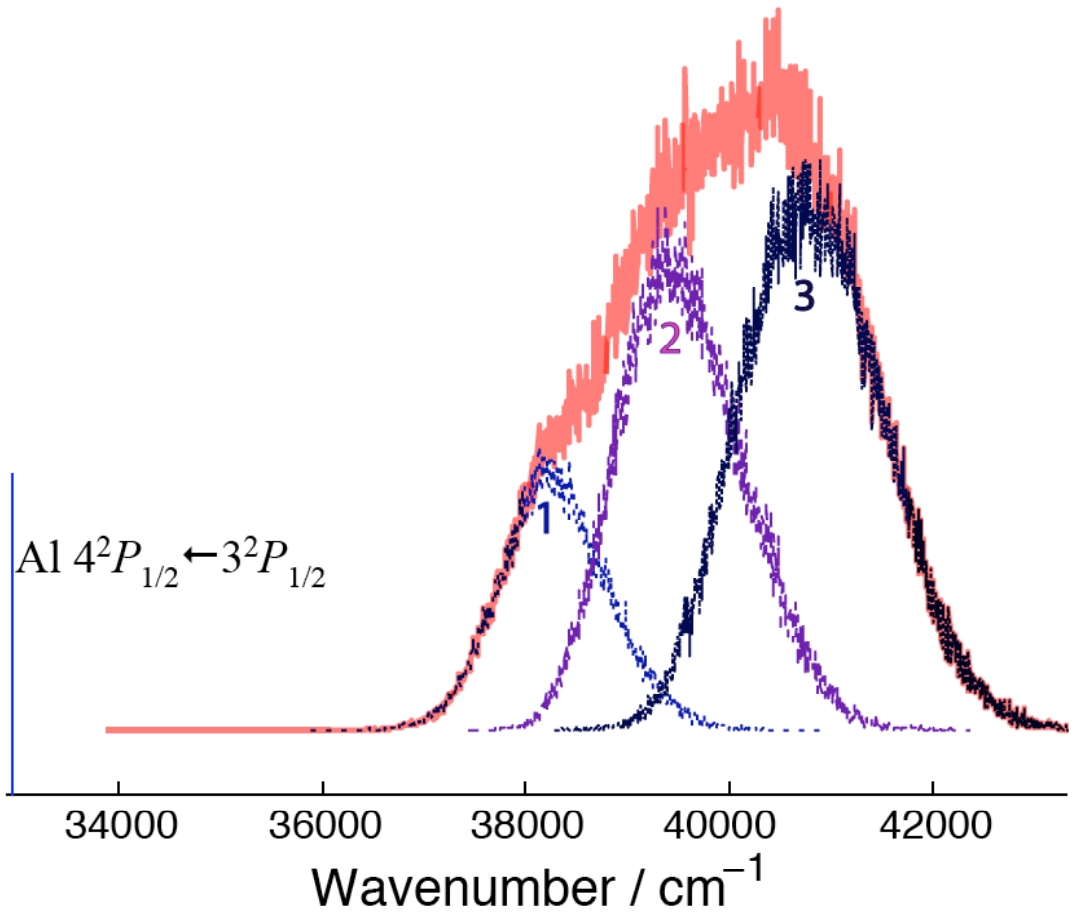

Fig 2.7 Predicted spectrum for the Al $4^2P \leftarrow 3^2P$ transition in helium. The contributions from transitions to each of the three distinct adiabatic electronic states of Al($4p$) are also shown.

2.5 Conclusion

To summarize, we have used the Multilevel path-integral Monte-Carlo simulation method to determine the arrangement of He atoms around a single Al atom

doped in a He cluster. We subsequently predict the spectrum corresponding to the $3d \leftarrow 3p$, $4s \leftarrow 3p$ and $4p \leftarrow 3p$ electronic transitions of the atom. Starting from *ab initio* Al–He pair potentials for the ground and lowest excited electronic states, we use the Balling and Wright pairwise Hamiltonian model to describe the interaction between the open-shell Al atom and an arbitrary number of He atoms. By describing this interaction as a sum of pairwise 6×6 Hamiltonian matrices, rather than the sum of pairwise scalar potentials, we can treat accurately the electronic anisotropy of the Al atom. A similar approach is used to describe the interaction of Al in its excited $3d$ and $4p$ states with multiple He atoms.

To carry out an accurate path-integral simulation in a reasonable time, we used a multilevel Monte-Carlo scheme. This involves first performing a large coarse displacement of the system in configuration space, but then refining only if the initial displacement is accepted. As we have shown, this technique is formally equivalent to a much more computationally intensive series of small displacements.

Our calculations show that insertion of Al into the cluster significantly influences the He packing. He atoms are pushed away from the embedded atom, relative to the He–He spacing in the pure liquid. This effect extends beyond the first solvation shell. The addition of an Al atom decreases the potential energy of the system by creating a helium cavity inside the liquid.

Using the results of our PIMC simulation, we then carried out a Franck-Condon simulation of the spectrum association with the $3d \leftarrow 3p$ electronic excitation of the solvated Al. With inclusion of an appropriate tail correction, the calculated spectrum agrees well with experiment, in shape, width and position. The blue shift of the calculated spectrum associated with the $4s \leftarrow 3p$ transition of solvated Al is about 25 nm (2000 cm^{-1}) more than seen in experiments on Al embedded into bulk liquid He. This discrepancy may come from the different conditions under which

experiment and simulation are performed. We predict that the spectrum associated with the $4p \leftarrow 3p$ transition will be blue shifted by ~7000 cm^{-1} (nearly 1 eV).

Chapter 3: An *ab initio* based model for the simulation of multiple ^2P atoms embedded in a cluster of spherical ligands, with application to Al in solid *para*-hydrogen

We present here a novel approach to the determination of the interaction between two atoms, each in a ^2P electronic state, embedded in a cluster of spherical atoms. This chapter is reproduced from a previously published paper by Wang, Alexander and Krumrine [Q. Wang, M. H. Alexander, and J. Krumrine, J. Chem. Phys. **117**, 5311 (2002)].

3.1 Introduction

The embedding of atomic impurities in solid hydrogen has received considerable recent experimental attention,[2,9,68,69] because of the potential technological utility of cryo-propellants. Atoms such as Li, Na, B, Al, N, and O have been successfully trapped in solid hydrogen.[9] As a complement to experimental work, simulation studies allow insight into the efficiency of impurity trapping and the degree to which these impurities will modify the solid.[15,16,70-73] Crucial to the success of these simulations is the accuracy of the description of the interaction between the embedded atom and the host. The accurate description of the atom-host interaction is complicated by the open-shell nature of most atomic radicals. Several recent studies reveal that neglect of this electronic anisotropy can lead to major inaccuracies in the calculated binding energy and in the radial distribution function of the impurity, especially when vacancies are present in the solid host.[15,16]

The interaction of Al or B with multiple $p\mathrm{H}_2$ clusters or the solid have been based on the accurate description of the binary B(Al)–H_2 cluster. A recent paper[74] has shown that sophisticated *ab initio* calculations of this binary interaction, coupled

with a description of the nuclear motion in the cluster which includes accurately the electronic orbital and spin angular momenta of the atom, can provide a description of the lower bound vibration-rotation levels of the Al–oH$_2$ complex which agrees, to within experimental uncertainty, with optical spectroscopic experiments. Simulations of clusters involving more than one H_2 molecule,[13] as well as simulations of a B or Al atom in solid pH$_2$,[15,16] have incorporated these accurate binary interactions within a model, developed first by Balling and Wright,[14] which allows the interaction potential for the solid to be obtained by diagonalizing a sum of 6×6 matrices.[17]

From the viewpoint of embedding either B or Al in solid pH$_2$ it is crucial to consider how recombination of these atoms will be mediated by the solvent molecules. The ease of this recombination will set an upper limit to the capacity of the cryosolid to store embedded atoms. Early work in this direction by Voth and Jang[71] neglected the electronic anisotropy of both the B–H_2 and B–B interaction. As we shall show in the present article, it is straightforward to go beyond this approximation by extending the ideas inherent in the approach of Balling and Wright[14] to develop an accurate description of the interaction of two ^2P atoms in the presence of multiple spherical ligands.

In the next section we shall describe new *ab initio* calculations which were done to determine the long-range behavior of the 18 states of Al_2 (9 singlet and 9 triplet states) which correlate with both atoms separately in their ground ^2P electronic state. The spin multiplicity of the triplet states then implies a total of 36 distinct states. To describe, simultaneously, the interaction of the two ^2P atoms with each other and with the spherical ligands, it is most convenient to work in a diabatic representation, which correlates with an asymptotically correct description in which the orientation of the singly-occupied p orbital on each atom is well defined with respect to a body-frame axis. In Sec. 3.3 we show how a simple valence-bond-based model, related to the atoms-in-molecules (AIM) ideas of Moffitt,[75] can be developed

to describe relations between this approximately diabatic basis and the molecular orbital description of the Al_2 molecular states.

Section 3.4 then describes how the interaction with each spherical ligand can be added on to this description of the atom-atom interaction. Our entire approach is closely related to the recent work of Batista and Coker[76] on the simulation of I_2 molecules embedded in liquid xenon, in which they used a diatomics-in-molecules (DIM) based approach to model the interaction potential. In Sec. 3.5 we report our development of an efficient computer code to calculate the resulting interaction potential and its derivatives, for future use in simulation studies. Section 3.6 presents a demonstration calculation, which shows how the interaction between two Al atoms site-substituted in solid pH$_2$ is significantly altered by the pH$_2$ molecules that separate the two metal atoms. We close with a brief conclusion.

3.2 Ab initio calculations

The encounter of two atoms both in ^2P electronic states gives rise to six triplet states: $^3\Pi_g$, $^3\Pi_u$, $^3\Delta_u$, $^3\Sigma_g^-$, and two states of $^3\Sigma_u^+$ symmetry which we label $1^3\Sigma_u^+$ and $2^3\Sigma_u^+$; as well as six singlet states: $^1\Pi_g$, $^1\Pi_u$, $^1\Delta_g$, $^1\Sigma_u^-$, and two states of $^1\Sigma_g^+$ symmetry, which we label $1^1\Sigma_g^+$ and $2^1\Sigma_g^+$. Because of the spin degeneracy of the triplet states and the spatial degeneracy of the Π and Δ states of both multiplicities, there are in fact 36 distinct electronic states. To determine the potential curves for the corresponding states of the Al_2 dimer as a function of the atom-atom distance R, we carried out state-averaged multi-configuration, self-consistent field calculations, SA-MCSCF (the state averaging was applied separately to all states of a given multiplicity).[77] Subsequently, we performed internally-contracted, multi-reference, configuration-interaction (ICMRCI) calculations[78,79] of the interaction potentials. The augmented correlation-consistent valence quintuple zeta (*av5z)* basis sets of Dunning and co-workers were used.[80-82] Only the outer p orbitals on each atom were

included in the active space, so that the 1*s*, 2*s*, 2*p*, and 3*s* orbitals on the Al atom were kept doubly occupied.

At each value of *R* the two pairs of states of the same symmetry ($^3\Sigma_u^+$ for the triplets and $^1\Sigma_g^+$ for the singlets) were transformed so as to maximize the overlap between the orbitals of each pair, and the asymptotic orbitals of each pair of states, computed at R = 30 bohr. This diabatizing transformation was then applied to the ICMRCI energies for these pairs of states, at the same value of *R*. In this way the sum of the orbital and overlap contribution to the mixing of the two states of the same symmetry is minimized, so that all the mixing manifests itself in the CI coefficients.

Figure 3.1 displays the dependence at long range of the six diabatic potentials of both singlet and triplet multiplicity for Al_2. As can be seen, at long range the $^3\Pi_u$ curve is the most attractive. The latest spectroscopic investigations indicate that this likely remains the lowest state at the molecular minimum, even though the $^3\Sigma_g^+$ state is the lowest electronic state of the bound molecule.[83] Figure 3.2 displays the dependence on *R* of the coupling between the two diabatic states of Σ_g^+ symmetry (singlets), which we designate $^1V_{12}$, and between the two diabatic states of Σ_u^+ symmetry (triplets), which we designate $^3V_{12}$. These diabatic couplings are large in magnitude, especially the coupling between the two singlet states.

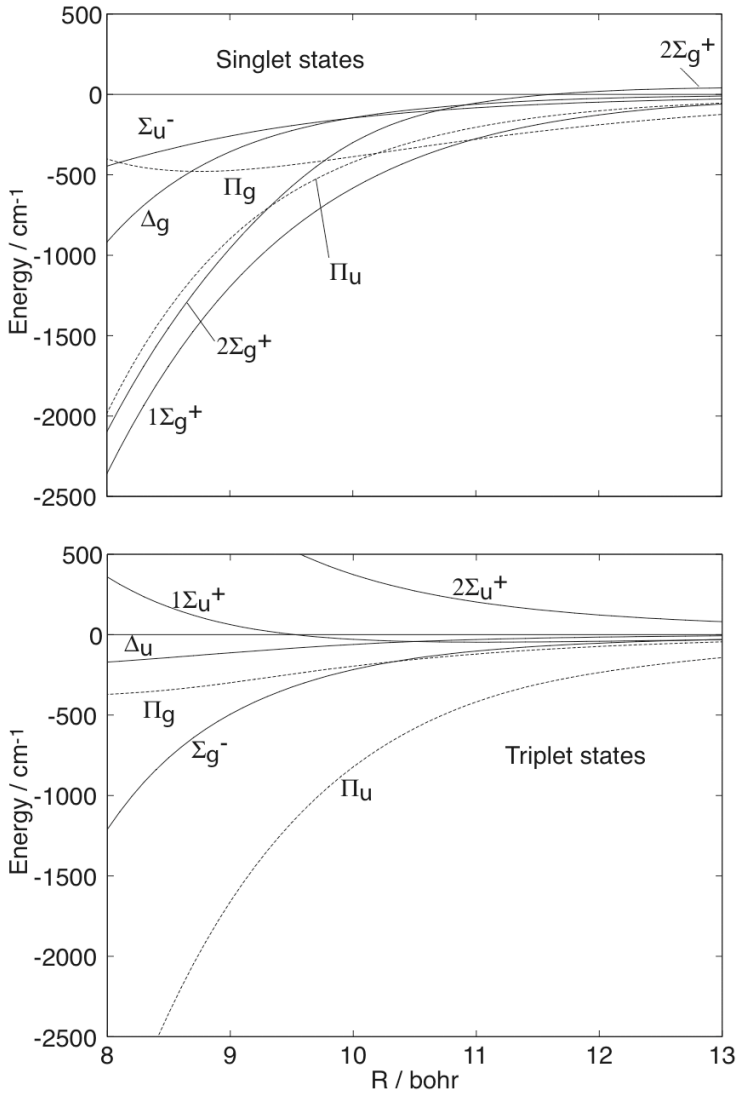

Fig 3.1 Potential curves for all the singlet (upper panel) and triplet (lower panel) electronic states of Al_2 which correlate with the separated atoms both in their ground electronic state. The two triplet states of Σ_u^+ symmetry and the two singlet states of Σ_g^+ symmetry have been diabatized, as described in Sec. 2.2 of the text. For clarity, dashed lines are used to designate the states of Π symmetry.

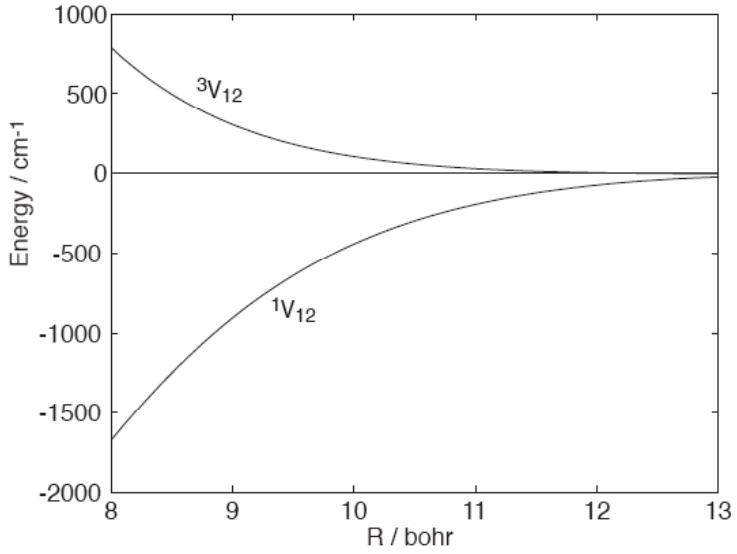

Fig 3.2 Diabatic coupling potentials: ${}^1V_{12}$ between the two singlet states of Σ_g symmetry and ${}^3V_{12}$ between the two triplet states of Σ_u symmetry.

3.3 Valence bond description of the ${}^2P$–${}^2P$ diabatic states

To describe the interaction of two ${}^2P$ atoms embedded in a cluster formed of spherical ligands (as, for example, Al atoms embedded in $p\mathrm{H}_2$), we would like to use the *ab initio* based interaction potentials presented in Sec. 3.2 combined with a model, similar to that presented by Balling and Wright,[14] for the interaction of each of the two metal atoms with the spherical ligands. This model is based on explicit consideration of the interaction of the p_x, p_y, and p_z orbitals with each ligand. The ${}^2P$ atom will be described in an uncoupled, Cartesian basis $| l\ q_l >$ where l, the orbital electronic angular momentum of the atom is 1 and $q_l = x,\ y,$ or z designates the orientation of the real (Cartesian) singly-filled p orbital. The encounter between an atom in a ${}^2P$ state and a spherical atom (or $p\mathrm{H}_2$) at any position in space can be described as a rotation of a diagonal matrix which contains the two potentials, V_Σ and V_Π, which describe the interaction of the ${}^2P$ atom and the spherical partner when the latter is located on the z axis.[14,17]

As mentioned in the Introduction, this approach is closely related to the earlier work of Batista and Coker[76] in which they modeled the interaction of two I atoms embedded in liquid xenon. These authors used a diatomics-in-molecules (DIM) approach.[84] Applications to molecular dynamics of the DIM and closely-related orthogonalized Moffitt method go back over thirty years.[85-87]

It would be straightforward to describe similarly the interaction between each spherical ligand and both ^2P atoms if we knew the Cartesian orientation of the two p orbitals. Unfortunately, these are coupled together in any molecular orbital description. Thus, prior to determining the ligand-metal interaction, it is necessary to transform the 36 diabatic states, which are described by definite values of the projection Λ of the total electronic angular momentum and the projection Σ of the total electronic spin, into an uncoupled basis consisting of the product of the Cartesian spin-orbital on Al atom a (the Cartesian orbital multiplied by its spin, α or β) and the Cartesian spin-orbital on Al atom b. We shall denote this the $q_a q_b$ basis, which is a product basis of what Moffit would describe as "approximate atomic functions".[75] The Al–Al axis is assumed to define the z-axis.

In the MCSCF calculations described in the preceding section only the two Al $3p$ orbitals make up the active space. It is straightforward, by analysis of the coefficients of the MCSCF wavefunctions, to extract the contribution of each covalent (valence bond) $q_a q_b$ orbital occupancy to the MCSCF state wavefunctions. At long range, because the MCSCF wavefunctions dissociate properly, all ionic ($q_a q_a'$) contributions to the wavefunctions vanish. The diabatization of the two $^3\Sigma_u$ states and the two $^1\Sigma_g$ states ensures that the asymptotic description of these two states in terms of $q_a q_b$ states [see Eq. (3.3) below] remains valid at all values of R.

The transformation between the valence-bond-like $q_a q_b$ basis (columns) into the 9 triplet molecular orbital diabatic states with $M_S = 1$ (rows) is given by

	$x_a y_b$	$x_b y_a$
$^3\Sigma_g^-$	$2^{-1/2}$	$2^{-1/2}$
$^3\Delta_{u,xy}$	$2^{-1/2}$	$-2^{-1/2}$

(3.1)

	$x_a z_b$	$x_b z_a$
$^3\Pi_{gx}$	$2^{-1/2}$	$2^{-1/2}$
$^3\Pi_{ux}$	$2^{-1/2}$	$-2^{-1/2}$

(3.2)

(with a similar expression for the Π_{gy} and Π_{uy} states in terms of $y_a z_b$ and $y_b z_a$), and

	$x_a x_b$	$y_a y_b$	$z_a z_b$
$\Delta_{u,x2\text{-}y2}$	$2^{-1/2}$	$-2^{-1/2}$	0
$1\ \Sigma_u^+$	$6^{-1/2}$	$6^{-1/2}$	$(2/3)^{1/2}$
$2\ \Sigma_u^+$	$3^{-1/2}$	$3^{-1/2}$	$-3^{-1/2}$

(3.3)

We obtain an entirely similar expression for the triplet states with $M_S = -1$, except that each of the Cartesian spin-orbitals has spin state β.

For the states, both singlet and triplet, with M_S=0, the comparable transformations from $q_a q_b$ states into definite Λ and definite $\Sigma(M_S)$ states is given by the following matrices:

	$x_a\bar{x}_b$	$\bar{x}_a x_b$	$y_a\bar{y}_b$	$\bar{y}_a y_b$	$z_a\bar{z}_b$	$\bar{z}_a z_b$
$^1\Delta_{g,x2\text{-}y2}$	1/2	–1/2	1/2	–1/2	0	0
$1\ ^1\Sigma_g^+$	$12^{-1/2}$	$-12^{-1/2}$	$12^{-1/2}$	$-12^{-1/2}$	$3^{-1/2}$	$3^{-1/2}$
$2\ ^1\Sigma_g^+$	$6^{-1/2}$	$-6^{-1/2}$	$6^{-1/2}$	$-6^{-1/2}$	$-6^{-1/2}$	$6^{-1/2}$
$^3\Delta_{u,x2\text{-}y2}$	1/2	1/2	–1/2	–1/2	0	0
$1\ ^3\Sigma_u^+$	$12^{-1/2}$	$12^{-1/2}$	$12^{-1/2}$	$12^{-1/2}$	$3^{-1/2}$	$3^{-1/2}$
$2\ ^3\Sigma_u^+$	$6^{-1/2}$	$6^{-1/2}$	$6^{-1/2}$	$6^{-1/2}$	$-6^{-1/2}$	$-6^{-1/2}$

(3.4)

	$x_a\bar{y}_b$	$\bar{x}_a y_b$	$x_b\bar{y}_a$	$\bar{x}_b y_a$
$^1\Sigma_u^-$	1/2	–1/2	–1/2	1/2
$^1\Delta_{g,xy}$	1/2	–1/2	1/2	–1/2
$^3\Sigma_g^-$	1/2	1/2	1/2	1/2
$^3\Delta_{u,xy}$	–1/2	–1/2	1/2	1/2

(3.5)

and

	$x_a\bar{z}_b$	$\bar{x}_a z_b$	$x_b\bar{z}_a$	$\bar{x}_b z_a$
$^1\Pi_{gx}$	1/2	–1/2	1/2	–1/2
$^1\Pi_{ux}$	1/2	–1/2	–1/2	1/2
$^3\Pi_{gx}$	1/2	1/2	1/2	1/2
$^3\Pi_{ux}$	1/2	1/2	–1/2	–1/2

(3.6)

with a similar matrix relating the Π states of *y* symmetry to the Cartesian spin-orbit labeled states $y_a\bar{z}_b$, $\bar{y}_a z_b$, $y_b\bar{z}_a$, and $\bar{y}_b z_a$.

Strictly speaking, the $q_a q_b$ states are not true valence bond states because the overlap does not enter into the transformation between these and the molecular orbital states. However, the nearest-neighbor distance in solid H_2 is ~7.2 bohr. We will be interested primarily (see Sec. 3.5 below) in the simulation of two Al atoms separated by at least 10 bohr, where overlap factors will be small. This neglect of the overlap terms is equivalent to what has been called the ZAOA (zero atomic overlap approximation) in the DIM literature.[86,88,89]

In the molecular orbital basis, the matrix of the electronic Hamiltonian H_{el}, exclusive of spin-orbit coupling, is diagonal, except for the two diabatic states of Σ_u symmetry (for the triplets) and the two diabatic states of Σ_g symmetry (for the singlets). The transformation [defined by Eqs. (3.1)–(3.6)] into the $q_a q_b$ basis gives rise to numerous off-diagonal components, although the matrix of H_{el} is still diagonal in the total spin-projection quantum number, and the matrix is divided into blocks by the reflection symmetry of the $q_a q_b$ states. The matrix elements of H_{el} in the $q_a q_b$ basis can be expressed in terms of the diagonal matrix elements of H_{el} in the diabatic molecular orbital basis plus the two off-diagonal coupling terms $^1V_{12}$ and $^3V_{12}$. The explicit form of these matrix elements is given in Appendix 3.I.

The transformation described by Eqs. (3.1)–(3.6) pertains to the MCSCF wavefunction, and is an orthogonal transformation, valid at all *R*. As *R* decreases,

ionic terms will make a contribution to the MCSCF wavefunction. In addition, double (and higher order) excitations will make a contribution to the IC-MRCI wavefunction at all values of R. Consequently, the diabatic states, obtained by the transformation described by Eqs. (3.1)–(3.6), and the corresponding diabatic energies (Appendix 3.I), are characterized by a single valence-bond-like $q_a q_b$ electron occupancy only asymptotically. However, since the CI corrections to the wavefunction are small, and since the ionic terms vanish asymptotically, to an excellent degree of approximation the valence-bond $q_a q_b$ labels provide an excellent description of the behavior of the two p electrons in each state.

We write the spin-orbit Hamiltonian as the sum of the usual atomic spin-orbit Hamiltonian on each ^2P atom, taken separately,

$$H_{\rm so}(a,b) = H_{\rm so}(a) + H_{\rm so}(b) \tag{3.7}$$

The distances are large enough that we can safely neglect any spin-other orbit terms coupling the two atoms. In the 6×6 basis of the three Cartesian p orbitals (and their two spin projections), the matrix of the spin-orbit Hamiltonian is

$$\underline{\underline{H}}_{so} = \frac{1}{2} a \times \begin{array}{c|cccccc} & x & y & z & \bar{x} & \bar{y} & \bar{z} \\ \hline x & 0 & i & 0 & 0 & 0 & 1 \\ y & -i & 0 & 0 & 0 & 0 & i \\ z & 0 & 0 & 0 & -1 & -i & 0 \\ \bar{x} & 0 & 0 & -1 & 0 & -i & 0 \\ \bar{y} & 0 & 0 & i & i & 0 & 0 \\ \bar{z} & 1 & -i & 0 & 0 & 0 & 0 \end{array} \tag{3.8}$$

where a is the spin-orbit constant of the ^2P atom (74.7 cm^{-1} for Al[18]). Consequently, the matrix elements of the spin-orbit Hamiltonian in the basis of the 36 $q_a q_b$ valence-bond states are given by

$$\langle q_a' q_b' | H_{so} | q_a q_b \rangle = \delta_{q_a' q_a} \langle q_b' | H_{so} | q_b \rangle + \delta_{q_b' q_b} \langle q_a' | H_{so} | q_a \rangle \quad (3.9)$$

where $\langle q_b' | H_{so} | q_b \rangle$ and $\langle q_a' | H_{so} | q_a \rangle$ correspond to matrix elements of the one-atom spin-orbit matrix are given by Eq. (3.8).

Adding the 36 ×36 matrix of the spin-orbit Hamiltonian to the full 36 ×36 matrix of the Al_2 dimer, and diagonalizing the resulting Hamiltonian, we obtain fully adiabatic electronic states in the presence of the spin-orbit coupling. Figure 3.3 shows the dependence on *R* of the potential curves of these fully adiabatic states at long range. The most attractive of these corresponds to the $^3\Pi_{\Omega=0}$ state. This strongly attractive potential would govern the interaction between two Al atoms embedded in a cluster of spherical atoms, provided that the spherical ligands did not interfere with the coupling between the electronic and spin orbital angular momenta. As we will see below, in solid pH$_2$ the ligand–Al interaction does significantly effect the strength and range of the attractive interaction between the two Al atoms.

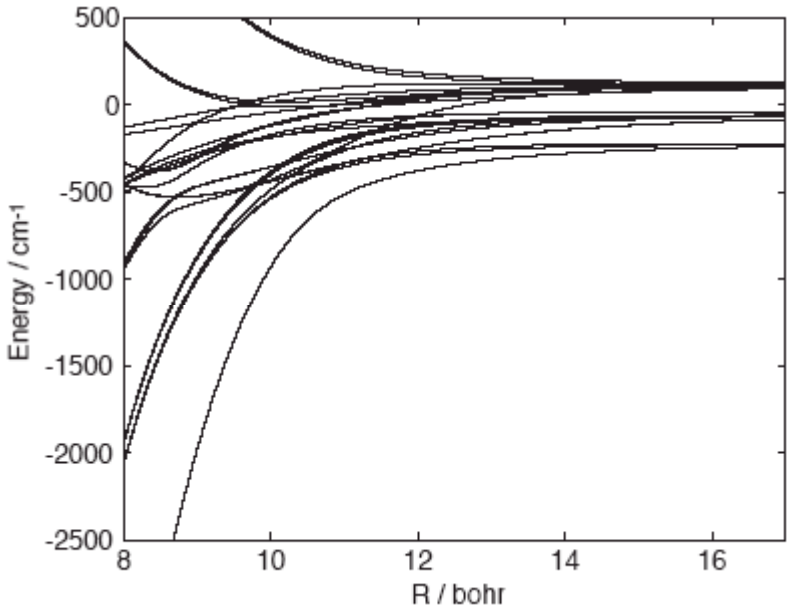

Fig 3.3 Fully-adiabatic Al_2 potential curves obtained by diagonalizing the sum of the 36 × 36 matrix of the electronic plus spin-orbit Hamiltonian.

3.4 Interaction of the two ^2P atoms with multiple spherical ligands

Balling and Wright[14] developed a model to describe the interaction of multiple spherical atoms with a single atom in a ^2P electronic state. The coordinate system is defined by the orientation of the three p Cartesian orbitals on the ^2P atom. As discussed in the preceding section, if the spherical ligand were located along the z-axis, the interaction could be described in terms of two potentials, V_Σ and V_Π.[90] If the spherical atom is rotated to a position $\{R, \theta, \phi\}$, the interaction, still in the basis of the three Cartesian p orbitals, is described by the matrix

$$\mathbf{V}(R, \theta, \phi) \equiv \mathbf{D}(\phi, \theta, 0)\, \mathbf{V}(R)\, \mathbf{D}^T(\phi, \theta, 0) \tag{3.10}$$

Here $\mathbf{D}(\phi, \theta, 0)$ is the matrix of the rotation specified by the Euler angles $\{\phi, \theta, 0\}$,[59] and $\mathbf{V}(R)$ is a diagonal matrix with elements

q_l	$q_l = x$	y	z
x	$V_\Pi(R)$	0	0
y	0	$V_\Pi(R)$	0
z	0	0	$V_\Sigma(R)$

(3.11)

It can be shown that the transformation of Eq. (3.10) leads to the following expression for $\mathbf{V}(R,\theta,\phi)$, still in the basis of the x, y and z Cartesian p orbitals.

$$\mathbf{V} = V_\Pi\, \mathbf{1} + (V_\Sigma - V_\Pi) \times \frac{1}{R^2} \begin{vmatrix} x^2 & xy & xz \\ xy & y^2 & yz \\ xz & yz & z^2 \end{vmatrix} \tag{3.12}$$

where $\mathbf{1}$ designates the unit matrix and $\{x,y,z\}$ designates the Cartesian position of the spherical ligand. Here we have suppressed the arguments of $\mathbf{V}$ and the dependence on R of V_Σ and V_Π. In the basis of the Cartesian orbitals with negative spin projection

quantum number ($\bar{x},\bar{y},\bar{z}$) we have an identical 3×3 matrix, so that in the basis of the six *p* spin-orbitals, the interaction of the Al atom with a spherical perturber at position $\{x,y,z\}$ is block diagonal and given by

$$\mathrm{V}_6(x,y,z)=\begin{vmatrix} \mathrm{V} & 0 \\ 0 & \mathrm{V} \end{vmatrix} \tag{3.13}$$

where **V** is defined by Eq. (3.12).

In the presence of multiple spherical ligands, each located at position $\{x_i,y_i,z_i\}$, the matrix of the complete interaction potential is just

$$\mathrm{V}=\sum_i \mathrm{V}_6(x_i,y_i,z_i) \tag{3.14}$$

In the adiabatic limit, we diagonalize the sum of the 6×6 **V** matrix and the 6×6 matrix of the spin-orbit operator on the single ^2P atom [Eq. (3.8)]. The motion of the atoms is governed by the lowest root V_a, to which is added the pair-wise scalar interaction between all the spherical ligands.

This simple, yet effective, model can easily be extended to the interaction of two ^2P atoms embedded in an environment of multiple spherical ligands. The interaction between the two Al atoms is described by the block-diagonal 36×36 matrix defined in Appendix 3.I to which is added the 36×36 matrix of the combined spin-orbit Hamiltonian [see Eqs. (3.8) and (3.9)]. The transformation to the valence bond q_aq_b states, defines, for each state, the Cartesian orientation of each of the *p* orbitals. Consequently, the interaction with each spherical ligand can be described by a separate 36×36 matrix $\mathbf{V}_i(x_i,y_i,z_i)$ with matrix elements

$$\langle q_a'q_b'|V_i\,|\,q_aq_b\rangle=\delta_{q_a'q_a}\left(\mathrm{V}_6\right)_{q_b'q_b}+\delta_{q_b'q_b}\left(\mathrm{V}_6\right)_{q_a'q_a} \tag{3.15}$$

where the matrix elements of $\mathbf{V}_6$ in the Cartesian states of either atom *a* or atom *b* are given by Eqs. (3.12) and (3.13).

In the adiabatic limit, the interaction matrix $\mathbf{V}_i$ is summed over the positions of each ligand, to which is added the 36×36 matrices of the spin-orbit operator [Eq. (3.9)] and the Al–Al interaction (discussed in the preceding paragraph). The resulting matrix is diagonalized. To the lowest root is added the scalar pair-wise interaction potential between all the spherical ligands. This then defines the potential for the motion of any atom in the ensemble.

In the case of a single ^2P atom the orientation of the p orbitals refers to the (arbitrary) space-fixed axis system. For the present situation of two ^2P atoms, the orientation of the p orbitals in the $q_a q_b$ basis is defined with respect to a body-frame system where the vector joining the two ^2P atoms defines the z axis. Accordingly, the coordinates $\{x_i,y_i,z_i\}$ which define the position of each ligand must be referenced to this same body frame. This is discussed in more detail in Appendix 3.II.

3.5 Computational implementation

In order to pursue eventually simulation studies, we have developed a fast FORTRAN subroutine to calculate the potential for two Al atoms embedded in N pH$_2$ molecules as well as the 3N+6 derivatives necessary for the determination of the forces. The 18 Al–Al diabatic energies, plus the two off-diagonal diabatic coupling potentials were fitted with accurate functional forms containing 4–6 parameters per term. For computational expediency, we used a rapid table-lookup algorithm to calculate the Al–Al diabatic energies, the Al–H$_2$ V_Σ and V_Π potentials, and the H$_2$–H$_2$ potential, as well as their derivatives. In this algorithm, the potential is first calculated at a grid of points equi-spaced in r^{-2}, and then algebraically interpolated.[24]

To determine the potential for a given arrangement of the N+2 atoms requires the determination of one set of 14 Al–Al potentials (12 diagonal diabatic potentials and two off-diagonal diabatic potentials), the transformation of the resulting terms into the $q_a q_b$ basis (see Appendix 3.I), the determination of 4N Al–pH$_2$ potentials (V_Σ

and V_{Π} for each Al–pH$_2$ pair), the transformation of the resulting 2N matrices into the $q_a q_b$ basis following Eq. (15), the diagonalization of the resulting 36×36 matrix, and the determination of N(N–1)/2 H_2-H_2 potentials. In the present application we took the H_2–H_2 potential of Silvera and Goldman.[91]

In addition there are 3N+6 derivatives of the potential which must be determined in order to calculate the forces which are necessary in a molecular dynamics based simulation, such as those of Voth and co-workers.[15,16,71] The vector joining the two Al atoms ($\vec{R}$)defines the z axis in the body-frame coordinate system. The x and y axes are defined by the orientation of $\vec{R}$ in the space-frame. As is discussed in more detail in Appendix 3.II, the derivatives of the potential with respect to the position of any of the pH$_2$ ligands can be determined using the Hellman-Feynman theorem, which requires only the derivative of the $\mathbf{V}_i$ matrix of Eq. (3.15) for the particular Al–H_2 pair. For the remaining 6 coordinates (associated with the two Al atoms), the derivatives involve numerical differentiation of the lowest root of the full 36×36 potential matrix.

A series of tests showed that the total computational time scaled nearly linearly with N. This indicates that the rate determining step, despite the efficient table lookup method, is the calculation of the 4 N Al–pH$_2$ potentials, and the transformation of these contained in Eq. (3.15).

3.6 Test calculation

To investigate the role that the intervening pH$_2$ molecules play in moderating the Al–Al interaction, we carried out the following simple simulation. We assume that solid pH$_2$ crystallizes in a hexagonal close-packed lattice.[92] The structure of the hcp lattice (illustrated schematically in Fig 3.4) consists of an overlapping series of infinite hexagonal planes. We substituted two Al atoms at the center of adjacent hexagons in one plane, as illustrated in Fig 3.5. We then allowed the Al atoms to

move, symmetrically, along the line which connects the two site-substitutional positions. Within the hcp lattice each site-substituted Al atom is surrounded by 12 nearest neighbors (at a distance of 7.163 bohr, which corresponds to the zero-pressure density of solid H_2 of 23.10 cm^3/mole[92]), six next-nearest neighbors (at a distance of 10.129 bohr), and two next-next-nearest neighbors (at a distance of 11.696 bohr). To simulate the effect of embedding the two Al atoms in the pH_2 lattice, we included all pH_2 molecules which were situated within 11.7 bohr of at least one of the substitutional sites, which is a total of 36 pH_2 ligands. Figure 3.6 shows the position of these 36 ligands with respect to the two Al atoms.

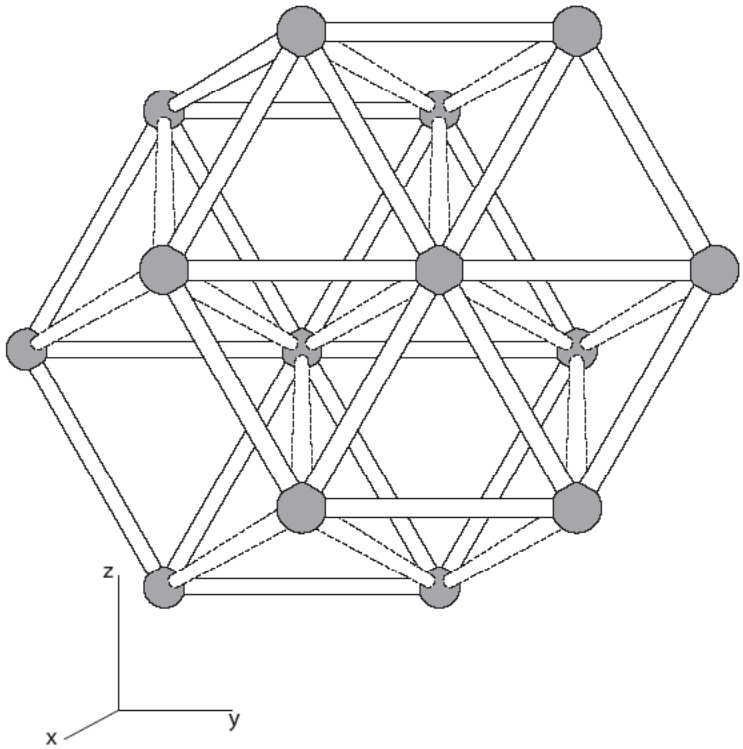

Fig 3.4 Schematic picture of an hcp lattice. The lattice consists of layers of hexagonal planes. Neighboring planes are displaced with respect to the adjacent planes. For more information, see http://cst-www.nrl.navy.mil/lattice/struk/a3.html. Each vertex has 12 nearest neighbors: 6 at the vertices of the surrounding hexagon in the same plane, and 6 arranged in equilateral triangles in the two adjacent planes. The solid and dashed connection lines do not indicate actual bonds, but are inserted merely to guide the eye and illustrate the relative position of the hexagonal planes.

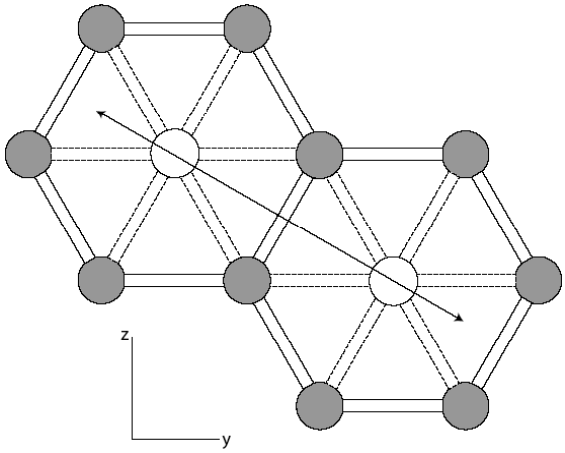

Fig 3.5 Position of site-substituted Al atoms in two adjacent hexagons in one hcp plane. In our demonstration calculation the atoms are allowed to move symmetrically back and forth along the line which connects them. The solid and dashed connection lines do not indicate actual bonds, but are inserted merely to guide the eye.

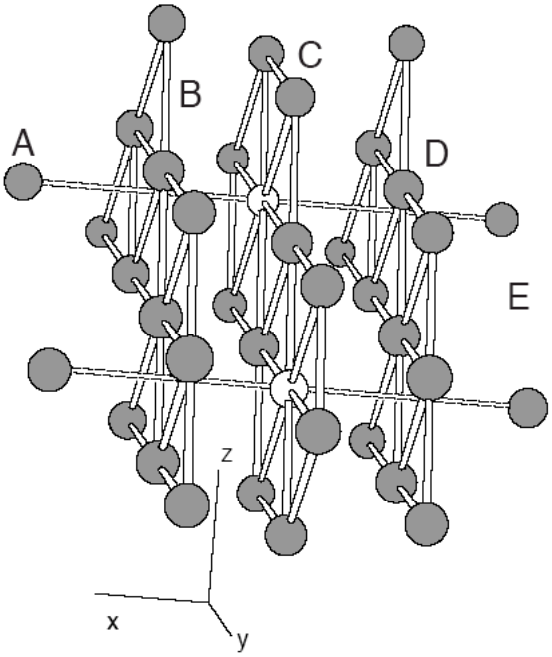

Fig 3.6 Section of the hcp lattice of pH$_2$, showing the two site-substituted Al atoms (white) surrounded by all 36 pH$_2$ molecules which lie within 11.7 bohr of one or the other of the Al atoms. For purposes of illustration, in this figure the crystal is oriented so that the hexagonal planes, labeled "A" – "E" can be distinguished. The pH$_2$ molecules in planes A and E lie directly above and below the two Al atoms, as indicated by the dashed connection lines. These connection lines do not indicate actual bonds, but are inserted merely to guide the eye.

The potential energy for motion of the Al atoms along their line of centers was determined by constructing and diagonalizing the full 36×36 matrix, discussed in the preceding sections. Figure 3.7 shows the dependence on the Al–Al distance of the energy of the lowest root, which provides, in the adiabatic model, the potential for the relative motion of the Al atoms.

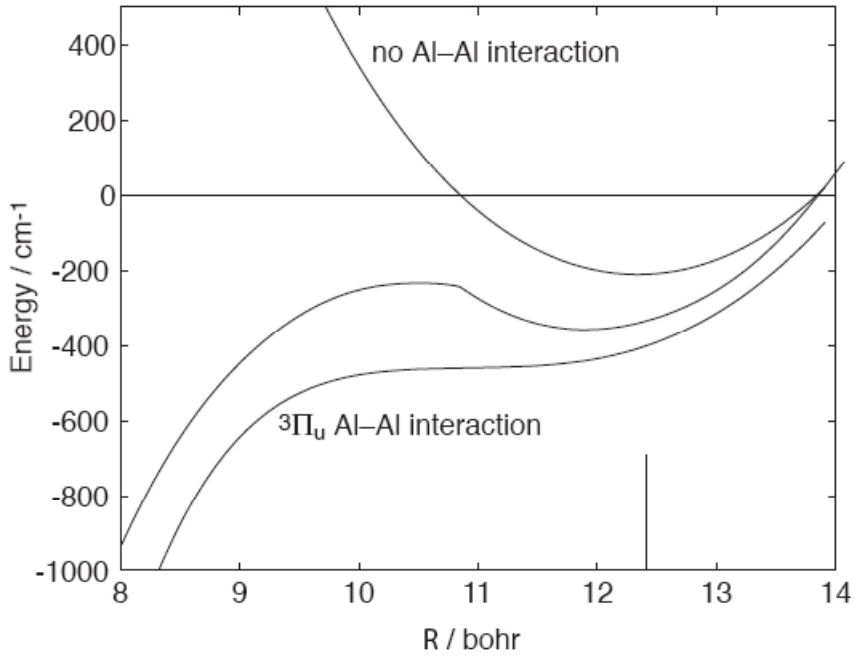

Fig 3.7 Potential of interaction between two Al atoms, site substituted in two adjacent hexagons of an hcp lattice of pH$_2$, constrained to move symmetrically along the line of separation (see Fig 3.5). The upper, parabolic curve corresponds to a calculation in which all Al– pH$_2$ interactions are included, but the Al–Al interaction potential is set to zero. The lower, barrierless curve, corresponds to a calculation in which all Al–pH$_2$ interactions are included and the Al–Al interaction is assumed to be given by the most attractive ($^3\Pi_u$) of the Al–Al interaction potentials (see Figs 3.1 and 3.3). Finally, the middle curve depicts the lowest eigenvalue of the 36 × 36 matrix of the full interaction potential as developed in the present paper.

For comparison, we also present in Fig 3.7, the potentials which arise from a calculation in which we include the interactions between both Al atoms and the 36

pH$_2$ ligands, without including any interaction between the two Al atoms. This potential then corresponds to the lowest eigenvalue of the sum of the Balling and Wright 6 ×6 matrices for the interaction of the two Al atoms with all the hydrogens. The resulting potential is centered at a distance of 12.34 bohr, which is nearly equal to the distance between the two substitutional sites (12.41 bohr, see Fig 3.5).

If we were to include just the pH$_2$ ligands which lay a certain distance from one of the Al atoms, then, because of the symmetry of this distribution around the substitutional site, the most favorable position of the Al atom would be at this substitutional site. However, because all pH$_2$ ligands are included which lie within a given distance from either pH$_2$, the distribution of these is not symmetrically placed with respect to the position of either Al atom. Consequently, the pH$_2$ ligands which are centered around the one Al atom act to attract, slightly, the other Al atom, so that equilibrium separation between the two Al atoms is slightly less than the distance between the substitutional sites.

In the second comparison contained in Fig 3.7, we assume that the 6 ×6 Balling and Wright model described the interaction of each Al atom with all the hydrogens, as described in the preceding paragaraph, and that the most attractive of the Al$_2$ potentials ($^3\Pi_u,\Omega=0$, see Figs 3.1 and 3.3) describes the interaction between the two Al atoms. In other words we assume that the presence of the pH$_2$ molecules does not interfere with the spin and orbital angular momentum coupling of the two 3p electrons on the separate Al atoms, so that they can couple as favorably as possible. In this case, we observe that the strong attractive limb of the $^3\Pi_u$ state can overcome the relatively weak Al–pH$_2$ interactions, which, as we have seen in the preceding paragraph, tend to hold the Al atoms at their substitutional sites. Consequently, when the $^3\Pi_u$ potential is added, there is no apparent barrier to recombination of the two Al atoms.

However, as can be seen in Fig 3.7, when the electronic anisotropies of the Al–Al and Al–pH$_2$ interactions are taken into account simultaneously, then there appears a substantial barrier to recombination of the Al atoms. The $^3\Pi_u$ state corresponds to a $\sigma_a\pi_b - \sigma_b\pi_a$ orientation of the two 3p electrons. However, the interaction of the σ orbital with the intervening two hydrogen molecules is strongly repulsive, which tends to overcome the attractiveness of the $^3\Pi_u$ state, at least at long range. As the two Al atoms approach closer (inside of ~10 bohr), the depth of the $^3\Pi_u$ attraction becomes progressively larger and eventually dominates, which would lead to eventual recombination. The slight kink in the middle curve in Fig 3.7 corresponds to an avoided crossing. Examination of the eigenvectors show that at long range the lowest adiabatic state has, as we would expect, predominately $^3\Pi$ character. At shorter distances, where the σ interaction becomes unfavorable, the lowest adiabatic state shifts to predominately $^1\Sigma_g^+$ character which corresponds to a more favorable $\pi_x\pi_x + \pi_y\pi_y$ orientation of the 3p electrons.

3.7 Conclusion

We have presented a novel approach to the determination of the interaction between two atoms, each in a ^2P electronic state, embedded in a cluster of spherical atoms. The model is based on the prior determination of accurate *ab initio* potential energy curves for the M$_2$ system, for all the 36 electronic states which correlate with dissociation into ground-state M(^2P) atoms, and the subsequent transformation of the two $^1\Sigma_g^+$ and two $^3\Sigma_u^+$ states into a diabatic basis in which the electronic character remains as similar as possible to the separated atom limit. Consequently, making use of a valence-bond-like (or atoms-in-molecules) model, we transform the 36 molecular orbital states, which have a definite multiplicity and D$_{\infty h}$ spatial symmetry, into a set of 36 Cartesian (q_aq_b) states which correspond to assigning the two p electrons to approximate Cartesian orbitals centered on either atom.

It is then easy to use the earlier Balling and Wright model[14] to determine, in this 36 state basis, the matrix elements corresponding to the interaction of each ^2P atom with any number of surrounding spherical ligands. The lowest eigenvalue of the resulting 36×36 matrix defines, in an adiabatic approximation, the potential governing the motion of the atoms. Our construction of the interaction potential is closely related to recent work of Batista and Coker on the interaction of two I atoms in liquid xenon.[76]

We presented an application to the determination of the interaction of two Al atoms embedded in solid $p\mathrm{H}_2$, site-substituted in the center of two adjacent hexagons. High accuracy, multi-reference, configuration-interaction calculations were used to determine the necessary Al_2 potential energy curves. The results of this model calculation show that the interaction between the two Al atoms is significantly modified by the presence of the intervening $p\mathrm{H}_2$ models. When the Al atoms are separated by distances greater than 10 bohr, the interaction with the $p\mathrm{H}_2$ molecules impede the two $3p$ electrons from aligning themselves correctly for the lowest electronic state of Al_2. Consequently, there appears a significant barrier (at long range) to recombination of the two Al atoms. This barrier is not present if the competing electronic anisotropy of the interactions is not taken into account.

This model could be adapted without modification to the interaction of other ^2P atoms in either $p\mathrm{H}_2$ or other spherical environments (Ar, He). Full many-body simulation studies, along the lines of those we have carried out for a single B or Al atom in $p\mathrm{H}_2$,[15,16] can now be done to explore to full details of the recombination of embedded atoms. In addition, the model presented here could be extended, in a straightforward manner, to the interaction of atoms in other open-shell electronic states, or, to the interaction of two atoms in different electronic states.

Chapter 4: Path-integral Monte-Carlo simulations of solid *para*-hydrogen doped with several Al impurities

4.1 Introduction

The embedding of light impurities in solid hydrogen has received considerable experimental and theoretical attention in recent years, partly because of the potential technological applications as high energy density materials.[10] Fajardo and coworkers have successfully trapped light impurities such as Li, B, Al, N, O in solid hydrogen.[2,9,93] Spectral studies have also been performed by them and others.[2,9,74,93]

On the theoretical side, numerous simulation studies have appeared, in order to explain observed spectra and to predict the stability of the trapped impurity. Klein and co-workers used path-integral Monte-Carlo (PIMC) methods[70,94] to investigate the spectra and the nature of trapping sites for a single atomic lithium impurity trapped in *para*-hydrogen (pH_2) and *ortho*-deuterium (oD_2). We recall that pH_2 and oD_2 are the even-j isotopes which are spherically symmetric in the lowest state.

The calculations of Klein and co-workers indicated that a lithium atom appears to occupy preferentially a site with nearby vacancies. Using centroid path-integral molecular-dynamics (PIMD), they also looked at the diffusion and melting of semi-infinite slabs of pH_2 containing a Li impurity atom.[95] These authors used pair potentials to describe both the Li-pH_2 (or oD_2) and the pH_2-pH_2 (oD_2-oD_2) interactions. The assumption of pairwise additivity for the impurity atom-ligand potential is valid for Li, for which the electronic configuration of the ground state is spherical (^2S).

Jang and Voth used PIMD and centroid molecular dynamics (CMD) to investigate the stability with respect to recombination of the atomic impurities, Li and B, trapped in solid $p\mathrm{H}_2$.[71,72] Their calculations showed that B-doped systems can achieve a higher impurity concentration than Li-doped systems before recombination occurs. In their description of the B-H_2 interaction Jang and Voth neglected the angular anisotropy of the electron density of the B atom in its ^2P ground state.

Since B has a singly-filled 2*p* orbital in its ground state, its interaction with a spherical $p\mathrm{H}_2$ partner will depend on the orientation of the B orbital. The binary B-H_2 interaction is correctly described by two degenerate Π states and a Σ^+ state. If the *z*-axis is taken to be the internuclear axis, then these three states correspond to the three Cartesian orientations of the singly filled *p*-orbital (p_z for the Σ^+ state and p_x and p_y for the Π state). However, in the work of Voth and Jang, the B-H_2 interactions were treated using a single potential obtained by averaging over the three orientations of the 2*p* orbital.

Alexander *et al*. were the first to take into account the electronic anisotropy of the ground state B atom in a cluster,[12,13] using the model due to Balling and Wright,[14] discussed in Chap. 2 of this thesis. This work was then extended to include correctly the orbital degeneracy in simulations of a single B atom in solid $p\mathrm{H}_2$ (with Jang and Voth).[15] This investigation showed that the orientation of the B electronic charge distribution significantly affects the energetics of the trapped atom and the orientation of the nearby $p\mathrm{H}_2$ molecules. Small distortions of the lattice occur to allow an energetically favorable orientation of the 2*p* orbital, even in the absence of a vacancy.

The Balling and Wright model[14] was used earlier by Boatz and Fajardo to estimate the energies of Na in its 3*p* (^2P) excited state embedded in solid Ar. With this model, they used classical Monte-Carlo simulations to calculate the optical absorption spectra of Na trapped in clusters, on surfaces and in matrix sites of Ar.[96]

More recently, a closely related, but classical molecular dynamics simulation based on a diatomics-in-molecules (DIM) treatment of the potential was used to study the magnetic and optical properties of atomic B in rare gas matrices.[97,98] In both cases, the interaction of the ^2P electronic states with an arbitrary positioned rare gas atom is described by the rotation of a diagonal interaction matrix, the elements of which are the Π_x, Π_y and Σ^+ interaction potentials. In these treatments the interactions involving an open-shell atom are described in a more realistic manner by the assumption of a pairwise-additive Hamiltonian matrix rather than a pairwise-additive scalar potential.

Mirijanian, Alexander and Voth further extended the quantum simulations studies of Alexander and co-workers[15] to an atomic Al impurity.[16] The same trend was found for Al as for B: The orientation-dependent Al-pH$_2$ potential induces some distortion of the nearest-neighbor ligand shell to allow the Al p-orbital to orient itself to minimize the repulsive Σ and maximize the attractive Π interactions (For Al-pH$_2$ the V_Σ and V_Π potentials are plotted in Fig 4.1).

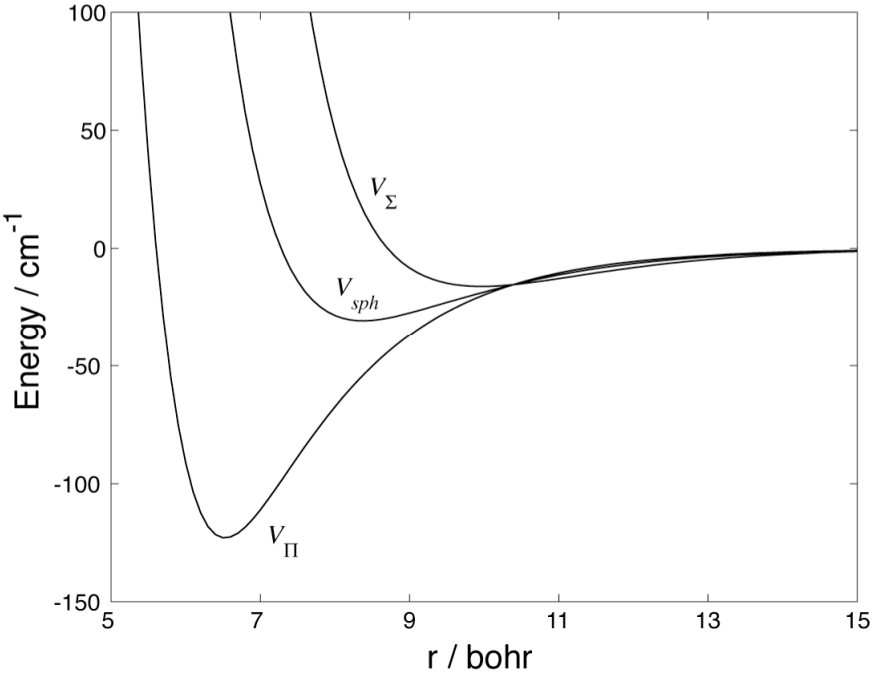

Fig 4.1 Potential curves of the Al-pH$_2$ pair. The spherical average over the three possible orientations of the 3p orbital, V_{sph}=2/3V_Π+1/3V_Σ, is also shown.

For open-shell atoms such as B and Al, one important question remains unanswered: when doped with multiple atomic impurities, is the system stable with respect to recombination, a highly exothermic process? To study more than one doped open-shell atom, we must consider the interaction between impurity atoms, which depends on the relative orientation of the *p*-electrons of both dopants.

As described in Chapter 3 of this thesis, in an earlier article we developed a theoretical framework for the accurate description of the interaction of two ^2P atoms in the presence of multiple spherical ligands.[99] We included a demonstration application to the interaction of two Al atoms embedded in solid $p\mathrm{H}_2$, site-substituted in the center of two adjacent hexagons. When the hydrogen molecules were fixed at their lattice positions, there appeared to be a significant barrier to recombination of the two Al atoms.[99] In this chapter we will relax this constraint, to allow for the motion of the H_2 molecules, which may be considerable even at temperatures below 5K. To do so requires a complete quantum simulation.

Toward this goal, we carried out a series of PIMC simulations of solid $p\mathrm{H}_2$ (or $o\mathrm{D}_2$) with two Al atoms site-substituted in different initial positions. The aim is to understand the equilibrium stability of the trapped Al impurities and the changes in the solid structure when multiple Al dopants are added. In the next section we shall describe the method. In the results section we describe the calculations we have done so far. We close with a brief conclusion.

4.2 Simulation methods

4.2.1 Model and potentials

The modeling of the interactions is fully described in several earlier papers.[16,99] We use the Silvera-Goldman potential[91] to describe the interactions between the $p\mathrm{H}_2$ molecules, which we assume spherical. The Al-$p\mathrm{H}_2$ and Al–Al

potentials are based on accurate *ab initio* calculations by Alexander *et al.*[100] The same potential has been used to study the Al-*o*D_2 system. We construct the potential matrix in a basis of diabatic Cartesian states, and then add the matrix of the spin-orbit operator in the same Cartesian orbital basis. The lowest eigenvalue of the matrix defines, in an adiabatic approximation, the potential which governs the motion of the particles.

As discussed in the Introduction, when a single Al atom is embedded in solid *p*H_2, the three fold degeneracy of Al in its $3s^2 3p$ electronic ground state is split by the interaction with *p*H_2 into two degenerate Π states and a Σ^+state. The corresponding potentials are labeled V_Π and V_Σ (see Fig. 4.1). In the 6-fold basis of the $3p_x$, $3p_y$ and $3p_z$ orbitals with both up and down spin, the matrix is diagonal. The matrix elements are V_Π and V_Σ. This assumes that the *p*H_2 is positioned along one of the Cartesian axes. Within the Balling and Wright model,[14] if the *p*H_2 molecule is instead positioned at some arbitrary position (r, θ, ϕ), then the interaction, in the fixed $p_x\ p_y\ p_z$ basis can be described by an orthogonal transformation (rotation) of this diagonal matrix.

The interaction of the Al atom with an arbitrary number of *p*H_2 ligands is then a sum of similarly rotated matrices. To this is added the matrix of the spin-orbit operator in the $p_x\ p_y\ p_z$ Cartesian orbital basis. The lowest root of the sum of these matrices, plus the sum of the scalar H_2–H_2 interactions, defines the potential for motion of the Al and *p*H_2 molecules. For comparison, we will use a scalar Al–H_2 potential, which is the spherical average over the three possible orientations of the $3p$ orbital, namely, $2/3 V_\Pi + 1/3 V_\Sigma$.[16]

When two Al atoms are embedded, the construction of the potential is considerably more complicated, as described in detail in Chapter 3. First, one needs accurate *ab initio* potential energy curves for all the 36 Al_2 electronic states which correlate to dissociation into ground-state Al (^2P) atoms. Consequently, making use

of a valence-bond-like model, we can transform these 36 molecular orbital states into a set of 36 states which correspond to assigning the two 3*p* electrons to Cartesian orbitals centered on each atom. Once this is done, it is straightforward to use the Balling and Wright model[14] to determine, in the 36 state basis, the matrix elements corresponding to the interaction of each ^2P atom with any number of surrounding spherical ligands. Within the adiabatic approximation, the lowest eigenvalue of the resulting 36×36 matrix defines the potential governing the motion of the molecules.[99]

4.2.2 Simulation in a canonical ensemble

For solid $p\mathrm{H}_2$ at 4K the thermal de Broglie wavelength[31,101] $\lambda=\left(2\pi\hbar^2/mk_BT\right)^{1/2}$ is ~ 11.6 bohr. Since this is larger than the lattice constant (~ 7.2 bohr), solid $p\mathrm{H}_2$ must be treated as a quantum solid.[23]

The exchange of H_2 molecules is unimportant in the solid.[19,23,102] Also because the Al atom is considerably heavier, its behavior will be more nearly classical. Consequently we assume that all the particles in our simulation obey Boltzmann statistics, to which the primitive PIMC method described in Chapter 1 is directly applied. This was the approach followed by Neumann, Zoppi *et al*. in simulations of pure $p\mathrm{H}_2$ at T=18.9K,[33,102,103] except that the "intramolecular" coordinates of their chain were sampled directly from a multivariate Gaussian distribution [*i.e.*, the contribution to the Boltzmann factor originating from the first term in the exponential in Eq. (1.15) is sampled directly]. For our system at 4K, we found the spread of the free particle to be appreciably larger than the length over which the potential energy changed significantly, so the rate of accepted moves is low and efficiency is not greatly improved, as was pointed out by Neumann, Zoppi *et al*.[33] In this thesis we will report only results obtained by the primitive PIMC algorithm.

In our simulations, the number of particles is kept at N=180. Initial

configurations are created by stacking together 5×3×3 copies of the unit cell of the hcp lattice (containing four particles each), to match the experimental density of pure solid *para*-hydrogen, namely 23.1cm^3/mol.[92] The result is an almost cubical simulation box (35.81×37.22×35.09 bohr^3, or 18.95×19.69×18.57 Å^3), to which periodic boundary conditions are applied. Thus, the static lattice energies we report below apply to 180 particles in a single simulation box, unless otherwise specified. (The structure of the hcp lattice is illustrated in Fig 3.4.)

We start the simulation by first obtaining an equilibrated slice configuration for solid pH$_2$. We adjust the parameters (Trotter number, step size, acceptance ratio) during the process. In the Monte-Carlo procedure we move each of the p slices sequentially, but within each slice all N particles are moved simultaneously. The Metropolis rejection/acceptance algorithm is imposed after the displacement of each slice. Sequential displacement of all p slices is called a cycle. Over 500,000 cycles were performed in each run prior to data acquisition to insure initial equilibration of the system.

While the primitive algorithm is sometimes regarded as inefficient,[19] it is easy to implement. To be cautious, we carried out an error analysis identical to that described in section 1.3.5 in Chapter 1 for pure solid hydrogen. The "size" of the quantum particles, which we estimate by the rms delocalization about the average position, is calculated and compared with previously published simulations for pH$_2$ at similar temperatures and densities.

A rough criterion for choosing the Trotter number p was set by Berne and Thirumalai,[20]

$$p >> \frac{\beta\hbar^2}{m{r_0}^2} \tag{4.1}$$

where r_0 is the length scale over which $V(x)$ changes. The Silvera-Goldman H$_2$–H$_2$ potential has a minimum energy of –22.07 cm^{-1} at 6.52 bohr, and a full width at half

minimum of ~ 2.13 bohr. If we set r_0 ~ 1 bohr, p should be bigger than 21. Voth *et al.*[15,16] used p=48 in PIMD studies of both pure and doped $p\mathrm{H_2}$. Other PIMC studies of pure $p\mathrm{H_2}$ have used values of p ranging from 4 to 64.[33,102] We set the Trotter number successively to 25, 48, 68 and 98 in order to monitor the convergence.

As a final check to our method, we replaced one $p\mathrm{H_2}$ molecule with an Al atom after first obtaining an equilibrated solid $p\mathrm{H_2}$ configuration. The resultant Al-$\mathrm{H_2}$ pair correlation function $g_{\mathrm{Al-H_2}}$ was compared to that obtained from Voth's earlier PIMD simulations under the same conditions.[16]

We start the simulation of multiple Al dopants by site substituting two $p\mathrm{H_2}$ molecules in the center of two adjacent hexagons (either sharing sides, or sharing a single vertex), or in the center of two next-nearest-neighbor hexagons, or in two adjacent layers. After a run has completed, we save $g(r)$, as well as the equilibrium positions and average energies. For comparison, a simulation of Al doped in solid $o\mathrm{D_2}$ was also done for site-substitution in two side-by-side adjacent hexagons.

The maximum step size Δ is taken to be the same in each dimension for $p\mathrm{H_2}$. Since the rms delocalization of particles in a harmonic potential is proportional to $m^{-1/2}$, and since Al is ~13 times heavier than $\mathrm{H_2}$, we use a smaller step size for the displacements of the Al atoms by imposing a maximum Al step size of $\Delta_{\mathrm{Al}}=\Delta_{\mathrm{H_2}}/3$. For the Al–$o\mathrm{D_2}$ system, we keep the same ratio of step sizes. The value of $\Delta_{\mathrm{H_2/D_2}}$ controls the fraction of random moves which are accepted. In each simulation, we adjusted $\Delta_{\mathrm{H_2/D_2}}$ to obtain an acceptance ratio x_A of ~ 0.35. In this way we neither wasted nor accepted too many steps.

4.3 Results and discussion

4.3.1 Solid $p\mathrm{H_2}$ and $o\mathrm{D_2}$

Some results of our PIMC simulations on pure solid $p\mathrm{H_2}$ / $o\mathrm{D_2}$ are listed in Table 4.1. All calculations were performed at a temperature of 4K. Each simulation was started from a perfect hcp lattice and consisted of a production stage of $3000 \times N_M$ cycles subsequent to the equilibration stage. Here N_M is the "dilution factor", the number of cycles skipped between configurations which are saved for analysis. A total of 3000 configurations were analyzed in each run. The value of N_M was taken to be 150 except the run for Trotter number p=98, for which N_M =500. In the Table $\Delta_{\mathrm{H_2/D_2}}$ is the maximum step size for $p\mathrm{H_2}$ / $o\mathrm{D_2}$. Here s is the correlation length for the effective energy V_{eff}. As an example, the plot of $M_b\sigma^2(\langle V_{eff}\rangle_b)/\sigma^2(V_{eff})$ *vs.* $M_b^{1/2}$ (as defined in Chapter 1 section 1.3.5) is shown for the run of p=25 in Fig. 4.2. The pair correlation functions for $p\mathrm{H_2}$ and $o\mathrm{D_2}$ are plotted in Fig 4.3. For $p\mathrm{H_2}$, Trotter numbers of p=48, 68 and 98 give virtually the same curve, while the p=25 curve is not converged to the same extent. The sharper peaks in the correlation function reveal that the heavier $o\mathrm{D_2}$ molecules are more localized about their equilibrium lattice sites.

Table 4.1 PIMC simulations of solid $p\mathrm{H_2}$ / $o\mathrm{D_2}$ with the Silvera-Goldman potential and N=180 particles at 4K. Here, p is the number of beads (Trotter number), $\Delta_{\mathrm{H_2/D_2}}$ is the maximum step size for $p\mathrm{H_2}$ / $o\mathrm{D_2}$, x_A is the fraction of accepted trial moves (acceptance ratio), s is the correlation length for the effective energy, and R is the rms delocalization of the quantum particles. Also E_k and U are the total kinetic and potential energies. The statistical uncertainties were determined as described in section 1.3.5. The kinetic energy per particle, E_k/N is also listed. The results are based on 3000 configurations out of each run, with dilution factor = 150 except for p=98, where a dilution factor of 500 was used. The numbers marked "p=∞" have been obtained by linear extrapolation as a function of 1/p.[102]

	p	$\Delta_{\mathrm{H_2/D_2}}$ (bohr)	x_A	s	$R_{\mathrm{H_2/D_2}}$ (bohr)	$E_{k_{\mathrm{H_2/D_2}}}$ ($\mathrm{cm^{-1}}$)	$U_{\mathrm{H_2/D_2}}$ ($\mathrm{cm^{-1}}$)	$E_{k_{\mathrm{H_2/D_2}}}/N$ ($\mathrm{cm^{-1}}$)	$U_{\mathrm{H_2/D_2}}/N$ ($\mathrm{cm^{-1}}$)
$p\mathrm{H_2}$	25	0.15	0.333	16	1.348	6786±10	−19949±8	37.70±0.06	−110.8±0.04
	48	0.12	0.358	18	1.307	7933±29	−19481±18	44.07±0.16	−108.2±0.10
	68	0.10	0.379	20	1.288	8291±34	−19316±15	46.06±0.19	−107.3±0.08
	98	0.08	0.408	8	1.270	8526±37	−19256±17	47.37±0.21	−107.0±0.09
	∞				1.235	9155±39	−19012±56	50.9±0.22	−105.6±0.31
$o\mathrm{D_2}$	48	0.10	0.301	20	1.088	5381±20	−20935±37	29.90±0.11	−116.3±0.21

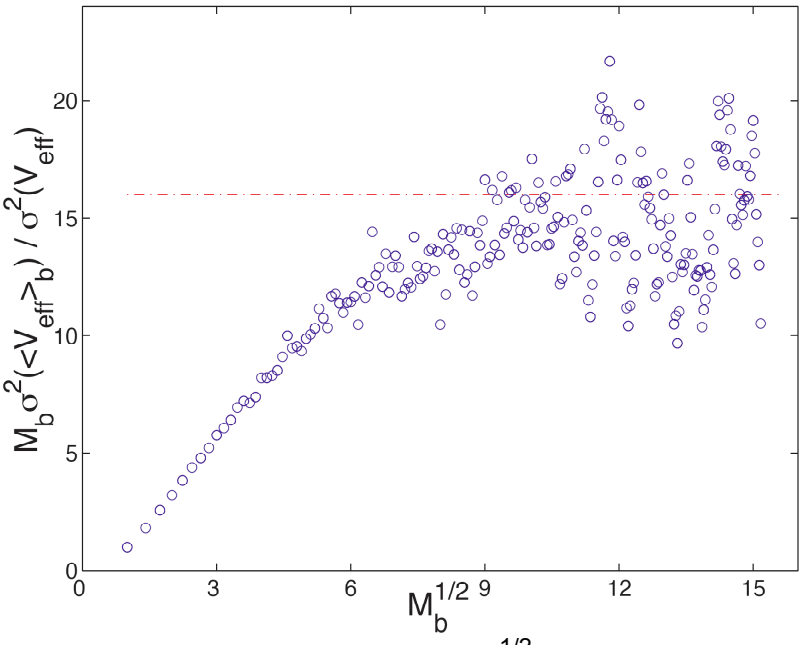

Fig 4.2 Plot of $M_b\sigma^2(\langle V_{eff}\rangle_b)/\sigma^2(V_{eff})$ against $M_b^{1/2}$ [Eq. (1.37)] with p=25. A plateau value of s=16 is obtained. This means that only one configuration in every 2400 cycles (the product of s times the dilution factor of 150) contributes completely new information to the average.

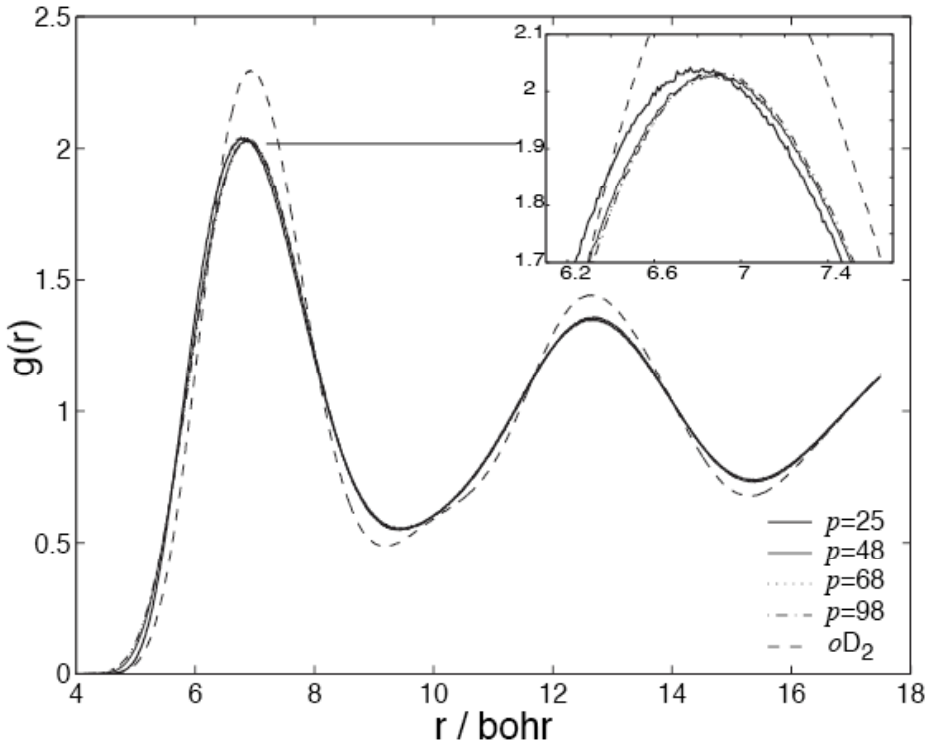

Fig 4.3 Pair correlation functions for pure $p\mathrm{H}_2$ and $o\mathrm{D}_2$. For $p\mathrm{H}_2$, results are shown corresponding to simulations with different Trotter numbers p.

Zoppi and Neumann[102] determined that the rms delocalization of pure solid hcp $p\mathrm{H}_2$ described by a Lennard-Jones interaction potential at 18.9K with density ρ=28.27 nm^{-3} was 0.888 bohr, with a smaller value at higher densities. The rms delocalization we report here is considerably greater because we are at a lower density and a lower temperature, where quantum effects are more significant. If we compare the particle localization, defined as the rms delocalization divided by the lattice constant (7.163 bohr here), our value of ~0.18 for $p \geq 48$ agrees well with Goldman's theoretical calculation (0.18)[92] and Nielsen's neutron scattering measurement (0.192±0.006).[104] The comparable value for $o\mathrm{D}_2$ is 0.15, which also agrees with Goldman's theoretical calculation,[92] although no experimental value is available. Because of the heavier mass the quantum delocalization is smaller for D_2.

Also listed in Table 4.1 are values for the average kinetic and potential energies. The correlation length s was estimated separately for the kinetic energy and potential energy, because these properties converge at different rates. We see that the kinetic energy is comparable in magnitude to the static lattice energy, and the kinetic energy per particle is much greater than k_BT (k_BT=2.78 cm^{-1} at T=4K), a characteristic of a quantum solid. In Kelvin units, the average kinetic energy of a hydrogen molecule is 63.4±0.2K (p=48), which agrees with the result of Jang and Voth's constatnt pressure PIMD simulation (62.7±0.1K) under the same conditions.[72] The kinetic to potential energy ratio increases as p increases. Following suggestions by several authors,[102] we used linear extrapolation as a function of $1/p$ to estimate the limits as $p \rightarrow \infty$.

For $p\mathrm{H}_2$, the limiting value of the total kinetic energy is about half of the average potential energy depth. Because of the smaller quantum effect, the kinetic energy for $o\mathrm{D}_2$ decreases about 30%. Also the static lattice energy is 7.5% lower in the presence of this smaller distortion to the lattice structure than that of $p\mathrm{H}_2$. The potential energy per $p\mathrm{H}_2(o\mathrm{D}_2)$, $U_{\mathrm{H}_2/\mathrm{D}_2}/N$ (N=180), ranges from −105.6 to

-116.3 cm^{-1}. In Kelvin units, the average interaction potentials between hydrogen molecules is 155.7±0.2K (p=48), which agrees with the result of Jang and Voth's constant pressure PIMD simulation (152.3±0.1K) under the same conditions.[72] The Silvera-Goldman potential[91] which we use to describe the binary interactions for $p\mathrm{H}_2$ (or $o\mathrm{D}_2$) molecules has a minimum of -22.07 cm^{-1} at a distance of 6.52 bohr. At the lattice distance 7.16 bohr for solid $p\mathrm{H}_2$ / $o\mathrm{D}_2$, the value of this potential is -18.41 cm^{-1}. For a molecule in an hcp lattice with 12 nearest neighbors, an estimate of the potential energy per $p\mathrm{H}_2$ / $o\mathrm{D}_2$ can be obtained by multiplying -18.41 cm^{-1} by 6, ~ -110 cm^{-1}, comparable to our results in Table 4.1.

Using a discrete variable representation (DVR) method (Appendix 4.I), we calculate the zero-point kinetic energy per $p\mathrm{H}_2$ / $o\mathrm{D}_2$ in the dimer to be 2.4 / 2.7 cm^{-1}. In simulations of pure solid $p\mathrm{H}_2$ / $o\mathrm{D}_2$ we found that the kinetic energy per molecule in the solid was much higher than that in an isolated dimer. Also, the kinetic energy is approximately proportional to $m^{-1/2}$ for $p\mathrm{H}_2$ / $o\mathrm{D}_2$, which is reasonable since we use the same potential for both. For a harmonic oscillator, the zero-point kinetic energy is just $\hbar\omega/4$.

4.3.2 One Al atom in $p\mathrm{H}_2$

The first two rows in Table 4.2 present some results from our simulation study of Al impurities doped in $p\mathrm{H}_2$. Table 4.3 lists the corresponding energies. The pair correlation function for one Al atom site-substituted in solid $p\mathrm{H}_2$ is shown in Fig 4.4. As discussed in section 4.2.1, simulations were carried out with both the correct anisotropic Al-H_2 potential and a spherically averaged potential. The resulting curves agree well with those from Voth's earlier PIMD simulation at the same temperature and density, and based on the same potentials.[16]

One interesting result is that the degree of delocalization of the Al atom predicted by the spherically averaged potential is considerably greater than when the orientation dependent potential is used (as shown by the values of R_{Al} in Table 4.2). This might be a result of the non-uniform electronic density of the Al atom. By comparing with the pair correlation functions for pure solid $p\mathrm{H_2}$ (Fig 4.4), we see that the embedded Al atom acts to push the nearest neighbor $p\mathrm{H_2}$ molecules away.

By fitting with a Gaussian function the first peak of the correlation function for the spherically averaged Al–$\mathrm{H_2}$ potential, we can use Eq. (1.19) to estimate the number of particles present in the first solvation shell. The number is 12.7. In a rigid hcp lattice the number of nearest neighbors is 12. Thus, we conclude that for the spherically averaged $\mathrm{AlH_2}$ potential, the nearest-neighbor $p\mathrm{H_2}$ molecules are pushed away uniformly.

However, as we might have anticipated, for the anisotropic Al–$\mathrm{H_2}$ potential, the displacement of the nearest-neighbor $p\mathrm{H_2}$ molecules is no longer uniform. The first peak in the correlation function splits into two merged peaks. We can fit these with two Gaussian functions, obtaining 5.7 and 6.7 for the number of particles contained in the inner and outer shoulders, respectively. Thus the 12 nearest neighbors are divided into two groups: 6 stay at roughly their nominal hcp positions, while 6 others are pushed farther away than in the case of the spherically averaged Al–$\mathrm{H_2}$ potential. Those molecules which have been pushed farthest away contribute to the shoulder peak at ~8.1 bohr.

The $\mathrm{H_2}$ molecules which lie outside the first solvation shell are little affected by the electronic anisotropy, as can be seen in the shape of the second peak in the correlation function at ~12.4 bohr. The maximum is not shifted. The shape of the peak is only slightly changed.

Table 4.2 PIMC simulations of solid $p\mathrm{H}_2$ / $o\mathrm{D}_2$ with doped Al impurities at 4K. Total N=180 particles. Trotter number p=48. $\Delta_{\mathrm{H}_2/\mathrm{D}_2}$ is the step size for $p\mathrm{H}_2$ / $o\mathrm{D}_2$[a]. x_A is the acceptance ratio, s is the correlation time for the effective energy, and R the rms delocalization of the quantum particles. The results are based on 3000 configurations out of each run, with dilution factor = 150, except that the rms delocalizations are based on 100 configurations, with a dilution factor of 500.

	$\Delta_{\mathrm{H}_2/\mathrm{D}_2}$[a] (bohr)	x_{A}	s	$R_{\mathrm{H}_2/\mathrm{D}_2}$ (bohr)	R_{Al} (bohr)
$p\mathrm{H}_2$ + 1Al [anisotropic Al–H_2 potential]	0.12	0.356	40	1.303	0.443
$p\mathrm{H}_2$ + 1Al [spherical Al–H_2 potential]	0.12	0.356	20	1.314	0.657
$p\mathrm{H}_2$ + 2Al [case (a)][b]	0.12	0.353	27	1.299	0.663
$p\mathrm{H}_2$ + 2Al [case (b)][c]	0.12	0.355	20	1.302	0.502
$p\mathrm{H}_2$ + 2Al [case (c)][d]	0.12	0.354	14	1.296	0.611
$p\mathrm{H}_2$ + 2Al [case (d)][e]	0.12	0.355	17	1.295	0.561
$p\mathrm{H}_2$ + 2Al [case (b), spherical potential][c]	0.12	0.352	18	1.303	0.483
$p\mathrm{H}_2$ + 2Al [case (c), spherical potential][d]	0.12	0.354	16	1.287	0.575
$o\mathrm{D}_2$ + 2Al [case (a)][b]	0.10	0.300	20	1.097	0.505

[a] Step size for Al $\Delta_{\mathrm{Al}} = 1/3\,\Delta_{\mathrm{H}_2}$

[b] case (a): two Al atoms site-substituted at two lattice points in the center of two side-sharing adjacent hexagons

[c] case (b): two Al atoms site-substituted at two lattice points in the center of two vertex-sharing adjacent hexagons

[d] case (c): two Al atoms site-substituted at two lattice points in the center of two next-nearest neighboring hexagons

[e] case (d): two Al atoms site-substituted at two lattice points in the center of two different layers

Table 4.3 PIMC results for energy of solid $p\mathrm{H}_2$ / $o\mathrm{D}_2$ with doped Al impurities at 4K. The simulation parameters are listed in Table 4.2. E_k and U are the kinetic and potential energies. E_k/N is the kinetic energy per particle.

	$E_{k\mathrm{Al}}/N_{\mathrm{Al}}$ (cm^{-1})	$E_{k_{\mathrm{H}_2/\mathrm{D}_2}}/N_{\mathrm{H}_2/\mathrm{D}_2}$ (cm^{-1})	U (cm^{-1})
$p\mathrm{H}_2$ + 1Al [anisotropic Al–H_2 potential]	16.85±1.37	44.49±0.20	−20041±13.4
$p\mathrm{H}_2$ + 1Al [spherical Al–H_2 potential]	15.61±1.73	44.57±0.11	−19700±15.1
$p\mathrm{H}_2$ + 2Al [case (a)]	37.06±1.30	44.84±0.16	−31597±12.9
$p\mathrm{H}_2$ + 2Al [case (b)]	18.83±1.36	45.15±0.15	−20643±9.4
$p\mathrm{H}_2$ + 2Al [case (c)]	18.29±1.23	45.18±0.09	−20675±10.1
$p\mathrm{H}_2$ + 2Al [case (d)]	16.57±1.41	45.08±0.10	−20700± 7.2
$p\mathrm{H}_2$ + 2Al [case (b), spherical potential]	34.92±1.18	44.89±0.10	−31224± 9.1
$p\mathrm{H}_2$ + 2Al [case (c), spherical potential]	14.75±1.23	45.43±0.11	−19943± 7.8
$o\mathrm{D}_2$ + 2Al [case (a)]	39.65±1.69	30.73±0.14	−33097±12.5

Table 4.4 Binding energy and equilibrium internuclear distance of the Al–H_2 and H_2–H_2 interaction

	H_2–H_2	Al($3p\ ^2P$)–H_2 (ground state)			Al–Al
	(D_2–D_2)	$^2\Sigma$	$^2\Pi$	Spherical ($2/3V_\Pi+1/3V_\Sigma$)	$^2\Pi_u$
R_e /bohr	6.52	9.96	6.53	8.38	5.39
D_e /cm^{-1}	−22.07	−16.05	−123.01	−30.65	−11471.42
Potential at lattice distance/cm^{-1}	−18.41	238.45	−104.26	9.98	−5643.32

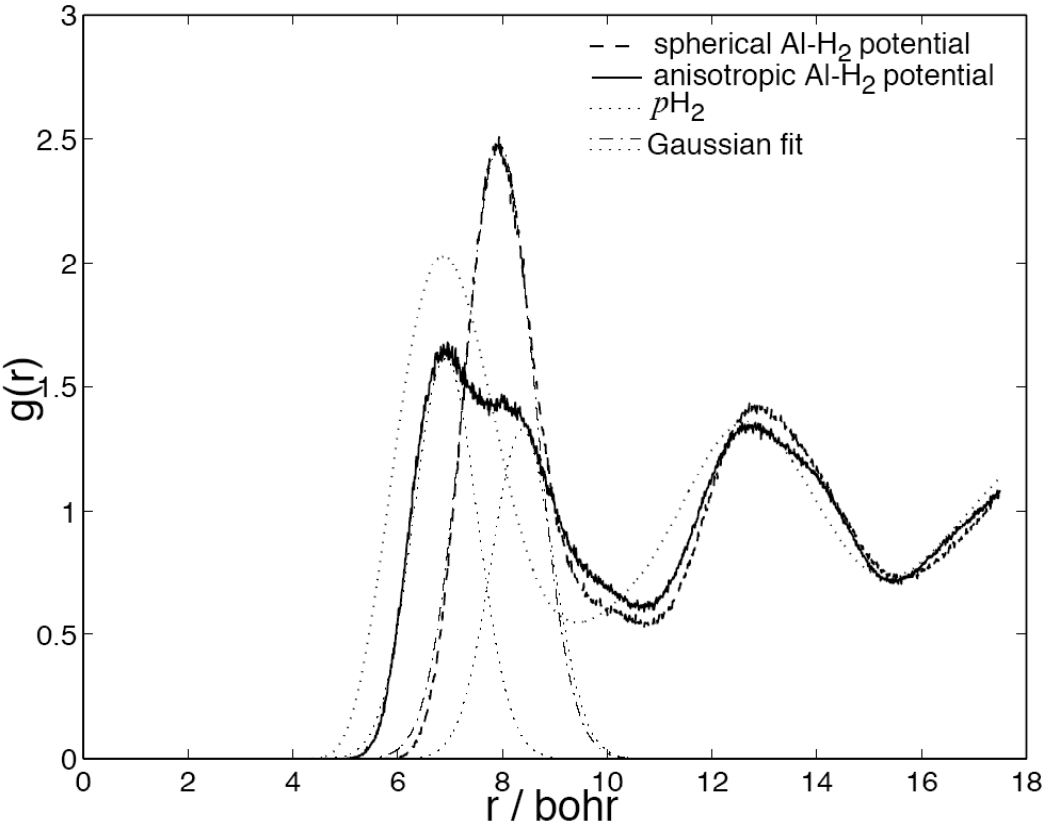

Fig 4.4 Al–H_2 pair correlation functions for one Al atom site-substituted in the solid, determined using the orientation dependent and spherically averaged Al–H_2 potentials. For comparison, the pair correlation function for pure solid p-H_2 is also shown.

To gain a more descriptive view of how the embedded Al atom(s) affect the positions of the $p\mathrm{H_2}$ molecule, we display, in Fig. 4.5 the average projection of the positions of the 12 nearest neighbors on the *xy* and *xz* planes (the *xy* plane is defined as the plane in which Al is hexagonally caged in the center of 6 nearest neighbor $\mathrm{H_2}$ molecules, see Fig 4.5). For the anisotropic potential (Fig 4.5.I), we see that the 6 nearest neighbors in the *xy* plane remain near the original positions, while the 6 others above and below the plane are pushed up and pushed aside almost uniformly along the vector which connects the Al atoms with each of the $p\mathrm{H_2}$ ligands.

In contrast, Fig 4.5.II shows comparable position projections but for the simulations based on the averaged (spherical) potential. Here all 12 $\mathrm{H_2}$ molecules are displaced outward to the same extent. One possible explanation of the difference between two figures is that the electron density of the Al atom is rearranged so that the *p* electron is confined to the p_z orbital, thereby minimizing the electron density in the *xy* plane. In this way, for the interaction involving the 6 in-plane ligands, the strong head-to-head V_Σ repulsion (Fig. 4.1) is avoided while the attractive V_Π interaction is maximized, so that the total potential energy is lowered. This is reflected in the average energies shown in Table 4.3. Compared to pure solid $\mathrm{H_2}$ (p=48, Table 4.1), embedding an Al atom lowers the total static lattice energy by ~ 220 $\mathrm{cm^{-1}}$ if the spherically averaged Al–$\mathrm{H_2}$ potential is used, and by ~ 560 $\mathrm{cm^{-1}}$ if the orientation dependent potential is used. In contrast, however, the kinetic energy of the $\mathrm{H_2}$ molecules does not change much.

As summarized in Table 4.4, the Silvera-Goldman potential[91] describing the $p\mathrm{H_2}$–$p\mathrm{H_2}$ interaction has a value of −18.41 $\mathrm{cm^{-1}}$ at the lattice distance 7.16 bohr. The minimum in the Silvera-Goldman potential (−22.07 $\mathrm{cm^{-1}}$) occurs at a closer distance of 6.52 bohr. The minimum in the spherically-averaged Al–$\mathrm{H_2}$ potential is −30.6 $\mathrm{cm^{-1}}$ and occurs at 8.38 bohr. The value of the V_Π potential is –104.26 $\mathrm{cm^{-1}}$ at

the lattice distance. The minimum in V_Π is –123.0 cm^{-1} at 6.53 bohr, and, in V_Σ, -16.1 cm^{-1} at 9.96 bohr.

In the case of the spherically-averaged potential, an estimate of the static lattice energy change can be obtained by multiplying the Al–pH_2 energy (-30.6 cm^{-1}) by 12 (the number of nearest neighbors) and then subtracting the 12 pH_2–pH_2 energies corresponding to the pH_2 which was replaced. This yields -146.3 cm^{-1}. Our result of ~ –220 cm^{-1} is lower by ~ 73 cm^{-1}, probably because of the next-nearest-neighbor contributions and the change in the H_2–H_2 energy engendered by the compression of the H_2 lattice when the Al atom is embedded.

For the anisotropic Al–H_2 potential, an estimate of the static lattice energy change can be obtained by multiplying –104.26 cm^{-1} by 6 (for the nearest neighbors in the same plane, which stay near the original lattice points and presumably mainly feel the V_Π attraction). We must again subtract the self-energy of the replaced pH_2. We obtain –515.1 cm^{-1}, comparable to the value of ~ –560 cm^{-1} form the simulation. Here too, next-nearest-neighbor interactions and the result of the compression of the H_2 lattice by the push of Al atom are probably responsible for the ~ 45 cm^{-1} discrepancy.

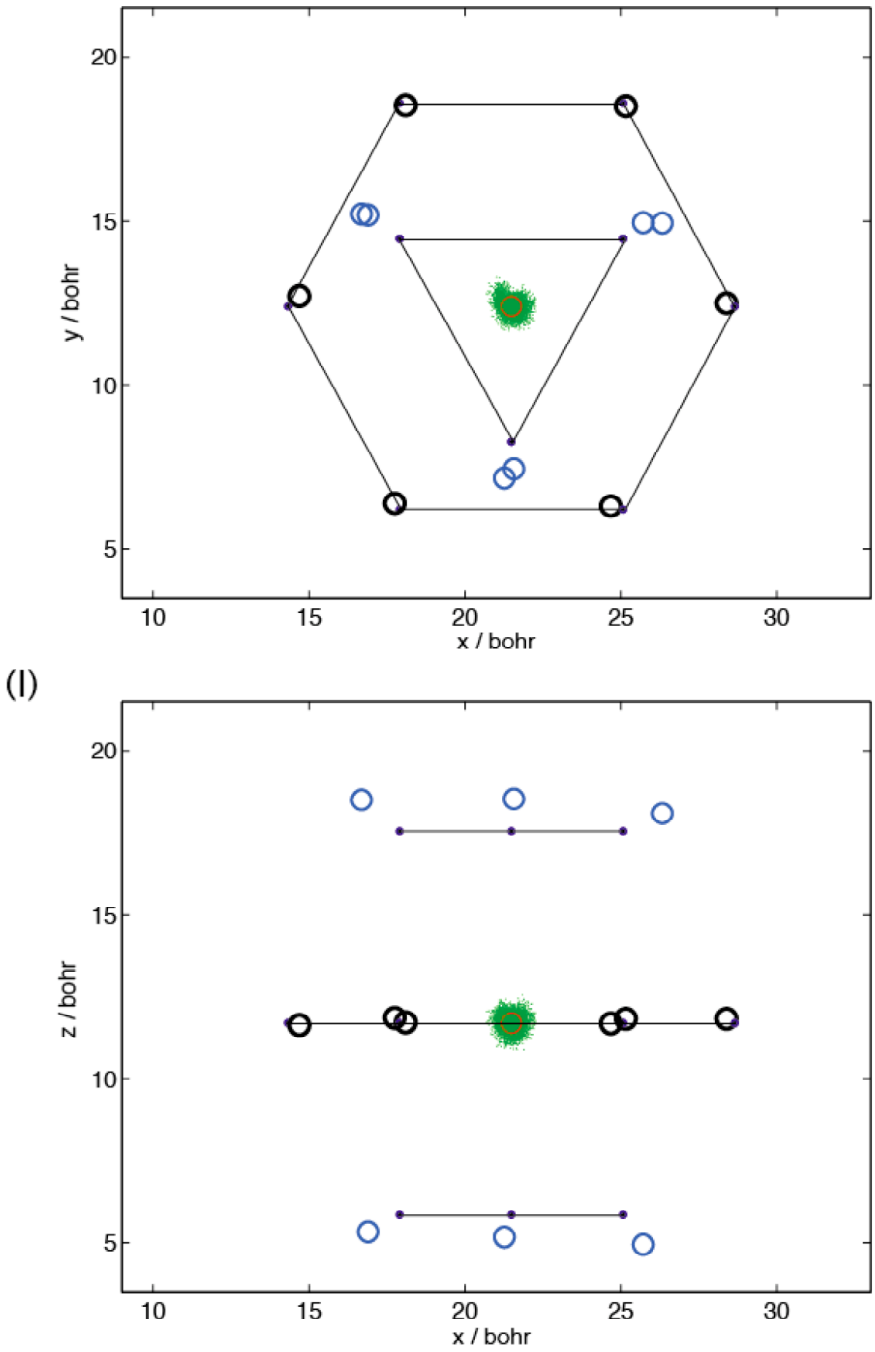

Fig 4.5 Positions of the 12 nearest-neighbor pH$_2$ molecules and the central, site-substituted Al atom impurity resulting from 100 PIMC configurations, with dilution factor of 500 and p=48, projected onto the xy and xz planes. The small filled circles (•) mark the positions of the hcp lattice sites. The open circles (o) designate the averaged positions of the pH$_2$ molecules and the Al atom. The positional spread of the Al atom from simulations with Trotter number p=48 is illustrated by the dotted points. To guide the eye, the hcp vertices lying in parallel xz planes are connected by straight lines. (I): Anisotropic Al–H$_2$ potential,

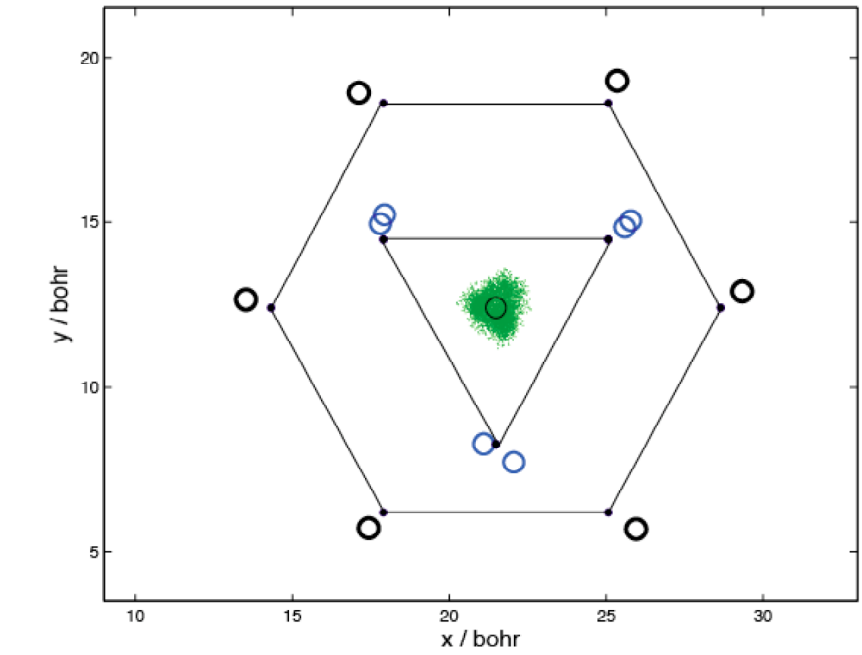

(II)

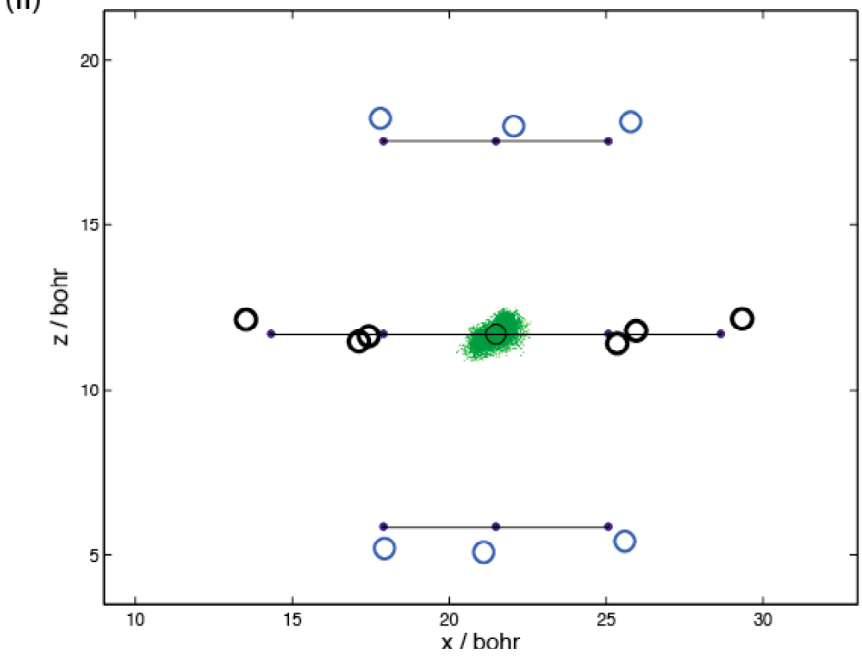

Fig 4.5 (II): Spherically averaged Al–H_2 potential.

4.3.3 Two Al atoms in pH_2

In the investigation of two Al atoms embedded in solid pH_2, we studied four initial locations for the atoms (Fig 4.6). In case (a), the Al atoms are in the center of two side-sharing adjacent hexagons. This is the closest distance (12.406 bohr) at which we can site substitute two Al atoms with at least one intervening pH_2 molecule. In case (b), the two Al atoms are centered in two vertex-sharing hexagons, at a distance of 14.325 bohr. In case (c), the two Al atoms are in two next-nearest-neighbor hexagons, at a distance of 18.951 bohr. In case (d), the two Al atoms are initially positioned in the centers of two neighboring hexagons located in adjacent hcp planes, at a distance of 16.016 bohr.

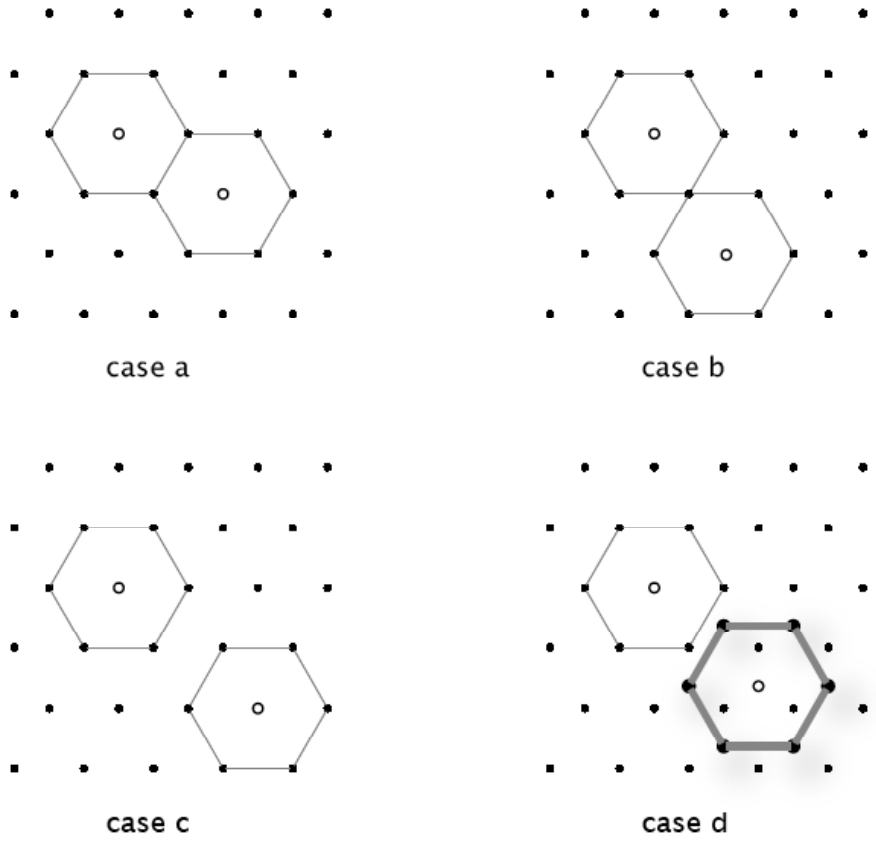

Fig 4.6 Position of site-substituted Al atoms in the center of two hexagons. The connection lines do not indicate actual bonds, but are inserted merely to guide the eye. Case (a): two side-sharing adjacent hexagons in one hcp plane; Case (b): two vertex-sharing adjacent hexagons in one hcp plane; Case (c): two next-nearest neighboring hexagons in one hcp plane; Case (d): two adjacent layers.

Figure 4.7(I) shows the Al–Al pair correlation functions after the PIMC simulations were run for these four cases. In case (a), the equilibrated distance between the two Al atoms is dramatically shifted inward compared with the initial separation. The Al–Al internuclear separation for the lowest Al_2 potential curve distance predicted by *ab initio* potentials is R_e = 5.39 bohr. Since this value corresponds to the maximum in the pair distribution function in Fig. 4.7(I), it is obvious that in case (a) the two Al atoms manage to move the H_2 molecules aside and recombine. For comparison purposes, a similar simulation was done on two Al atoms embedded in solid o-D_2. Here, too, the Al–Al pair distribution function indicates that the two Al atoms combine.

Figure 4.8(I) shows the distortion in the lattice structure reflected in the Al–H_2/D_2 pair correlation functions. In combining, the Al atoms actually move away from the closest hydrogens. This is manifested in the outward shift of the peaks in $g_{\text{Al-H}_2}(r)$. This tendency is even stronger in p-H_2 than in o-D_2. More insight is gained by the positional projections of the nearest neighbors shown in Fig 4.9. We see big distortions to the lattice structure; very few molecules remain close to their original lattice points. The two vertex H_2/D_2 molecules which lie between the original sites of the two Al atoms are pushed away dramatically so that the Al atoms can move toward each other. The tension on the lattice engendered by this large distortion in the *xy* plane is reduced by relocation of molecules out of this plane. Also, the distortion is not only localized in the layer containing the Al atoms. The four p-H_2/o-D_2 molecules which were initially above and below the final positions of the Al atoms are pushed away strongly and in a nonuniform manner, both in the *xy* plane and in the *z* direction.

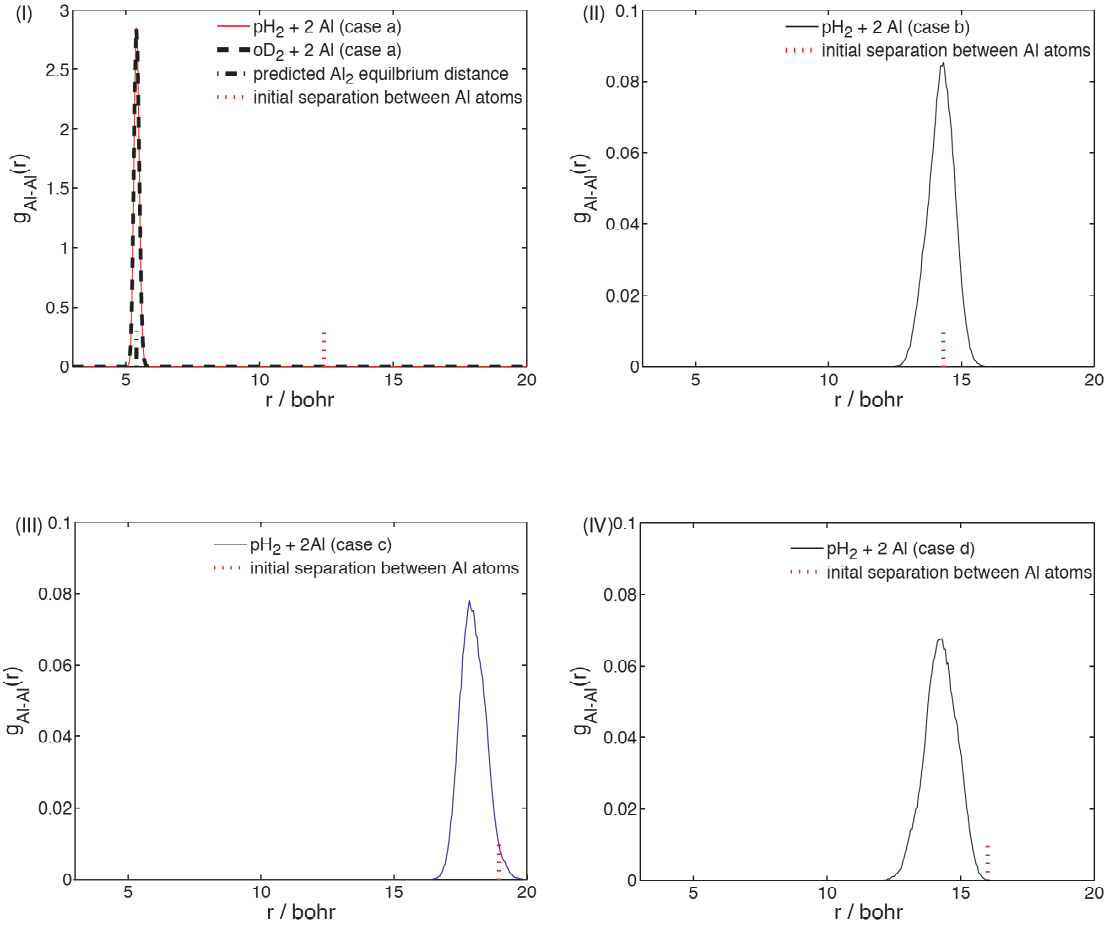

Fig 4.7 Al–Al pair correlation functions for two Al atoms site substituted in the solid. (I): case (a) substitution in *p*H_2 and *o*D_2; (II): case (b) substitution in *p*H_2; (III): case (c) substitution in pH_2. (IV): case (d) substitution in *p*H_2. The vertical bars indicate the initial separation between the Al atoms. In (I) the vertical bar at r=5.39 bohr indicates the Al_2 equilibrium distance predicted by our *ab initio* calculations.

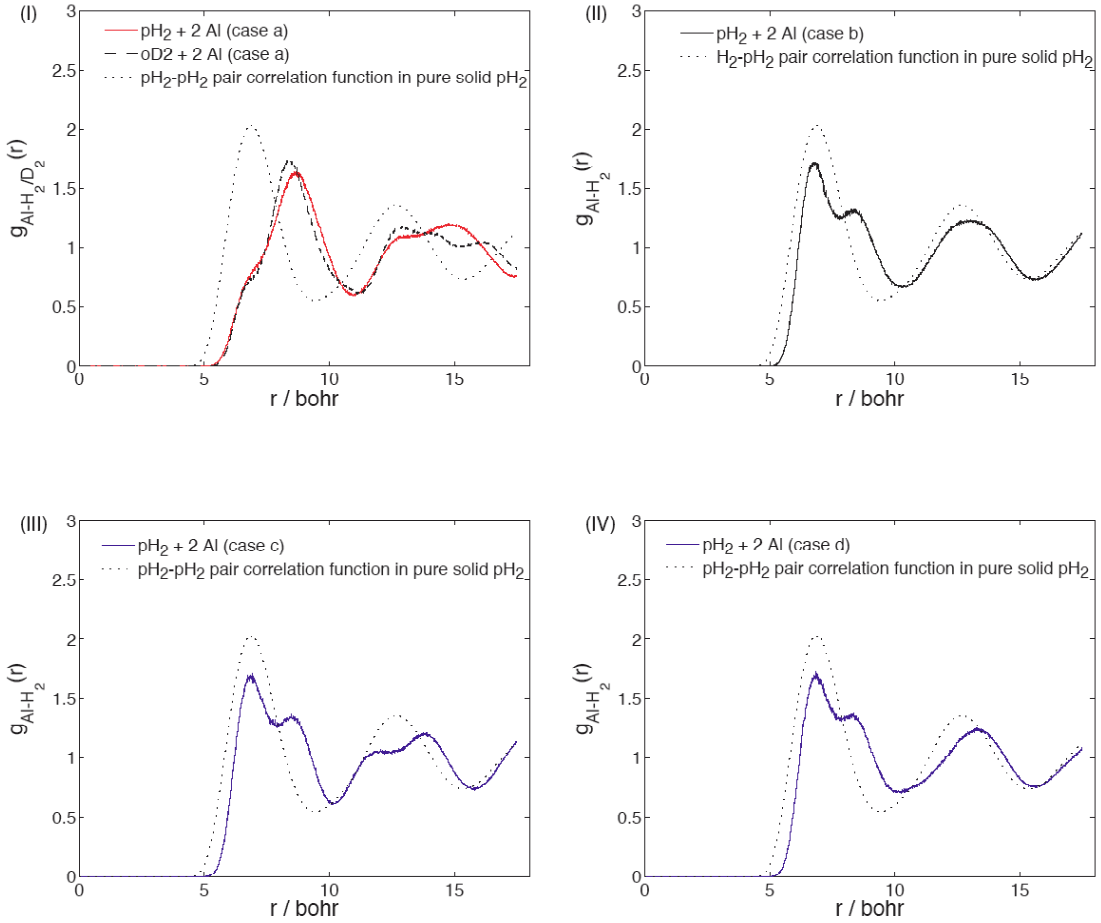

Fig 4.8 Al-ligand pair correlation functions for two Al atoms site substituted in the solid. (I): case (a) substitution in pH_2 and oD_2; (II): case (b) substitution in pH_2; (III): case (c) substitution in pH_2; (IV): case (d) substitution in pH_2. For comparison purposes the pair correlation function for pure solid pH_2 is also shown in each plot.

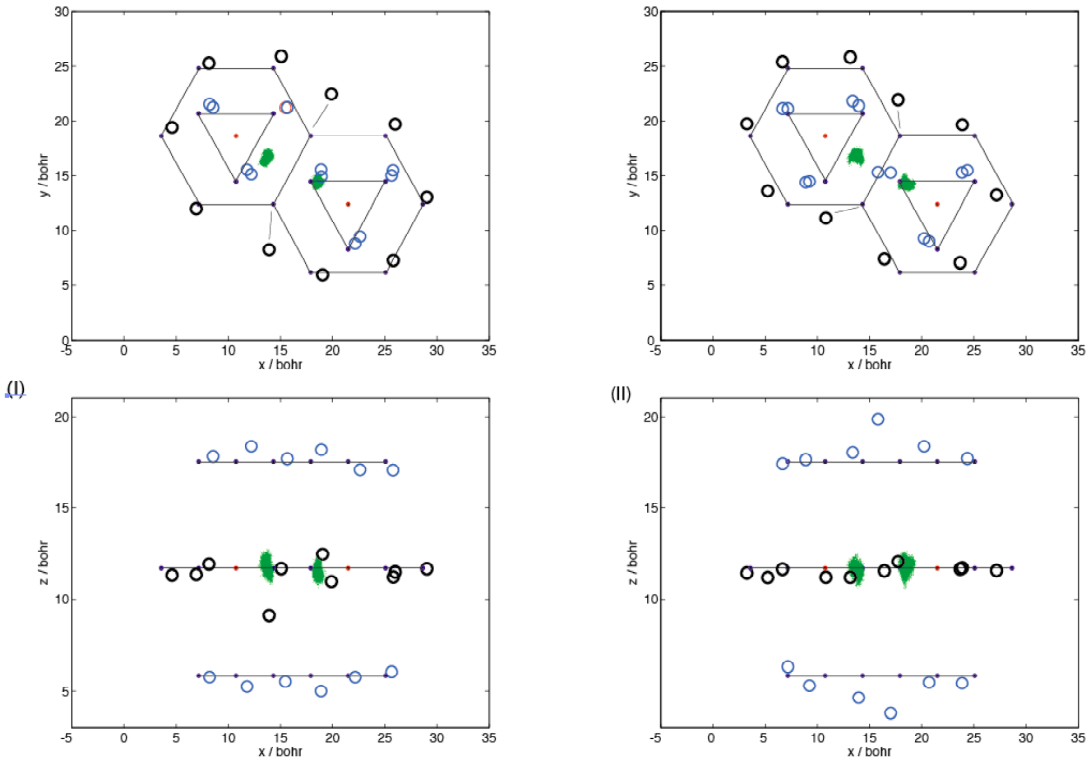

Fig 4.9 Positions of the 22 nearest-neighbor $p\mathrm{H_2}$ / $o\mathrm{D_2}$ molecules and the two central, case (a) site-substituted Al atoms resulting from 100 PIMC configurations, with dilution factor of 500 and p=48, projected onto the xy and xz planes. The filled circles (•) are the positions of the hcp lattice sites. The open circles (o) designate the averaged (centroid) positions of the $p\mathrm{H_2}$ / $o\mathrm{D_2}$ molecules and the Al atoms. The positional spread of the Al atom is illustrated by the dotted points. To guide the eye, the hcp vertices lying in parallel xz planes are connected by straight lines. (I): 22 $\mathrm{H_2}$ + 2 Al, (II): 22 $\mathrm{D_2}$ + 2 Al.

In case (b), the two Al atoms stay close to the original positions. In case (c) and case (d), the two Al atoms equilibrate at a somewhat shorter distance, but far from combining into an $\mathrm{Al_2}$ molecule [Fig 4.7(II), (III), (IV)]. In cases (b), (c), and (d) there are more intervening $\mathrm{H_2}$ molecules than in case (a). The Al–Al attraction is not strong enough to push all the $\mathrm{H_2}$ molecules away. If we neglect the dip in the shoulder, the first peak in $g_{\mathrm{Al\text{-}H_2}}(r)$ of Fig 4.8 [(II), (III), (IV)] strikingly resembles, both in position and shape, that in Fig 4.4 for the anisotropic Al–$\mathrm{H_2}$ potential. This indicates that each Al atom affects the $\mathrm{H_2}$ lattice structure separately.

Figure 4.10 shows the planar projections of the positions of the H_2 molecules for case (b), (c) and (d). Cases (b) and (c) are similar to the one Al atom impurity case; the H_2 molecules located in the same *xy* plane as an Al atom stay close to their original positions, while some H_2 molecules above and below this plane are pushed away. However, this displacement is not as uniform as in the case of the single atom impurity. Furthermore, there is a small overall translational motion of the lattice cage which accompanies the movement of the Al atoms. As a result, the two nearest neighbor cages move slightly closer in both case (b) and (c). In case (d), however, the in plane movement is a little larger. Presumably, when the two Al atoms are in different layers, the lattice distorts differently to accommodate the tension induced by the strong attraction between the Al atoms.

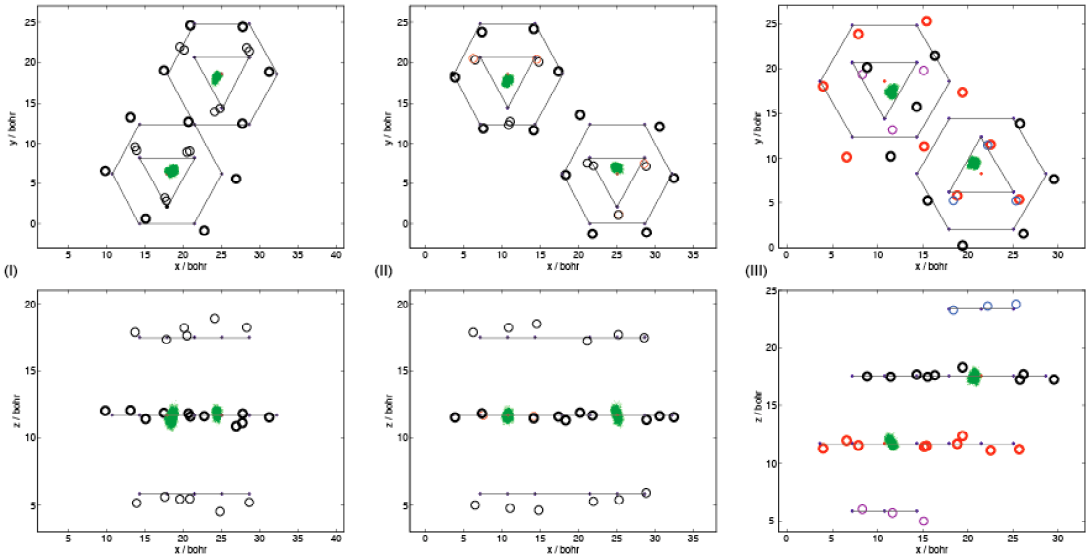

Fig 4.10 Positions of the nearest-neighbor *p*H_2 molecules and the two central, site-substituted Al atoms resulting from 100 PIMC configurations, with dilution factor of 500 and *p*=48, projected onto the xy and xz planes. The filled circles (•) are the positions of the hcp lattice sites. The open circles (o) designate the averaged positions of the pH2 molecules and the Al atoms. The spread in the positions of the Al atoms is shown by the dotted points. To guide the eye, the hcp vertices lying in parallel xz planes are connected by straight lines. (I): 23 H_2 + 2 Al (case (b) substitution), (II): 24 H_2 + 2 Al (case (c) substitution) (III): 24 H_2 + 2 Al (case (d) substitution).

Table 4.3 presents values for the average energies of solid $p\mathrm{H}_2$ / $o\mathrm{D}_2$ with doped Al impurities. The potential energies for case (a) compared with the pure solid drop by over 12100 cm^{-1}. The lowest of the Al–Al potential used in the simulation has a well depth of –11471 cm^{-1} at 5.39 bohr. For this state the zero-point-corrected dissociation energy is D_0 = 11319 cm^{-1} (determined using the DVR method described in Appendix 4.I). Clearly, then, the lowering in the energy of the solid when two atoms are embedded initially at the positions designated as case (a) corresponds to the release of the Al–Al bond energy.

Also, as in the pure solid, the static lattice energy for the $o\mathrm{D}_2$ system is lower than for $p\mathrm{H}_2$ by ~1500 cm^{-1}, since $o\mathrm{D}_2$ is more localized. In cases (b), (c) and (d), the addition of the two Al atoms reduces the potential energies by 580–610 cm^{-1} per atom. This number is close to the case of a single Al atom. This is a further confirmation that in cases (b) and (c) each Al atom affects the lattice separately. Further, there is only small interaction between the two Al atoms. The kinetic energy of the ligand $p\mathrm{H}_2$ / $o\mathrm{D}_2$ molecules varies little between the pure solid (Table 4.1), the mono-substituted solid and the bi-substituted solid [cases (a), (b), (c) and (d)]. In cases (b), (c) and (d), the kinetic energy of the Al atoms is very comparable to the mono-substituted solid.

However, we observe an increase in the average Al kinetic energy in case (a). Our DVR calculations show that in the ground vibrational level of the $^3\Pi_u$ state of Al_2 the expectation value of the kinetic energy is 77.2 cm^{-1} . This is completely consistent with the computed average kinetic energy for case (a) substitution: 37.1 cm^{-1} per Al atom. This means that the kinetic energy of the Al atoms in case (a) substitution is governed by the Al_2 molecular potential.

Figure 4.11(I) presents the potential energy profile associated with the recombination of the two Al atoms in case (a). The reaction coordinate is chosen to be the distance between the two Al atoms (x axis). The solid curve corresponds to a

calculation in which Al atoms are constrained to move symmetrically along the line of separation, while all $p\mathrm{H}_2$ molecules are frozen at the hcp lattice sites. This curve is similar to what we published earlier,[99] but with the imposition of periodic boundary conditions. When the $p\mathrm{H}_2$ molecules are frozen, we observe a substantial barrier to the recombination of the Al atoms at a distance of 10–12 bohr. The height of the barrier is 147 cm^{-1}, much greater than $k_B T$ at 4K (2.78 cm^{-1}).

However, when the constraints on the movement of $p\mathrm{H}_2$ molecules is relaxed, as shown in the dash-dot curve, which corresponds to a calculation in which Al atoms are still fixed at the nominal value of R, but the positions of all the $p\mathrm{H}_2$ molecules are allowed to relax, the barrier is reduced. As we have discussed in section 4.3.1, the quantum delocalization of the $p\mathrm{H}_2$ molecules is large, their kinetic energies are greater than $k_B T$. Consequently, solid $p\mathrm{H}_2$ is more flexible than a classical lattice, and can easily undergo large distortions to the lattice structure. It is the quantum nature of the $p\mathrm{H}_2$ molecules that allows the Al atoms to displace the $p\mathrm{H}_2$ molecules and thereby, to combine.

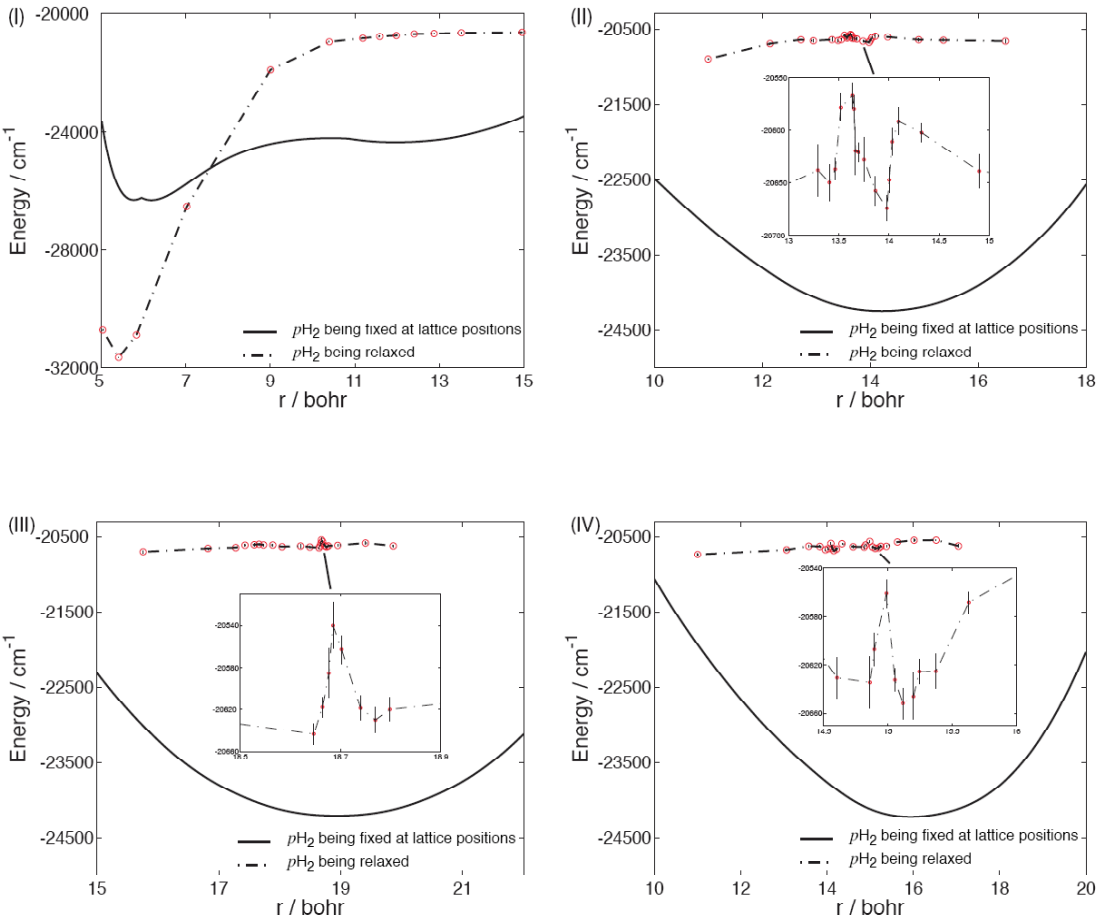

Fig 4.11 Total potential energy of 178 $p\mathrm{H}_2$ molecules with two doped Al atoms. The Al atoms are constrained to move symmetrically along the line of separation (see Fig. 4.6). The solid lines correspond to a calculation in which the hydrogen molecules are fixed at their lattice positions. The dash-dot lines correspond to a calculation in which the hydrogen molecules are allowed to relax. (I) case (a) substitution; (II) case (b) substitution; (III) case (c) substitution; (IV) case (d) substitution.

Since the two Al atoms recombine in case (a), but not in case (b), this observation may set a limit to the extent to which one could dope Al atoms into solid $p\mathrm{H}_2$. Suppose we were to dope multiple Al atoms into $p\mathrm{H}_2$, with each pair of Al atoms substituted into sites whose relative positions correspond to case (b). From simple geometric consideration, this lattice would correspond to a molar ratio of 1 Al : 15 H_2, or 0.07 mole percent.

4.3.4 Effect of electronic anisotropy

To explore the effects of the orientation of the Al electronic charge distribution on the energetics and stability of the trapped atoms, we carried out two case (b) and (c) simulations in which we neglected the electronic anisotropy of the Al atoms. To accomplish this we first assumed that the spherically averaged Al–H_2 potential describe the interaction of each Al atom with all the hydrogens, and, secondly, that the most attractive of the Al_2 potentials ($^3\Pi_u$) describes the interaction between the two Al atoms. Figure 4.12 shows the Al–Al pair correlation functions for these two cases. Interestingly, in case (b) the equilibrated distance peaks around the Al_2 dimer distance, which indicates that when described by the spherical Al–H_2 potential, the two Al atoms have combined. This is in contrast to the results, presented in the two preceding paragraphs, where we conclude that for case (b) the two Al atoms do not recombine when the electronic anisotropy of the Al atoms is described correctly.

In case (b), there is a single H_2 molecule which lies midway between the embedded Al atoms. Consequently, as discussed earlier, the 3*p* orbitals of the two Al atoms would prefer to be oriented perpendicular to the Al–H_2–Al plane, to minimize the repulsive energy. However, the orientation of the 3*p* orbitals in the $^3\Pi_u$ state of Al_2 corresponds to one orbital π and the other orbital σ. Thus, when the electronic asymmetry is taken into account, the presence of the intervening *p*H_2 molecule in case (b) prevents the two electrons in the two Al atoms from adopting the orientation which corresponds to the most attractive Al–Al interaction.

In case (c), the equilibrated distance is somewhat shorter than when the full electronically anisotropic potential is used, but still remains far from combining into an Al_2 molecule.

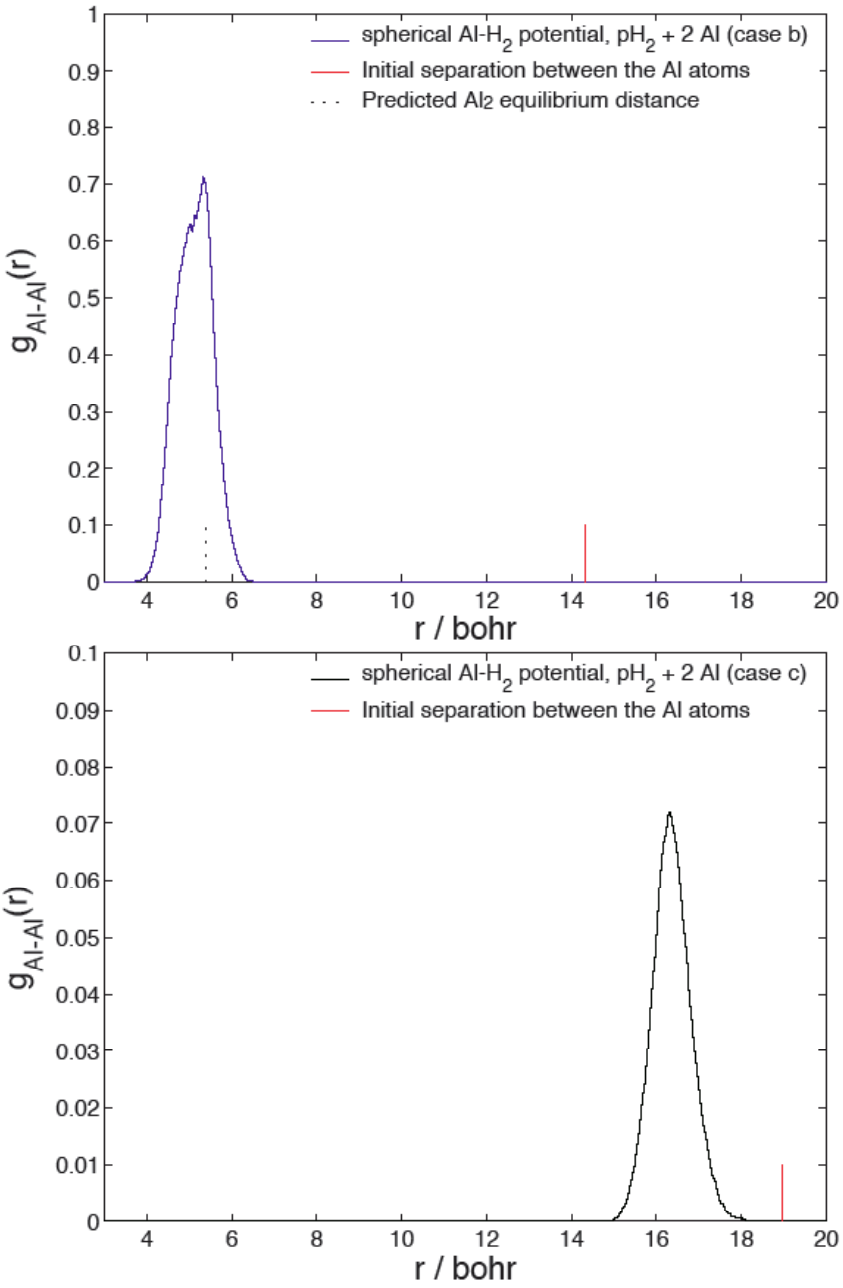

Fig 4.12 Al–Al pair correlation functions for two Al atoms site substituted in the solid. All Al-pH$_2$ interactions are assumed spherical, and the Al–Al interaction is assumed to be given by the ($^3\Pi_u$) potential. Upper panel: case (b) substitution in pH$_2$; Lower panel: case (c) substitution in pH$_2$. The vertical bars indicate the initial separation between the Al atoms. In the upper panel the vertical bar at r=5.39 bohr indicates the Al$_2$ equilibrium distance predicted by our *ab initio* calculations.

The lattice distortion is reflected in the Al–H_2 pair correlation function in Fig. 4.13. The presence of the Al atoms results in a displacement of the H_2 molecules that is more uniform than in when the anisotropic Al–H_2 potential is used. Especially in case (c), the pair-correlation function $g_{\mathrm{Al-H_2}}(r)$ is essentially identical to spherical Al–H_2 potential in Fig 4.4 for a single Al atom substitute in solid H_2, which indicates that each Al atom affects the Al–H_2 lattice structure separately before Al–Al combination happens.

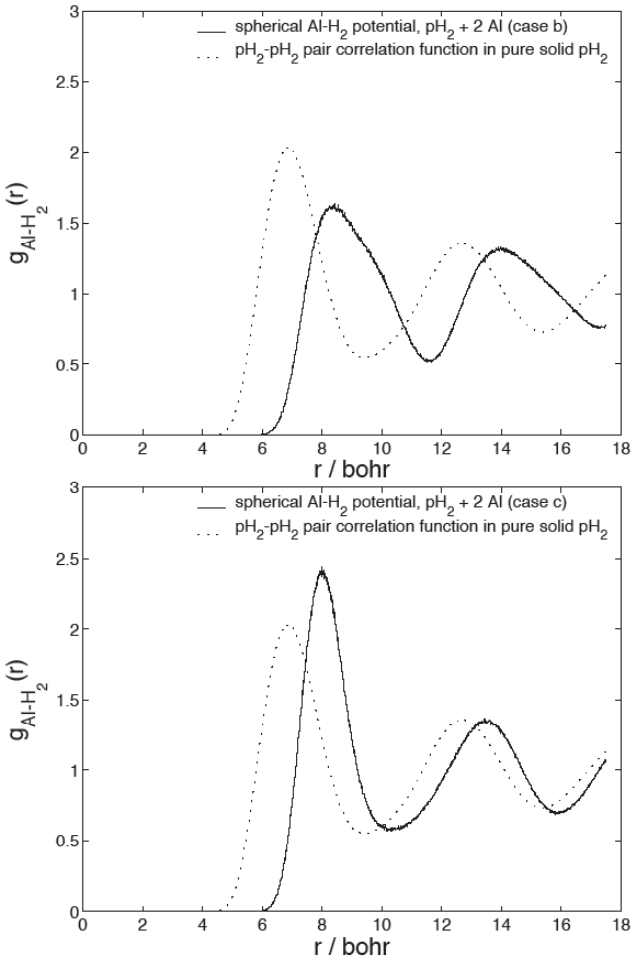

Fig 4.13 Al-pH$_2$ pair correlation functions for two Al atoms site substituted in the solid. All Al-pH$_2$ interactions are assumed spherical, and the Al–Al interaction is assumed to be given by the ($^3\Pi_u$) potential. Upper panel: case (b) substitution in pH$_2$; Lower panel: case (c) substitution in pH$_2$. For comparison purpose, the pair correlation function for pure solid pH$_2$ is also shown in each plot.

When the electronically asymmetric potentials are used, in case (b) the H_2 molecules in the same *xy* plane as the Al atoms stay close to their original positions before combination happens. In contrast, the positional projection in Fig 4.14 shows that even in case (c), all H_2 molecules are pushed outward. And there is also an overall translational motion of the lattice cage which accompanies the movement of the two Al towards each other. In case (b), the H_2 molecule originated between the two Al atoms is pushed dramatically to one side. The pushing is directed almost vertically to Al–Al connection line. The tension so produced on the lattice is reduced by positioning other H_2 molecules originated near the final position of this H_2 molecule away, as shown by the arrows in Fig 4.14(I). This drastic reorientation does not occur when the anisotropic Al–H_2 potential is used.

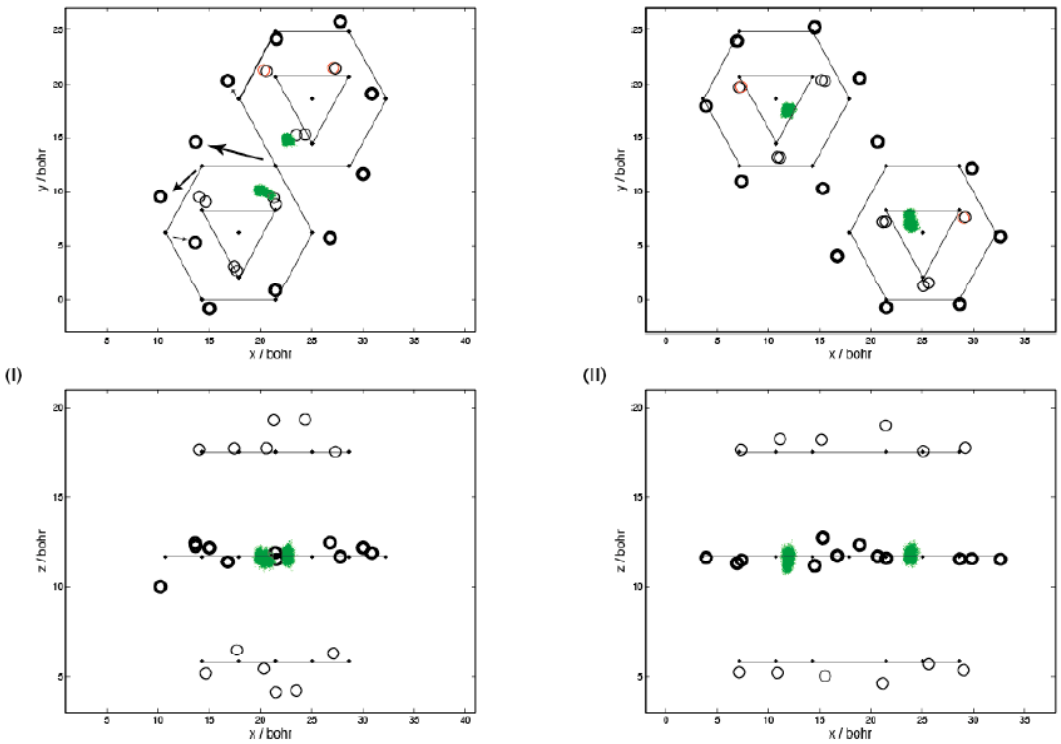

Fig 4.14 Positions of the nearest-neighbor $p\mathrm{H_2}$ molecules and the two central, site-substituted Al atoms described by 100 PIMC configurations, with dilution factor of 500 and p=48, projected onto the *xy* and *xz* planes. All Al-$p\mathrm{H_2}$ interactions are assumed spherical, and the Al–Al interaction is assumed to be given by the most attractive ($^3\Pi_u$) potential. The filled circles (•) indicate the positions of the hcp lattice sites. The open circles (o) designate the averaged positions of the $p\mathrm{H_2}$ molecules and the Al atoms. The positional spread of the Al atom is shown by the dotted points. To guide the eye, the hcp vertices lying in parallel *xz* planes are connected by straight lines. (I): 23 $\mathrm{H_2}$ + 2 Al (case (b) substitution), (II): 24 $\mathrm{H_2}$ + 2 Al (case (c) substitution).

Table 4.2 and 4.3 also present the results for the rms delocalizations and average energies. Again, the delocalization and average kinetic energy of the $\mathrm{H_2}$ molecules varies little. The average kinetic energy of the Al atoms in case (c) is close to that for one Al atom in solid $\mathrm{H_2}$ when the spherical Al–$\mathrm{H_2}$ potential is used, but that in case (b) is close to the computed average kinetic energy of case (a) determined with the anisotropic potential (Table 4.3). This is another confirmation that when recombination occurs, the motion of the two Al atoms is dominated by the $\mathrm{Al_2}$ molecule potential.

When the spherical Al–pH$_2$ potential is used, then, compared to pure solid pH$_2$ (p=48, Table 4.1), embedding of two Al atoms lowers the total static lattice energy by ~ 231 cm^{-1} per Al atom in case (c). This is consistent with the number in the case of a single embedded Al atom with Al–H$_2$ interaction described by the spherical potential, because each Al atom affects the lattice separately. The potential energy for case (b) is decreased by 11743 cm^{-1} compared to pure solid H$_2$, consistent with the energy released when two Al atoms combine.

Consequently, the electronic anisotropy of the Al atoms is one of the factors that helps stabilize a dispersion of Al atoms stable in solid pH$_2$ at distances of ~15 bohr. Without this anisotropy, recombination occurs for substitution distances < 15 bohr. For substitution distances longer than 18 bohr, however, the attraction between Al atoms is not strong enough to displace all the intervening hydrogens, irrespective of whether the open-shell nature of the Al atom is included.

4.3.5 Estimate of lifetime

Due to the deep attractive well of the Al dimer, the recombination of two embedded Al atoms will release a large amount of energy. Consequently, all the initial substitutional sites where our simulations do not lead to recombination correspond to metastable states. In these metastable states, recombination is statistically very improbable. To verify this, we ran case (b), (c) and (d) simulations for an additional 6 months, without observing any evidence of recombination. Eventually, if the simulation were continued long enough, the two atoms would combine. In this section we use transition state theory to estimate the lifetimes of these metastable states.

The energy profiles for case (b), (c) and (d) are obtained in the same way as for case (a) [Fig 4.11(II), (III), (IV)]. The reaction coordinate is chosen to be the distance between the two Al atoms. The solid curves correspond to calculations in

which Al atoms are constrained to move symmetrically along the line of separation with the $p\mathrm{H}_2$ molecules frozen at the hcp lattice sites. In each case the height of the calculated barrier is inserted into the standard transition state expression[101]

$$k = \frac{k_B T}{h} \exp\left(-E_a / k_B T\right) \frac{Q^{\neq}}{Q_r} \tag{4.2}$$

to estimate the rate constant for recombination. Here we assume that the partition function ratio of the transition state and the reactant is 1:1. The rate constants and the corresponding half lifetimes (ln2/K) are listed in Table 4.5.

Table 4.5 Estimated recombination lifetime

	$E_a(\mathrm{cm}^{-1})$	$K(\mathrm{s}^{-1})$	ln2/K
case (b)	107	1.46×10^{-6}	5.5 days
case (c)	103	5.98×10^{-6}	32 hours
case (d)	91	5.46×10^{-4}	1270 seconds

From this rough estimate, we see that the atomic level dispersion of two Al atoms as exemplified by the three cases we studied here, will be stable only for several minutes to several days. We also notice that initial substitutions in case (b), where a hydrogen molecule sits nominally midway between the two Al atoms, corresponds to the longest lifetime. In case (c), where two intervening molecules lie near the line connecting the Al atoms, the lifetime is in hours. In case (d), where the intervening hydrogen molecules lie farther away from the Al connection line, the lifetime is even shorter. As we might expect, the degree of metastability depends strongly on the initial relative arrangement of the particles.

4.4 Conclusion

In summary, then, we have used the PIMC method to study the structure and energetics of pure solid $p\mathrm{H}_2$ / $o\mathrm{D}_2$ and the effect of site-substitution doping by one or

two Al atoms. For pure solid $p\mathrm{H}_2$, we first monitored the convergence of the PIMC. We then showed that the $p\mathrm{H}_2$ molecules exhibit large quantum delocalization and kinetic energies much greater than k_BT, two distinct characteristics of a quantum solid.

Our results for a single Al atom in solid $p\mathrm{H}_2$ were essentially the same as those obtained earlier by Mirijanian *et al*. with PIMD methods.[16] With our new information on the particle positional spread and average energies, and by comparing with the pair correlation function for pure solid $p\mathrm{H}_2$, we predicted that the 3*p* electron density of Al is distributed primarily along a single axis. This lowers the static lattice energy, but is accompanied by some distortion of the lattice.

For two Al atoms embedded in solid $p\mathrm{H}_2$ / $o\mathrm{D}_2$, we studied four different substitution sites. For substitution sites within a distance of ~ 13 bohr, we found that the two Al atoms greatly distort the lattice structure to allow recombination into the Al_2 molecule. This releases a large amount of energy. This result is different from the model studies presented in a previous paper,[99] where the $p\mathrm{H}_2$ molecules were fixed in place. It is the quantum nature of the $p\mathrm{H}_2$ molecules that facilitates recombination of the Al atoms.

However, when the two Al atoms are embedded initially at distances longer than 14 bohr, the equilibrated separation between the two Al atoms is little changed from the initial substitutional sites. The interaction between the two Al atoms is small, and the Al atoms affect the system separately. This may impose an upper practical limit to the density of Al atoms which can be substituted before recombination occurs, which is ~ 6.67% mole percent Al to H_2. We estimate the lifetime of the embedded solids at T=4K to range from several minutes to several days

We investigated several factors that affect the stability of the dispersion. The initial relative position of the particles is the most important of these. Of those we

tested, the optimal arrangement is one in which the intervening H_2 molecules remain as close as possible to the vector seperating between the two Al atoms. The Al electronic anisotropy is another factor that helps stability. Stability is enhanced if the local H_2 arrangement impedes the two 3*p* orbitals in the Al atoms from adopting the arrangement which corresponds to the lowest electronic state of Al_2 molecule ($^3\Pi_u$).

Chapter 5: Overall Conclusions

Guided by the overall goal of studying many-body interactions involving open-shell particles, we have presented in this dissertation the investigation of atomic Al doped into two different low-temperature condensed media. We have chosen Monte-Carlo, path-integral simulations to determine the equilibrium properties of these multi-dimensional systems. This allows us to carry out quantum simulations at finite temperatures. To deal with the difficult problem of simulating Al doped in helium clusters at very low temperatures, we implemented out a multilevel extension of standard path-integral simulations

To describe one Al impurity atom doped in a cluster of spherical particles (He or $p\mathrm{H}_2$) we used the pairwise Hamiltonian model introduced first by Balling and Wright. To extend the study to more than one impurity atom, we used an extension of this idea to describe the interaction between two atoms, each in a ^2P electronic state, embedded in a cluster of spherical atoms. The model requires first accurate *ab initio* potential energy curves for the Al_2 system, for all the 36 electronic states which correlate with dissociation into two ground-state Al(^2P) atoms. Consequently, we use a valence-bond-like model to transform these 36 molecular orbital states into a set of 36 Cartesian ($q_a q_b$) states which correspond to assigning the two $3p$ electrons to Cartesian orbitals centered on either atom.

It is then easy to extend the Balling and Wright model to determine, in this 36 state basis, the matrix elements corresponding to the interaction of each ^2P atom with any number of surrounding spherical ligands. The lowest eigenvalue of the resulting 36×36 matrix defines, in an adiabatic approximation, the potential governing the motion of the atoms.

Our studies of Al in both liquid helium and solid *para*–hydrogen indicate that the impurity atoms strongly disturb the structure of the doped media. The electronic anisotropy of the Al atom plays an important role in both this structural change as well as in the energetics. We applied our potential model for two Al atoms embedded in solid $p\mathrm{H}_2$ to study the stability of the system with respect to recombination. We also investigated the effect on these solvated open-shell particles of spin-orbit coupling, electronic anisotropy. The detailed results and discussion are found in the four chapters of this dissertation.

Both the potential model we built and the specific simulations we performed on Al in helium and Al in hydrogen, have potential applications beyond the scope of this dissertation. The potential models could be adapted without modification to the interaction of other ^2P atoms in either $p\mathrm{H}_2$ or other spherical environments (Ar, He). In addition, the models could be extended, in a straightforward manner, to the interaction of atoms in other open-shell electronic states, or, to the interaction of two atoms in different electronic states.

For example, for the interaction of a ^2P atom (*e.g.*, the Al ground state) and a ^2D atom (*e.g.*, the Al 3*d* state or a transition metal atom in its ground electronic state) both embedded in an ensemble of spherical atoms, application of the pairwise Hamiltonian model is summarized schematically as

$$\begin{aligned}&\text{Total potential} = \\ &\text{lowest eigenvalue of } 60 \times 60 \text{ matrix} \left\{ \begin{array}{l} \text{the } {}^2P - {}^2D \text{ interaction matrix} \\ + \text{ matrix of the spin-orbit Hamiltonian} \\ + {}^2P \text{ atom}/{}^2D \text{ atom - matrix of interaction with spherical ligands} \end{array} \right\} \\ &+ \text{ scalar pair-wise interaction potential between all spherical ligands}\end{aligned} \tag{5.1}$$

Here the matrix of the spin-orbit Hamiltonian can be obtained from Eq. (3.9), and the matrix of interaction between a ^2P atom (or a ^2D atom) with the spherical ligands matrix can be obtained from Eq. (3.15). The difference from the application to two

Al atoms is that now the electronic-spin-orbit states of atoms a and atom b have dimensions 6 and 10, respectively. For the $^2P - {}^2D$ interaction matrix, we first need potential energy curves for the 60 distinct electronic states (some degenerate) which correlate with an atom in a ^2P state and an atom in a ^2D state. Then we need to develop a suitable valence bond description of each state in terms of a product of Cartesian-like functions $p_{q_a} d_{q_b}$

Likewise, this model could possibly be extended to more than two atoms in open-shell electronic states. Following Eq. (5.1), we can develop, straightforwardly, the matrices of the spin-orbit Hamiltonian and the interaction between each atom and the spherical ligands. For example, for three Al atoms (a, b, c), we can write

$$\begin{aligned}\langle q_a' q_b' q_c' | V_i | q_a q_b q_c \rangle = & \delta_{q_a' q_a} \delta_{q_b' q_b} \left(\mathrm{V}_6\right)_{q_c' q_c} \\ & + \delta_{q_a' q_a} \delta_{q_c' q_c} \left(\mathrm{V}_6\right)_{q_b' q_b} + \delta_{q_c' q_c} \delta_{q_b' q_b} \left(\mathrm{V}_6\right)_{q_a' q_a}\end{aligned} \tag{5.2}$$

However, it will be an extensive computational effort to calculate *ab initio* potential energy surfaces for the 216 states of Al_3, and to decompose these into a Cartesian $q_a q_b q_c$ valence bond description. The effort will be even greater to extend this model to n>3.

Since it is relatively easy to obtain the binary potentials, one might wonder whether we could apply the ideas behind Eqs. (3.9) and (3.15) to determine interactions involving more than two Al atoms, Namely,

$$\begin{aligned}\langle q_a' q_b' q_c' | V_{tri} | q_a q_b q_c \rangle = & \delta_{q_c' q_c} \left(\mathrm{V}_{di}\right)_{q_a q_b q_a' q_b'} \\ & + \delta_{q_b' q_b} \left(\mathrm{V}_{di}\right)_{q_a q_c q_a' q_c'} + \delta_{q_a' q_a} \left(\mathrm{V}_{di}\right)_{q_b q_c q_b' q_c'}\end{aligned} \tag{5.3}$$

As discussed in Chapter 3, all the valence-bond-like models we have introduced neglect the overlap between the atomic orbitals. This is certainly justified at large distances, but will fail in providing a decent description of the atomic interactions in the limit when they are close. Some questions for future studies are: How much does this zero-overlap description deviate from the true *ab initio* potential energy curves? At what atomic separations does it become reliable?

Impurity-doped helium nanodroplets continues to be a hot area of experimental investigation.[3-8,11,51] While many theoretical calculations have paid attention to the rotational motion of impurity molecules in helium,[19,47,105] there is a lack of theoretically predicted spectrum to compare with experimental results.[106] Two challenges are the accurate description of the interaction between the particles, especially for non-spherically-symmetric dopants, and the search for an efficient simulation method for the very quantum helium system. Certainly, future work should be devoted to the development of simulation methods which are more efficient than the PIMC techniques we used here to simulate the electronic excitation spectrum of Al in helium. We anticipate that continuing experimental studies of the spectra of atoms and molecules doped into cryogenic helium clusters (*e.g.*, Li, Na, K, Rb, Cs, Ag, Al, Eu, Mg and their dimer and clusters, organic molecules as glyoxal, polyaromatics, indoles and porphyrins)[3,11,106] will continue to provide a challenge for theoreticians.

Recently, Mella and co-workers have published quantum diffusion Monte-Carlo method (QMC) investigations of the Mg atoms in He clusters.[107] Unfortunately, as opposed to a path-integral simulation, in any QMC investigation the temperature is rigorously zero. Also, Mella and co-workers did not take into account the bosonic symmetry of helium. A challenge facing future applications of PIMC methods is how to go beyond the primitive approximation for the helium-impurity interaction (which is generally not isotropic) in an efficient simulation including the bosonic symmetry? One very promising approach is based on expanding the helium-impurity interaction in spherical terms and then using pair-product forms.[47] However, this expansion, at least as it has been applied up to now, does not retain the same level of accuracy as our potential model.

Our, and similar, studies of the stability against recombination of Al atoms dispersed in solid hydrogen will provide an upper bound to the maximum achievable

concentration of these atoms. This could have significant implications toward the potential use of doped H_2 as a rocket propellant. Although there exists some experimental information that one can achieve an Al concentration of above 10% in hydrogen,[108] based on our simulations, we suspect that at these concentrations the Al is present as diatomic molecules, or small polymers, rather than as a dispersed atomic solute.

Solid pH_2 is a very flexible quantum lattice.[72] It can easily absorb the strain induced by embedded Al impurities by distortion or expansion. In Chapter 4 above we have assumed a constant volume canonical ensemble, and we observe large distortions in the lattice structure. It would be interesting to see how the solid behaves under constant pressure conditions when the volume is allowed to change. To examine this effect, one would need to carry out a constant pressure PIMC simulation. In general, the isothermal-isobaric partition function can be written as[24,31]

$$Q_{NPT} = \int dV \exp\left(-\beta P_{\text{ext}} V\right) Q_{NVT} \propto \iint dV d\mathbf{q} \exp\left[-\beta\left(P_{\text{ext}} V + V_{eff}\right)\right], \quad (5.4)$$

where Q_{NVT} is the canonical partition function we discussed earlier in Eq. (1.16). It is sometimes an advantage to use scaled coordinates in constant pressure PIMC simulations. An expression for the partition function written in scaled coordinates for PIMC simulations is given in Ref. 94. With our potential model, it would be more straightforward to use Eq. (5.4).

One important difference between this ensemble and the canonical ensemble is that the Monte-Carlo moves involve changes in volume (so that the density fluctuates). In general, changing the volume is computationally more expensive since all the potentials need to be recalculated. It takes considerably more computer time to get well converged results in a constant pressure simulation. We did some exploratory investigations of constant pressure PIMC simulations (not included in this thesis).

These showed that the flexibility of solid *para* hydrogen is an additional factor that reduces the stability of Al atoms dispersed at the atomic level. Where, in the constant volume simulations, a barrier to recombination of two Al atoms occurs, as the constant volume restriction is relaxed, the solid *para* hydrogen can expand or shrink to allow the two Al atoms to move toward each other, and thereby combine, with a consequent significant lowering of the total energy.

In summary, we hope that our work will provide some insight into the complex role that electronic anisotropy plays in many-body systems, and help in developing an understanding of how to deal with weakly-interacting, open-shell systems in the condensed phase.

Appendix 2.I Matrix elements of $\mathbf{D}(\theta)$ and $\mathbf{H}_{so}$

$\mathbf{D}(\theta)$ = (2.1.1)

$$\begin{pmatrix} \cos^4\left(\frac{\theta}{2}\right) & \frac{1}{2}\sin\theta(1+\cos\theta) & \sqrt{\frac{3}{8}}\sin^2\theta & -\frac{1}{2}\sin\theta(\cos\theta-1) & \sin^4\left(\frac{\theta}{2}\right) \\ -\frac{1}{2}\sin\theta(1+\cos\theta) & \frac{1}{2}(2\cos\theta-1)(\cos\theta+1) & \sqrt{\frac{3}{2}}\sin\theta\cos\theta & \frac{1}{2}(2\cos\theta+1)(1-\cos\theta) & -\frac{1}{2}\sin\theta(\cos\theta-1) \\ \sqrt{\frac{3}{8}}\sin^2\theta & -\sqrt{\frac{3}{2}}\sin\theta\cos\theta & \frac{1}{2}\left(3\cos^2\theta-1\right) & \sqrt{\frac{3}{2}}\sin\theta\cos\theta & \sqrt{\frac{3}{8}}\sin^2\theta \\ \frac{1}{2}\sin\theta(\cos\theta-1) & \frac{1}{2}(2\cos\theta+1)(1-\cos\theta) & -\sqrt{\frac{3}{2}}\sin\theta\cos\theta & \frac{1}{2}(2\cos\theta-1)(\cos\theta+1) & \frac{1}{2}\sin\theta(1+\cos\theta) \\ \sin^4\left(\frac{\theta}{2}\right) & \frac{1}{2}\sin\theta(\cos\theta-1) & \sqrt{\frac{3}{8}}\sin^2\theta & -\frac{1}{2}\sin\theta(1+\cos\theta) & \cos^4\left(\frac{\theta}{2}\right) \end{pmatrix}$$

$\mathbf{H}_{so}$ = (2.1.2)

$\frac{1}{2}a\times$

	$d_{x^2-y^2}$	d_{xy}	d_{zx}	d_{yz}	d_{z^2}	$\overline{d_{x^2-y^2}}$	$\overline{d_{xy}}$	$\overline{d_{zx}}$	$\overline{d_{yz}}$	$\overline{d_{z^2}}$
$d_{x^2-y^2}$	0	$-2i$	0	0	0	0	0	-1	$-i$	0
d_{xy}	$2i$	0	0	0	0	0	0	i	-1	0
d_{zx}	0	0	0	$-i$	0	1	$-i$	0	0	$-\sqrt{3}$
d_{yz}	0	0	1	0	0	i	1	0	0	$\sqrt{3}i$
d_{z^2}	0	0	0	0	0	0	0	$\sqrt{3}$	$-\sqrt{3}i$	0
$\overline{d_{x^2-y^2}}$	0	0	1	-1	0	0	$2i$	0	0	0
$\overline{d_{xy}}$	0	0	i	1	0	$-2i$	0	0	0	0
$\overline{d_{zx}}$	-1	$-i$	0	0	$\sqrt{3}$	0	0	0	i	0
$\overline{d_{yz}}$	i	-1	0	0	$\sqrt{3}i$	0	0	$-i$	0	0
$\overline{d_{z^2}}$	0	0	$-\sqrt{3}$	$-\sqrt{3}i$	0	0	0	0	0	0

where spin-orbit constant a=0.54 cm^{-1} for Al (^2D).

Appendix 2.II Staging

Staging is another path-integral sampling technique that improves the efficiency of the simulation by making collective movements of the pseudoparticles.[26,109-111] It involves a change of integration variables, which serves to uncouple the harmonic term, and a corresponding reformulation of the effective Hamiltonian. It rigorously generates a canonical phase space distribution. To use the Levy construction in our multilevel sampling, we need to prove that the Levy construction exactly samples the free particle density matrix. Since the Levy construction is equivalent to one special case of staging, here we outline the staging method with the aim of justifying the use of the Levy construction in our multilevel sampling.

For simplicity, we only deal with a single particle in one dimension in this Appendix. It is straightforward to extend the discussion to our case of multiple particles, not necessarily of the same type, moving in three dimensions.

For a single particle not subject to an external field (*i.e.*, a free particle, V=0), we rewrite the density matrix in Eq. (1.13) as

$$\rho_0(x_i, x_{i+1};\tau)=\langle x_i \mid e^{-\tau \mathrm{T}} \mid x_{i+1}\rangle = \left(\frac{m}{2\pi\tau\hbar^2}\right)^{1/2} \exp\left(-\frac{m}{2\tau\hbar^2} \mid x_i - x_{i+1} \mid^2\right) \quad (2.2.1)$$

where T is the kinetic energy operator and τ is β/p. Then, the path-integral quadrature in Eq. (1.14) can be written as

$$Q = \int dx_1 dx_2 ... dx_p \rho_0(x_1, x_2;\tau) ... \rho_0(x_p, x_{p+1};\tau) \quad (2.2.2)$$

where $x_{p+1}=x_1$.

Let us divide the polymer chain of p particles into segments of length j ($nj=p$, n is an integer). We shall focus on with one segment which starts at $y_0 = x_{sj+1}$, and ends at $y_j = x_{sj+j+1}$ (s is an integer $<n$). We have

$$\cdots \rho_0(x_{sj}, x_{sj+1};\tau)\ \{\rho_0(x_{sj+1}, x_{sj+2};\tau)\ \cdots \rho_0(x_{sj+j}, x_{sj+j+1};\tau)\}\ \rho_0(x_{sj+j+1}, x_{sj+j+2};\tau)\ \cdots$$
$$\downarrow \quad \downarrow \qquad\qquad \downarrow \quad \downarrow$$
$$y_0 \quad y_1 \qquad\qquad y_{j\text{-}1} \quad y_j \qquad `$$

$$\begin{aligned}&\rho_0(y_0, y_1;\tau)\ \cdots \rho_0(y_{j\text{-}1}, y_j;\tau) = \\ &\frac{\rho_0(y_0,\ y_1;\tau)\rho_0(y_1,\ y_2;\tau)}{\rho_0(y_0,\ y_2;2\tau)} \cdot \frac{\rho_0(y_2,\ y_3;\tau)\rho_0(y_0,\ y_2;2\tau)}{\rho_0(y_0,\ y_3;3\tau)} \\ &\cdots \frac{\rho_0(y_{j-1},\ y_j;\tau)\rho_0(y_0,\ y_{j-1};(j-1)\tau)}{\rho_0(y_0,\ y_j;j\tau)} \cdot \rho_0(y_0,\ y_j;j\tau)\end{aligned} \tag{2.2.3}$$

Each fraction term on the right hand side of the above equation can be written in a common form:

$$\begin{aligned}&\frac{\rho_0(y_{i-1},\ y_i;\tau)\rho_0(y_0,\ y_{i-1};(i-1)\tau)}{\rho_0(y_0,\ y_i;i\tau)} \\ &= \left(\frac{1}{2\pi\tau\hbar^2}\cdot\frac{mi}{i-1}\right)^{1/2} \exp\left[-\frac{m}{2\tau\hbar^2}\left(|\, y_{i-1}-y_i\,|^2 + \frac{1}{i-1}|\, y_0-y_{i-1}\,|^2 - \frac{1}{i}|\, y_0-y_i\,|^2\right)\right] \\ &= \left(\frac{1}{2\pi\tau\hbar^2}\cdot\frac{mi}{i-1}\right)^{1/2} \exp\left\{-\frac{1}{2\tau\hbar^2}\cdot\frac{mi}{i-1}\left[{y_{i-1}}^2 - 2y_{i-1}\frac{y_0+(i-1)y_i}{i} + \left(\frac{y_0+(i-1)y_i}{i}\right)^2\right]\right\}\end{aligned} \tag{2.2.4}$$

If we define new variables

$$m_i = \frac{mi}{i-1}, y_{i-1}{}^* = \frac{y_0+(i-1)y_i}{i} \ (\text{so that } x_{sj+i}{}^* = \frac{x_{sj+1}+(i-1)x_{sj+i+1}}{i}) \tag{2.2.5}$$

(2.2.4) is written as

$$\frac{\rho_0(y_{i-1},\ y_i;\tau)\rho_0(y_0,\ y_{i-1};(i-1)\tau)}{\rho_0(y_0,\ y_i;i\tau)} = \left(\frac{m_i}{2\pi\tau\hbar^2}\right)^{1/2} \exp\left\{-\frac{m_i}{2\tau\hbar^2}\left[y_{i-1}-y_{i-1}{}^*\right]^2\right\} \tag{2.2.6}$$

Putting all together one arrives the following

$$\begin{aligned}&\rho_0(y_0, y_1;\tau)\ \cdots \rho_0(y_{j\text{-}1}, y_j;\tau) = \\ &\left(\frac{m}{2\pi j\tau\hbar^2}\right)^{1/2} \exp\left[-\frac{m}{2j\tau\hbar^2}\left(y_0-y_j\right)^2\right] \times \prod_{i=2}^{j}\left(\frac{m_i}{2\pi\tau\hbar^2}\right)^{1/2} \exp\left[-\frac{m_i}{2\tau\hbar^2}\left(y_{i-1}-y_{i-1}{}^*\right)^2\right]\end{aligned} \tag{2.2.7}$$

and

$$Q=\left(\frac{m}{2\pi j\tau\hbar^2}\right)^{n/2}\prod_{i=2}^{j}\left(\frac{m_i}{2\pi\tau\hbar^2}\right)^{n/2}\int dx_1dx_2...dx_p\bullet$$
$$\exp\left[-\sum_{s=0}^{n-1}\frac{m}{2j\tau\hbar^2}\left(x_{sj+1}-x_{sj+j+1}\right)^2-\sum_{s=0}^{n-1}\sum_{i=2}^{j}\frac{m_i}{2\tau\hbar^2}\left(x_{sj+i}-x_{sj+i}*\right)^2\right] \tag{2.2.8}$$

By use of the new staging variables we have obtained a system of uncoupled springs. Consequently, we can sample the coordinates directly from a Gaussian distribution. This allows us to perform collective uncorrelated movements of the particles.

The algorithm is applied as following: First, we select a segment of the chain and fix the two ends: $y_0 = x_{sj+1}$ and $y_j = x_{sj+j+1}$. The movements correspond to the intervening $j-1$ particles. The sampling is performed iteratively since as the index i decreases, all the y* depend on the preceding y.

1. $i = j$

$$m_j=\frac{mj}{j-1}, y_{j-1}*=\frac{y_0+(j-1)y_j}{j} \tag{2.2.9}$$

$$y_{j-1}'=y_{j-1}*+\eta\sqrt{\frac{\hbar^2\tau}{m_j}} \tag{2.2.10}$$

where η is a normally distributed random number with zero mean and unit variance.

2. $i = j-1$

$$m_{j-1}=\frac{m(j-1)}{j-2}, y_{j-2}*=\frac{y_0+(j-2)y_{j-1}}{j-1} \tag{2.2.11}$$

$$y_{j-2}'=y_{j-2}*+\eta\sqrt{\frac{\hbar^2\tau}{m_{j-1}}} \tag{2.2.12}$$

……

$j-1$. $i = 2$

$$m_2=2m, y_1*=\frac{y_0+y_2}{2} \tag{2.2.13}$$

$$y_1'=y_1*+\eta\sqrt{\frac{\hbar^2\tau}{m_2}} \tag{2.2.14}$$

In a full application of the staging algorithm, the above procedure is repeated all over the n segments of the chain. Also the Cartesian coordinate labels are reassigned by rotating the coordinate labels around the cyclic chain ($x_i \rightarrow x_{i+r}$, when $i \leq p\text{-}r$; $x_i \rightarrow x_{i+r-p}$, when $i > p\text{-}r$, r is some integer number). Note that the integral is invariant under a cyclic relabeling of the coordinates. This reassignment insures that no single point remains fixed permanently.

Note that the above procedure samples free particles (*i.e.*, kinetic terms only) exactly. With an external potential, there is an extra term in the partition function $\exp\left[-\frac{\beta}{p}\sum_{k=1}^{p} V(x_k)\right]$. Consequently, the standard Metropolis acceptance-rejection algorithm is invoked at each trial position. The rejection criterion is based only on the potential part of the exponent, since the kinetic part is sampled exactly by the staging algorithm.

Now we go back to the Levy construction. We observe that for $j=2$ Eq. (2.2.10) becomes

$$y_1' = \frac{y_0 + y_2}{2} + \eta\sqrt{\frac{\hbar^2\tau}{2m}} \tag{2.2.15}$$

which is indeed the Levy construction. With the staging coordinates the free particle density matrix is sampled exactly. Therefore, the Levy construction also samples the free particle density matrix exactly.

Appendix 3.I Matrix elements of H_{el}

For the $q_a q_b$ states with $M_S = 1$, the matrix of H_{el} blocks as follows, where we use a compact notation in which the energy of each diabatic molecular orbital state is designated by its state label

	$x_a x_b$	$y_a y_b$	$z_a z_b$
$x_a x_b$	$\frac{1}{2}\,{}^3\Delta + \frac{1}{6}\,1^3\Sigma_u + \frac{1}{3}\,2^3\Sigma_u + \frac{1}{\sqrt{3}}\,{}^3V_{12}$	$-\frac{1}{2}\,{}^3\Delta + \frac{1}{6}\,1^3\Sigma_u + \frac{1}{3}\,2^3\Sigma_u$	$\frac{1}{3}\,2^3\Sigma_u - \frac{1}{3}\,1^3\Sigma_u - \frac{1}{\sqrt{3}}\,{}^3V_{12}$
$y_a y_b$	s	$\frac{1}{2}\,{}^3\Delta + \frac{1}{6}\,1^3\Sigma_u + \frac{1}{3}\,2^3\Sigma_u - \frac{1}{\sqrt{3}}\,{}^3V_{12}$	$\frac{1}{3}\,2^3\Sigma_u - \frac{1}{3}\,1^3\Sigma_u + \frac{1}{\sqrt{3}}\,{}^3V_{12}$
$z_a z_b$	s	s	$\frac{2}{3}\,1^3\Sigma_u + \frac{1}{3}\,2^3\Sigma_u$

(3.1.1)

	$x_a y_b$	$x_b y_a$
$x_a y_b$	$\frac{1}{2}\,({}^3\Sigma_g + {}^3\Delta)$	$\frac{1}{2}\,({}^3\Sigma_g - {}^3\Delta)$
$y_a x_b$	s	$\frac{1}{2}\,({}^3\Sigma_g + {}^3\Delta)$

(3.1.2)

	$x_a z_b$	$x_b z_a$
$x_a z_b$	$\frac{1}{2}\,({}^3\Pi_g + {}^3\Pi_u)$	$\frac{1}{2}\,({}^3\Pi_g - {}^3\Pi_u)$
$z_a x_b$	s	$\frac{1}{2}\,({}^3\Pi_g + {}^3\Pi_u)$

(3.1.3)

The matrix of H_{el} in the space of the $y_a z_b$ and $y_b z_a$ states is identical to Eq. (3.1.3).

For the $q_a q_b$ states with $M_S = 0$, the matrix of H_{el} blocks as follows:

	$x_a \bar{y}_b$	$\bar{x}_a y_b$	$x_b \bar{y}_a$	$\bar{x}_b y_a$
$x_a \bar{y}_b$	$\frac{1}{4}\,[{}^1\Sigma_u + {}^3\Sigma_g + {}^1\Delta + {}^3\Delta]$	$\frac{1}{4}\,[-{}^1\Sigma_u + {}^3\Sigma_g - {}^1\Delta + {}^3\Delta]$	$\frac{1}{4}\,[-{}^1\Sigma_u + {}^3\Sigma_g + {}^1\Delta - {}^3\Delta]$	$\frac{1}{4}\,[{}^1\Sigma_u + {}^3\Sigma_g - {}^1\Delta - {}^3\Delta]$
$\bar{x}_a y_b$	s	identical to (1,1)	identical to (1,4)	identical to (1,3)

(3.1.4)

$x_b\bar{y}_a$	s	s	identical to (1,1)	identical to (1,2)
$\bar{x}_b y_a$	s	s	s	identical to (1,1)

	$x_a\bar{x}_b$	$\bar{x}_a x_b$	$y_a\bar{y}_b$	$\bar{y}_a y_b$	$z_a\bar{z}_b$	$\bar{z}_a z_b$
$x_a\bar{x}_b$	$\frac{1}{12}$ [3($^1\Delta$+ $^3\Delta$) +2(2$^1\Sigma_g$+ 2$^3\Sigma_u$) +1$^1\Sigma_g$+ 1$^3\Sigma_u$ +2$^{3/2}$(^{1}V$_{12}$+ ^{3}V$_{12}$)]	$\frac{1}{12}$ [3(–$^1\Delta$+ $^3\Delta$) +2(–2$^1\Sigma_g$+ 2$^3\Sigma_u$) –1$^1\Sigma_g$+1$^3\Sigma_u$ +2$^{3/2}$(–^{1}V$_{12}$ +^{3}V$_{12}$)]	$\frac{1}{12}$ [–3($^1\Delta$+ $^3\Delta$) +2(2$^1\Sigma_g$+ 2$^3\Sigma_u$) +1$^1\Sigma_g$+ 1$^3\Sigma_u$ +2$^{3/2}$(^{1}V$_{12}$+ ^{3}V$_{12}$)]	$\frac{1}{12}$ [3($^1\Delta$– $^3\Delta$) +2(–2$^1\Sigma_g$+ 2$^3\Sigma_u$) –1$^1\Sigma_g$+1$^3\Sigma_u$ +2$^{3/2}$(–^{1}V$_{12}$ +^{3}V$_{12}$)]	$\frac{1}{6}$ [–1$^1\Sigma_g$– 1$^3\Sigma_u$ +2$^1\Sigma_g$+ 2$^3\Sigma_u$– 2$^{-1/2}$(^{1}V$_{12}$+ ^{3}V$_{12}$)]	$\frac{1}{6}$ [1$^1\Sigma_g$– 1$^3\Sigma_u$ –2$^1\Sigma_g$+2$^3\Sigma_u$ + 2$^{-1/2}$(^{1}V$_{12}$– ^{3}V$_{12}$)]
$\bar{x}_a x_b$	s	identical to (1,1)	identical to (1,4)	identical to (1,3)	identical to (1,6)	identical to (1,5)
$y_a\bar{y}_b$	s	s	identical to (1,1)	identical to (1,2)	identical to (1,5)	identical to (1,6)
$\bar{y}_a y_b$	s	s	s	identical to (1,1)	identical to (1,6)	identical to (1,5)
$z_a\bar{z}_b$	s	s	s	s	$\frac{1}{6}$ [2(1$^1\Sigma_g$+ 1$^3\Sigma_u$) +2$^1\Sigma_g$+ 2$^3\Sigma_u$– 2$^{3/2}$(^{1}V$_{12}$+ ^{3}V$_{12}$)]	$\frac{1}{6}$ [2(–1$^1\Sigma_g$ +1$^3\Sigma_u$) –2$^1\Sigma_g$+2$^3\Sigma_u$ +2$^{3/2}$(^{1}V$_{12}$– ^{3}V$_{12}$)]
$\bar{z}_a z_b$	s	s	s	s	s	identical to (5,5)

(3.1.5)

and,

	$x_a\bar{z}_b$	$\bar{x}_a z_b$	$x_b\bar{z}_a$	$\bar{x}_b z_a$
$x_a\bar{z}_b$	$\frac{1}{4}[{}^1\Pi_g+{}^1\Pi_u+{}^3\Pi_g+{}^3\Pi_u]$	$\frac{1}{4}[-{}^1\Pi_g-{}^1\Pi_u+{}^3\Pi_g+{}^3\Pi_u]$	$\frac{1}{4}[{}^1\Pi_g-{}^1\Pi_u+{}^3\Pi_g-{}^3\Pi_u]$	$\frac{1}{4}[-{}^1\Pi_g+{}^1\Pi_u+{}^3\Pi_g-{}^3\Pi_u]$
$\bar{x}_a z_b$	s	identical to (1,1)	identical to (1,4)	identical to (1,3)
$x_b\bar{z}_a$	s	s	identical to (1,1)	identical to (1,2)
$\bar{x}_b z_a$	s	s	s	identical to (1,1)

(3.1.6)

The matrix of H_{el} in the space of the $y_a\bar{z}_b$, $\bar{y}_a z_b$, $y_b\bar{z}_a$, $\bar{y}_b z_a$ states is identical to Eq. (3.1.6).

Appendix 3.II Frame transformation and force calculations

In a Cartesian space frame, we assume that the two Al atoms (Al_a and Al_b) are at positions $\{x_a,y_a,z_a\}$ and $\{x_b,y_b,z_b\}$ while the i^{th} pH_2 is at $\{x_i,y_i,z_i\}$. We wish to transform into a body frame defined so that the positions of the two Al atoms in this body frame are: {0,0,0} and {0, 0, R}. This transformation can be achieved by first shifting the origin to the first Al atom, followed by two consecutive rotations around the shifted x and y axes.

The coordinates of the i^{th} pH_2 in the body frame (designated by tildes) are:

$$\begin{pmatrix} \tilde{x}_i \\ \tilde{y}_i \\ \tilde{z}_i \end{pmatrix} = \mathbf{T} \begin{pmatrix} x_i \\ y_i \\ z_i \end{pmatrix} \tag{3.1.7}$$

where the SF→BF transformation matrix is

$$\mathbf{T} = \frac{1}{\rho R} \begin{pmatrix} \rho^2 & -(x_b - x_a)(y_b - y_a) & -(x_b - x_a)(z_b - z_a) \\ 0 & (z_b - z_a)R & -(y_b - y_a)R \\ (x_b - x_a)\rho & (y_b - y_a)\rho & (z_b - z_a)\rho \end{pmatrix} \tag{3.1.8}$$

$\rho = \left[(y_b - y_a)^2 + (z_b - z_a)^2\right]^{1/2}$ and the subscript indices a and b refer to the coordinates of the two Al atoms.

The derivatives of the potential with respect to the 6 coordinates which define the position of the two Al atoms are obtained by numerical differentiation of the lowest eigenvalue of the 36×36 potential matrix $\mathbf{V}(\mathbf{q})$. The derivatives with respect to any of the 3 coordinates which define the positions of the i^{th} pH_2 ligand, q_k , where $q_{k=1} \equiv x_i$, $q_{k=2} \equiv y_i$ and $q_{k=3} \equiv z$, are determined using the Hellman-Feynman theorem, namely

$$d\mathbf{V}/dq_k = \mathbf{C}^T\left[d\mathbf{V}/dq_k\right]\mathbf{C} + dV_{H_2-H_2}/dq_k \tag{3.1.9}$$

where **C** is the column eigenvector of the lowest eigenvalue of the potential matrix **V** and $V_{H_2-H_2}$ denotes the sum of the scalar H_2 pair potentials between the i^{th} and all the other pH_2 ligands. As discussed in the text surrounding Eq. (3.15), the dependence of the **V** matrix on the position of the i^{th} pH_2 ligand is constructed from elements of the 6×6 block diagonal matrix defined by Eq. (3.13), and which we designate $\mathbf{V}_6$.

The matrix elements of the derivatives of **V** which appear in Eq. (3.1.9) can be obtained identically to Eq. (3.15), namely

$$\left\langle q_a' q_b' \left| \frac{dV_i}{dq_k} \right| q_a q_b \right\rangle = \delta_{q_a' q_a}\left(d\mathbf{V}_6/dq_k\right)_{q_b' q_b} + \delta_{q_b' q_b}\left(d\mathbf{V}_6/dq_k\right)_{q_a' q_a} \tag{3.1.10}$$

We recall that the two terms in Eq. (3.1.10) correspond to the interaction between the i^{th} pH_2 ligand and the first and second Al atom, respectively. Because $\mathbf{V}_6$ is a symmetric, block diagonal matrix built of two identical 3×3 matrices **V** [Eq. (3.13)], determination of the matrix derivative $d\mathbf{V}_6/dq_k$ involves differentiation of the two 3 × 3 matrices which represent the interaction of the i^{th} pH_2 with the first and second Al atom, respectively. The differentiation can be done either analytically or numerically; we found both to be equally efficient. The analytical form of the derivative of the 3 × 3 potential between the i^{th} pH_2 and the first Al atom (which defines the origin of the body frame coordinate system), which corresponds to the first term in Eq. (3.1.10) , can be written as:

$$\frac{d\mathbf{V}}{dq_k} = \left\{ \frac{1}{r^2}\left[\frac{dV_\Sigma}{dr} - \frac{dV_\Pi}{dr} - \frac{2}{r}(V_\Sigma - V_\Pi) \right]\mathbf{Q} + \frac{dV_\Pi}{dr}\mathbf{1} \right\} \frac{q_k - q_a}{r} + \frac{1}{r^2}(V_\Sigma - V_\Pi)\mathbf{D} \tag{3.1.11}$$

Here the V_Σ and V_Π potentials and their derivatives are evaluated at $r = r_{ai}$, the distance between the first Al atom and the i^{th} $p\mathrm{H}_2$. The symmetric matrix **Q** is the Cartesian matrix from Eq. (3.12), with the coordinates of the i^{th} $p\mathrm{H}_2$ in the body frame, namely

$$\mathbf{Q} = \begin{pmatrix} \tilde{x}_i^2 & \tilde{x}_i\tilde{y}_i & \tilde{x}_i\tilde{z}_i \\ \tilde{x}_i\tilde{y}_i & \tilde{y}_i^2 & \tilde{y}_i\tilde{z}_i \\ \tilde{x}_i\tilde{z}_i & \tilde{y}_i\tilde{z}_i & \tilde{z}_i^2 \end{pmatrix} \tag{3.1.12}$$

The symmetric matrix **D** in Eq. (3.1.11) is given by

$$\mathbf{D} = \begin{pmatrix} 2T_{1k}\tilde{x}_k & T_{2k}\tilde{x}_k + T_{1k}\tilde{y}_k & T_{3k}\tilde{x}_k + T_{1k}\tilde{z}_k \\ s & 2T_{2k}\tilde{y}_k & T_{3k}\tilde{y}_k + T_{2k}\tilde{z}_k \\ s & s & 2T_{3k}\tilde{z}_k \end{pmatrix} \tag{3.1.13}$$

where the **T** matrix is defined in Eq. (3.1.8) and, as stated earlier in this Appendix, the index k = 1,2,3 corresponds to $q_k = \tilde{x}_i$, $\tilde{y}_i$, or $\tilde{z}_i$. The **D** matrix is symmetric. For visual clarity this is designated by the index "*s*" in the lower triangles.

The analytical form of the derivative of the potential between the i^{th} $p\mathrm{H}_2$ and the second Al atom is given by the same three equations [(3.1.11)–(3.1.13)], except with $\tilde{z}_i$ replaced by $\tilde{z}_i - R$. The table lookup algorithm discussed in the main text is used both for the potentials [V_Σ and V_Π] and their derivatives with respect to r.

Appendix 4.I Discrete Variable Representation (DVR)

We use a simple DVR method[112] to solve the time-independent Schrödinger equation (TISE) numerically in the position representation. The DVR method can be used for a conservative potential $V(r)$ for which bound states exist. Consider the one-dimensional TISE in the position representation:

$$-\frac{\hbar^2}{2m}\frac{\partial^2}{\partial r^2}\psi(r)+V(r)\psi(r)=E\psi(r) \tag{4.1.1}$$

We chose a finite region such that $\psi(r)$ is negligible outside the region. The independent variable r is divided into $m-1$ equal sectors of length s ($=r/m$). At the nodes $\{r_1, r_2, \ldots, r_m\}$, V has the values $\{V_1, V_2, \ldots, V_m\}$ and ψ has the values $\{\psi_1, \psi_2, \ldots, \psi_m\}$. Then, using a 3-point finite difference approximation to the derivative, the Hamiltonian at point i can be written as:

$$-\frac{\hbar^2}{2m}\frac{1}{s^2}(\psi_{i+1}+\psi_{i-1}-2\psi_i)+V_i\psi_i \tag{4.1.2}$$

Equation (4.1.1) can be rewritten in matrix form:

$$\left[\begin{pmatrix} V_1 & & & & \\ & V_2 & & & \\ & & V_3 & & \\ & & & \ldots & \\ & & & & V_m \end{pmatrix} - \frac{\hbar^2}{2ms^2}\begin{pmatrix} -2 & 1 & & & \\ 1 & -2 & 1 & & \\ & 1 & -2 & 1 & \\ & & . & . & . \\ & & & 1 & -2 \end{pmatrix}\right]\begin{pmatrix}\psi_1\\ \psi_2\\ \psi_3\\ \ldots\\ \psi_m\end{pmatrix} = E\begin{pmatrix}\psi_1\\ \psi_2\\ \psi_3\\ \ldots\\ \psi_m\end{pmatrix} \tag{4.1.3}$$

This is a set of homogeneous linear equations whose solutions are the value of the wavefunctions at the nodes. The eigenvalues $E_1, E_2, \ldots, E_m$, are the finite-difference approximation to the eigenenergies for our system. Convergence to the true energies and wavefunctions can be achieved by increasing the number of sectors and increasing the range of r which is spanned.

The corresponding approximation to the kinetic energy is also calculated in matrix form:

$$\frac{\begin{bmatrix}\psi_1 & \psi_2 & \psi_3 & \cdots & \psi_m\end{bmatrix}\left[-\frac{\hbar^2}{2ms^2}\begin{pmatrix}-2 & 1 & & & \\ 1 & -2 & 1 & & \\ & 1 & -2 & 1 & \\ & & . & . & . \\ & & & 1 & -2\end{pmatrix}\right]\begin{pmatrix}\psi_1\\ \psi_2\\ \psi_3\\ \cdots\\ \psi_m\end{pmatrix}}{\begin{bmatrix}\psi_1 & \psi_2 & \psi_3 & \cdots & \psi_m\end{bmatrix}\begin{pmatrix}\psi_1\\ \psi_2\\ \psi_3\\ \cdots\\ \psi_m\end{pmatrix}} \quad (4.1.4)$$

where $\{\psi_1, \psi_2, \ldots, \psi_m\}$ is the ground state eigenvector.

Appendix 4.II Tail Correction

Because of the finite size of the simulation box, the potential used in our simulations is always truncated. It is useful to have an estimate of how much the missing long-range part affects our results. Here we estimate the tail correction to the potential energy decrease when H_2 molecule is replaced by Al atom (without tail correction, ~ 12100 cm^{-1} when two Al atoms replace two H_2 molecules in case (a), and ~ 560 cm^{-1} per atom in other cases).

For pairwise-additive potentials, a popular method[24] to estimate tail correction is to assume that pair correlation function $g(r) \approx 1$ in the region of $r>r_c$, where r_c is the spherical cutoff distance. Then for a potential $V(r)$, the long-range correction to the average total potential energy E for N particles is:

$$E_{LRC} = 2\pi N\rho \int_{r_c}^{\infty} r^2 V(r) dr \qquad (4.2.1)$$

Strictly speaking, since we use a minimum image convention in handling the periodic boundary condition,[24] we have a rectangular simulation box. Neglecting the difference between our nearly square box and the sphere, we set r_c to be half of the length of the shortest edge. The resulting error in the tail correction should be small.

We have at most two Al atoms in our simulation, so there is no need to consider a tail correction to the Al–Al interaction. For the H_2–H_2 Silvera-Goldman pair potential,[91], the long-range correction is estimated to be –4.12 cm^{-1} per H_2. For the Al–H_2 interaction, caution must be taken because it is not a pair-wise additive potential. We use the spherically averaged potential V_{sph}. The tail correction should be twice Eq. (4.2.1), since we have two Al atoms. This turns out to be –11.32 cm^{-1} per Al atom. So the tail correction for the average potential energy change of replacing one H_2 by a single Al atom is –11.32+4.12 = –7.2 cm^{-1}. In the case of two Al atoms replacement, it is a further decrease of –7.2×2 = –14.4cm^{-1}.

Bibliography

1. F. Jensen, *Introduction to Computational Chemistry*, Reprint ed. (John Wiley & Sons, 2001).
2. S. Tam, M. Macler, M. E. DeRose, and M. E. Fajardo, J. Chem. Phys. **113**, 9067 (2000).
3. F. Stienkemeier and A. F. Vilesov, J. Chem. Phys. **115**, 10119 (2001).
4. F. Stienkemeier, J. Higgins, C. Callegari, S. I. Kanorsky, W. E. Ernst, and G. Scoles, Z. Phys. D **38**, 253 (1996).
5. J. H. Reho, U. Merker, M. R. Radcliff, K. K. Lehmann, and G. Scoles, J. Phys. Chem. A **104**, 3620 (2000).
6. J. Reho, U. Merker, M. R. Radcliff, K. K. Lehmann, and G. Scoles, J. Chem. Phys. **112**, 8409 (2000).
7. J. A. Northby, J. Chem. Phys. **115**, 10065 (2001).
8. J. Higgins, C. Callegari, J. Reho, F. Stienkemeier, W. E. Ernst, M. Gutowski, and G. Scoles, J. Phys. Chem. A **102**, 4952 (1998).
9. M. E. Fajardo, S. Tam, T. L. Thompson, and M. E. Cordonnier, Chem. Phys. **189**, 351 (1994).
10. M. E. Fajardo, J. Propul. Power **8**, 30 (1992).
11. C. Callegari, K. K. Lehmann, R. Schmied, and G. Scoles, J. Chem. Phys. **115**, 10090 (2001).
12. J. R. Krumrine, M. H. Alexander, X. Yang, and P. J. Dagdigian, J. Chem. Phys. **112**, 5037 (2000).
13. A. Vegiri, M. H. Alexander, S. Gregurick, A. B. McCoy, and R. B. Gerber, J. Chem. Phys. **101**, 2577 (1994).
14. L. C. Balling and J. J. Wright, J. Chem. Phys. **79**, 2941 (1983).
15. J. R. Krumrine, S. Jang, M. H. Alexander, and G. A. Voth, J. Chem. Phys. **113**, 9079 (2000).
16. D. T. Mirijanian, M. H. Alexander, and G. A. Voth, Chem. Phys. Lett. **365**, 487 (2002).

17. M. H. Alexander, A. R. Walton, M. Yang, X. Yang, E. Hwang, and P. J. Dagdigian, J. Chem. Phys. **106**, 6320 (1997).
18. C. E. Moore, *Atomic Energy levels, NSRDS-NBS 35*. (U.S. Government Printing Office, Washington, D. C., 1971).
19. D. M. Ceperley, Rev. Mod. Phys. **67**, 279 (1995).
20. B. J. Berne and D. Thirumalai, Ann. Rev. Phys. Chem **37**, 401 (1986).
21. R. P. Feynman and A. R. Hibbs, *Quantum mechanics and path integrals*. (McGraw-Hill, New York, 1965).
22. H. F. Trotter, Proc. Am. Math. Soc. **10**, 545 (1959).
23. C. Chakravarty, J. Chem. Phys. **116**, 8938 (2002).
24. M. P. Allen and D. J. Tildesley, *Computer Simulation of Liquids*. (Oxford University Press, New York, 1987).
25. N. Metropolis, A. W. Rosenbluth, M. N. Rosenbluth, A. H. Teller, and E. Teller, J. Chem. Phys. **21**, 1087 (1953).
26. M. E. Tuckerman, B. J. Berne, G. J. Martyna, and M. L. Klein, J. Chem. Phys. **99**, 2796 (1993).
27. S. Jang and G. A. Voth, J. Chem. Phys. **107**, 9514 (1997).
28. G. J. Martyna, M. L. Klein, and M. E. Tuckerman, J. Chem. Phys. **97**, 2635 (1992).
29. S. Nose, Mol. Phys. **52**, 255 (1984).
30. W. G. Hoover, Phys. Rev. A **31**, 1695 (1985).
31. D. Chandler, *Introduction to Modern Statistical Mechanics*. (Oxford University Press, New York, 1987).
32. J. A. Barker, J. Chem. Phys. **70**, 2914 (1979).
33. M. Neumann and M. Zoppi, Phys. Rev. E **65**, 031203 (2002).
34. J.-L. Barrat, P. Loubeyre, and M. L. Klein, J. Chem. Phys. **90**, 5644 (1989).
35. M. F. Herman, E. J. Bruskin, and B. J. Berne, J. Chem. Phys. **76**, 5150 (1982).
36. M. Parrinello and A. Rahman, J. Chem. Phys. **80**, 860 (1984).
37. Y. J. Wong and G. V. Chester, Phys. Rev. B **37**, 9590 (1988).
38. M. H. Müser, P. Nielaba, and K. Binder, Phys. Rev. B **51**, 2723 (1995).
39. I. N. Levine, *Quantum Chemistry*, Fifth ed. (Prentice-Hall, New Jersey, 2000).

40. D. Finchamm, N. Quirke, and D. J. Tildesley, J. Chem. Phys. **84**, 4535 (1986).
41. A. Nakayama and K. Yamashita, J. Chem. Phys. **114**, 780 (2001).
42. F. Ancilotto, P. B. Lerner, and M. W. Cole, J. Low Temp. Phys. **101**, 1123 (1995).
43. T. Nakatsukasa, K. Yabana, and G. F. Bertsch, Phys. Rev. A **65**, 032512 (2002).
44. C. C. Lovallo and M. Klobukowski, J. Chem. Phys. **120**, 246 (2004).
45. C. C. Lovallo and M. Klobukowski, Chem. Phys. Lett. **373**, 439 (2003).
46. R. J. Hinde, J. Phys. B **36**, 3119 (2003).
47. P. Huang, Y. Kwon, and K. B. Whaley, in *Microscopic Approaches to Quantum Liquids in Confined Geometries*, edited by E. Krotscheck and J. Navarro (World Scientific, Singapore, 2002).
48. N. Blinov, X. Song, and P.-N. Roy, J. Chem. Phys. **120**, 5916 (2004).
49. C. Chakravarty, M. C. Gordillo, and D. M. Ceperley, J. Chem. Phys. **109** (1998).
50. L. Brualla, Ph. D thesis, Technical University of Catalonia, 2002.
51. Q. Hui, J. L. Persson, J. H. M. Beijersbergen, and M. Takami, Z. Phys. B **98**, 353 (1995).
52. R. A. Aziz and A. R. Janzen, Phys. Rev. lett. **74**, 1586 (1995).
53. M. H. Alexander, (private communication).
54. MOLPRO is a package of ab initio programs written by H.-J. Werner, P. J. Knowles, M. Schütz, R. Lindh, P. Celani, T. Korona, G. Rauhut, F. R. Manby, R. D. Amos, A. Bernhardsson, A. Berning, D. L. Cooper, M. J. O. Deegan, A. J. Dobbyn, F. Eckert, C. Hampel, G. Hetzer, A. W. Lloyd, S. J. McNicholas, W. Meyer, M. E. Mura, A. Nicklaß, P. Palmieri, R. Pitzer, U. Schumann, H. Stoll, A. J. Stone R. Tarroni, and T. Thorsteinsson.
55. K. A. Peterson and T. H. Dunning, Jr., J. Phys. Chem. A **101**, 6280 (1997).
56. M. P. D. Lara-castells, R. V. Krems, A. A. Buchachenko, G. Delgado-barrio, and P. Vilarreal, J. Chem. Phys. **115** (2001).
57. J. M. L. Martin, Chem. Phys. Lett. **259**, 679 (1996).
58. J. M. L. Martin and P. R. Taylor, J. Chem. Phys. **106**, 8620 (1997).

59. A. R. Edmonds, *Angular Momentum in Quantum Mechanics*, 2nd ed. (Princeton Unversity Press, Princeton, 1974).
60. R. N. Zare, *Angular Momentum*. (John Wiley & Sons, 1988).
61. P. Lévy, Compositio Math **7**, 283 (1939).
62. D. M. Ceperley and E. L. Pollock, Phys. Rev. lett. **56**, 351 (1986).
63. M. Lax, J. Chem. Phys. **20**, 1752 (1952).
64. E. Cheng and K. B. Whaley, J. Chem. Phys. **104**, 3155 (1996).
65. J. Simons and J. Nicoles, *Quantum Mechanics in Chemistry*. (Oxford University Press, Inc., New York, 1997).
66. C. Tao, P. J. Dagdigian, and M. H. Alexander, Chem. Phys. Lett. **392**, 151 (2004).
67. J. J. Sakurai, *Modern Quantum Mechanics*, Rev. ed. (Addison-Wesley, 1994).
68. M. E. Fajardo, S. Tam, and M. Macler, (private communication).
69. S. Tam, M. Macler, and M. E. Fajardo, J. Chem. Phys. **106**, 8955 (1997).
70. D. Scharf, G. J. Martyna, D. Li, G. A. Voth, and M. L. Klein, J. Chem. Phys. **99**, 9013 (1993).
71. S. Jang, S. Jang, and G. A. Voth, J. Phys. Chem. A **103**, 9512 (1999).
72. S. Jang and G. A. Voth, J. Chem. Phys. **108**, 4098 (1998).
73. R. J. Hinde, D. T. Anderson, S. Tam, and M. E. Fajardo, Chem. Phys. Lett. **356**, 355 (2002).
74. X. Tan, P. J. Dagdigian, J. Williams, and M. H. Alexander, J. Chem. Phys. **114**, 8938 (2001).
75. W. Moffitt, Proc. R. Soc. London, Ser. A **210**, 245 (1951).
76. V. S. Batista and D. F. Coker, J. Chem. Phys. **105**, 4033 (1996).
77. H.-J. Werner and W. Meryer, J. Chem. Phys. **74**, 5794 (1981).
78. H.-J. Werner and P. J. Knowles, J. Chem. Phys. **89**, 5803 (1988).
79. P. J. Knowles and H.-J. Werner, Chem. Phys. Lett. **145**, 514 (1988).
80. T. H. Dunning, Jr., J. Chem. Phys. **90**, 1007 (1989).
81. R. A. Kendall, T. H. Dunning, Jr., and R. J. Harrison, J. Chem. Phys. **96**, 6796 (1992).
82. D. E. Woon and T. H. Dunning, Jr., J. Chem. Phys. **98**, 1358 (1993).

83. M. F. Cai, C. C. Carter, T. A. Millar, and V. E. Bondybey, Chem. Phys. **115**, 233 (1991).
84. F. O. Ellison, J. Am. Chem. Soc. **85**, 3540 (1963).
85. G. G. Balint-Kurti and M. Karplus, J. Chem. Phys. **50**, 478 (1969).
86. R. K. Preston and J. C. Tully, J. Chem. Phys. **54**, 4297 (1971).
87. G. G. Balint-Kurti, Mol. Phys. **25**, 393 (1973).
88. F. O. Ellison, N. T. Huff, and J. C. Patel, J. Am. Chem. Soc. **85**, 3544 (1963).
89. I. Last, Chem. Phys. **55**, 237 (1981).
90. E. Hwang, Y.-L. Huang, P. J. Dagdigian, and M. H. Alexander, J. Chem. Phys. **98**, 8484 (1993).
91. I. F. Silvera and V. V. Goldman, J. Chem. Phys. **69**, 4209 (1978).
92. I. F. Silvera, Rev. Mod. Phys. **52**, 393 (1980).
93. M. E. Fajardo, J. Chem. Phys. **98**, 110 (1993).
94. D. Scharf, G. J. Martyna, and M. L. Klein, J. Chem. Phys. **99**, 8997 (1993).
95. K. Kinugawa, P. B. Moore, and M. L. Klein, J. Chem. Phys. **109**, 610 (1998).
96. J. A. Boatz and M. E. Fajardo, J. Chem. Phys. **101**, 3472 (1994).
97. T. Kiljunen, J. Eloranta, J. Ahokas, and H. Kunttu, J. Chem. Phys. **114**, 7157 (2001).
98. T. Kiljunen, J. Eloranta, J. Ahokas, and H. Kunttu, J. Chem. Phys. **114**, 7144 (2001).
99. Q. Wang, M. H. Alexander, and J. R. Krumrine, J. Chem. Phys. **117**, 5311 (2002).
100. J. Williams and M. H. Alexander, J. Chem. Phys. **112**, 5722 (2000).
101. T. L. Hill, *An introduction to statistical thermodynamics*. (Dover Publications, New York, 1986).
102. M. Zoppi and M. Neumann, Phys. Rev. B **43**, 10242 (1991).
103. M. Zoppi, B. Bafile, E. Guarini, F. Barocchi, R. Magli, and M. Neumann, Phys. Rev. lett. **75**, 1779 (1995).
104. M. Nielsen, Phys. Rev. B **7**, 1626 (1973).
105. Y. Kwon, P. Huang, M. V. Patel, B. Dorte, and K. B. Whaley, J. Chem. Phys. **113**, 6469 (2000).

106. M. Lindsay, (private communication, 2004).
107. M. Mella, G. Calderoni, and F. Cargnoni, J. Chem. Phys. **preprint** (2005).
108. D. J. Nesbitt, (private communication, 2003).
109. M. Sprik, M. L. Klein, and D. Chandler, Phys. Rev. B **31**, 4234 (1985).
110. E. L. Pollock and D. M. Ceperley, Phys. Rev. B **30**, 2555 (1984).
111. W. Janke and T. Sauer, Chem. Phys. Lett. **263**, 488 (1996).
112. D. T. Colbert and W. H. Miller, J. Chem. Phys. **96**, 1982 (1992).